Polymer-micromachined Table-shaped Flexible Tactile Sensor

Department of Micro-Nano Systems Engineering

Nagoya University

Jeong Il Lee

Abstract

This thesis describes the development of a flexible tactile sensor that has a three-dimensional table-shaped sensing part for equipment on an intelligent robot's fingertips. We proposed a sensing principle and experimentally demonstrated a new type of tactile sensor that can detect three-dimensional forces and has suitable flexibility and good sensitivity. We developed required polymer-micromachining technology applicable for the sensor.

To amplify the contact signal, a three-dimensionally designed table-shaped sensing element was attempted. A table-shaped epoxy sensing plate with four legs was built on top of a flexible and thin polymer substrate. This structure could effectively convert an external acting force into the concentrated internal stress. The normal and tangential forces could be detected by combining responses from metal strain gauges on the polymer substrate. Triaxial force detection was calculated by combining two-dimensional mapping data on the basis of strain distribution calculated by finite element analysis (FEA) simulation. The external loads applied to the sensor could be detected as a function of the strain-gauge responses.

To fabricate a three-dimensional structure of polymer-based sensor, we propose a new fabrication method in polymer-micromachining technologies such as thermo-compatible layer-by-layer process and thick sacrificial layer without wet or dry etching process. Moreover, three-dimensional structure patterning of up to 60-μm thickness was achieved by using a photo-definable lithography process with a photoresist material as a thick sacrificial layer.

The fabricated flexible tactile sensor was calibrated under normal and tangential forces by using the evaluation apparatus. The sensor showed the sensitivity in terms of $\Delta R/R$. Furthermore, normal and tangential force components showed good linearity to applied force.

Contents

Chapter 1

Introduction

1.1 Motivation

1.1.1 Background of the research

The aging society and the disabled

The world-wide trend of an aging society is occurring with a lack of workforce caused by the increase of life span and decrease of birth rate [1]. In particular, Japan is undergoing a rapid demographic change. Figure 1.1.1 shows the trends and future projection of average life expectancy based on the estimated figure on the assumption that death rate is ranked medium. The average life expectancy was 78.56 for males and 85.52 for females in 2005. However, after 50 years, it will continue to rise for both males and females, in 2055 being 83.67 for males and 90.34 for females [2].

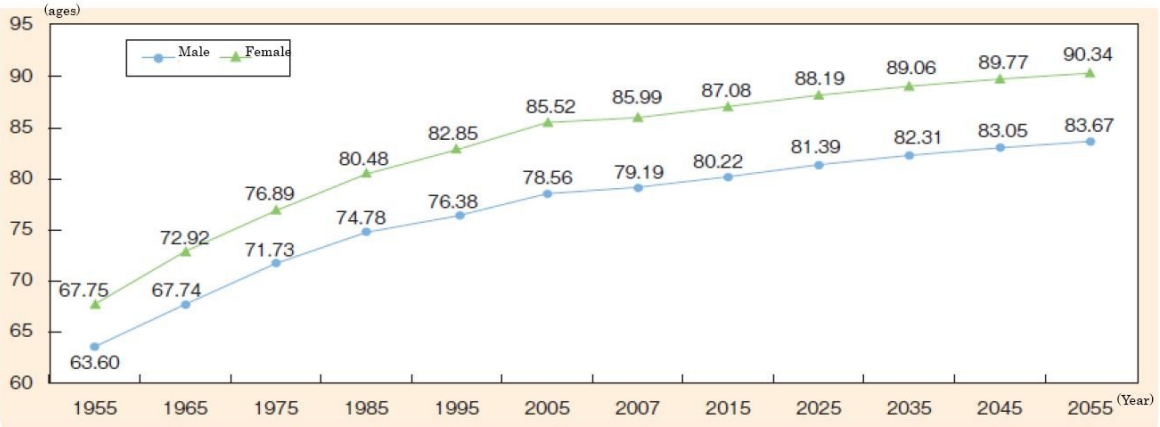

Figure 1.1.1 Trends and future projection of average life expectancy [2].

In Japan, the population of elderly people (aged 65 or older) will be 36.5 million with 40.5% share of the national total population (aging rate) in 2055 [2]. Meanwhile, it is estimated that population of the children (0-14 years old) will number less than 7.52 million in 2055 [2]. The decrease in number of births leads to decrease of the working age population (15-64 years old), which will be less than 80 million in 2012 and become 45.95 million in 2055, i.e. 1.3 working age people for every 1 elderly person in 2055 (see Table 1.1.1) [2]. Japan is expected to become an aged society the like of which no other country in the world has experienced [2].

Table 1.1.1 Number of persons aged 15-64 (working age population) who have supported the elderly aged 65 or older [2].

Year	persons
1965	10.8
1975	8.6
1985	6.6
1995	4.8
2005	3.3
2015	2.3 (expected)
2055	1.3 (expected)

In addition, the number of disabled people is growing through a variety of inevitable accidents [3-4]. Physical disability consists of half of the total disability in 2006, Japan (see Figure 1.1.2) [4]. In regard to social paradigm in welfare services, government manage is also changed passive protection into active supports for the disabled [5].

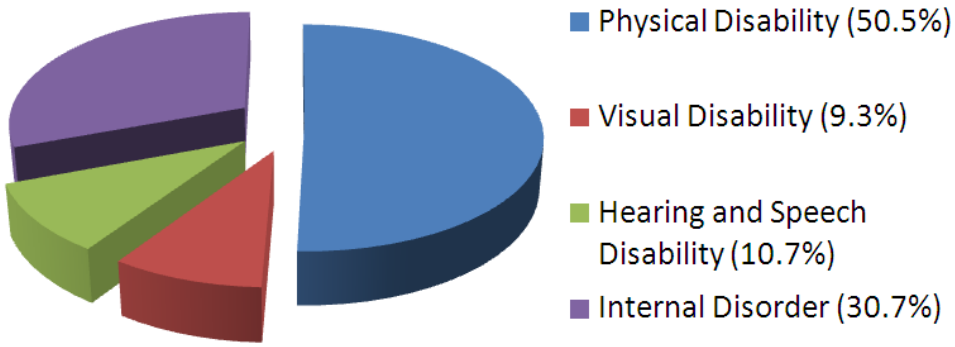

Figure 1.1.2 Survey on persons with physical disability in Japan [4].

Development of intelligent robot industry

Related-industries in the aging society and the disabled, i.e., rehabilitation and intelligent robot (particularly service robot) industries, including 'assistive devices' and the 'Silver-mate robot' for home-care nursing of the elderly and the disabled, receive a great deal of attention; some reports expect that these industries will increase a surprising amount within five years [6-7]. In 2010, the Ministry of Economy, Trade and Industry of Japan (METI) and the New Energy and Industrial Technology Development Organization of Japan (NEDO) expected projections in the growth of robot market [7]. According to the projections, the robot industry is expected to 9.7 trillion Japan Yen in 2035 [7]. This expansion of robot market is driven by services sector which has almost half of the potion in 2035 (see Figure 1.1.3) [7].

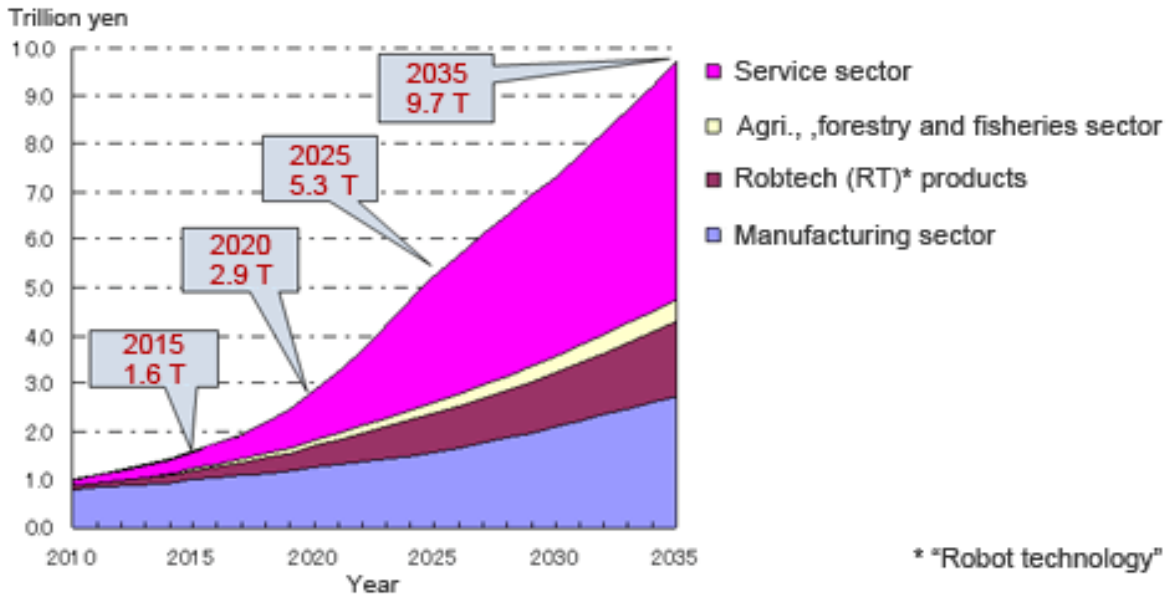

Figure 1.1.3 Robot market projections through 2035 in Japan [7].

1.1.2 Intelligent robot's fingertips and tactile sensor

Intelligent robot and tactile sensor

As industrialization is progressing gradually to a higher level, there is a large range of demands for human-like precise and complex measurements. There is a variety of specially designated sensing devices matched to each main sensing modalities — sight, sound, smell, taste and touch. Although studies on human mimetic sensors — especially in the fields of vision and audition — have been performed actively, the situation is not the same for the tactile field [8-9]. In the early stage, tactile sensing devices were intended for applications in medicine and assistive devices. For example, medical robots equipped tactile sensing device can provide surgeons with technical supports of enhanced dexterity and precise control (Figure 1.1.4) [10].

Figure 1.1.4 Intuitive surgical's da Vinci® surgical system [10].

HRI : Human robot interaction

In recent years, studies on human-robot interaction have needed to utilize tactile sensors to physically interact with people and their environment in contexts such as rehabilitation, home/hospital care, education, and entertainment. In regard to human communication, physical touch is essential for an infant or child's social, cognitive, and physical development [11]. Touch also plays an important role in adulthood, when a person is soothing, playing, and maintaining proximity between a child and caretaker [12]. Similarly, physical interaction with robots (such as hugging and hand shaking) builds closer relationships between a human and a robot from the perspective of spatial distance [13]. The *ROBOSKIN* project shows another application domain of tactile interaction, namely, that between robots and autistic children to improve social-interaction capabilities of the children (Figure 1.1.5) [14]. Furthermore, physical therapy for stroke rehabilitation by robotic manipulators is a promising application of tactile sensors [15].

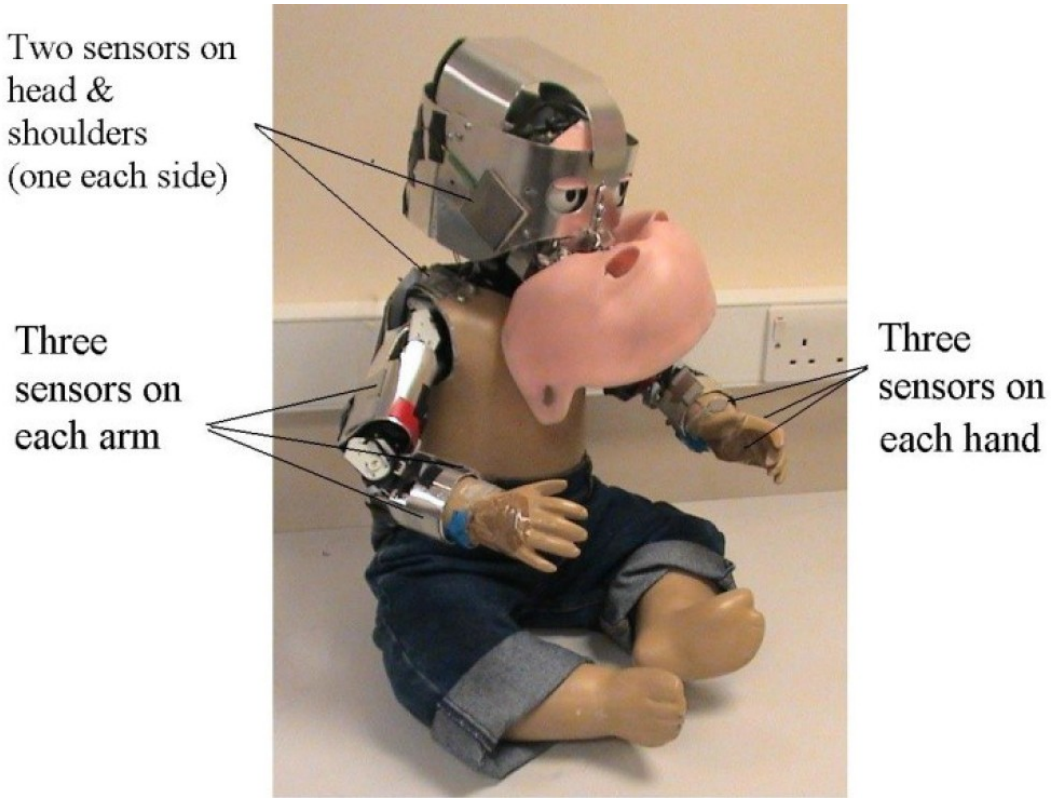

Figure 1.1.5 Illustration of the temporary tactile sensors [14].

Demand of tactile sensor for intelligent robot's fingertip

In work on the human-robot collaboration, researchers have developed tactile sensors [16-17]. Manipulating objects by a robotic hand requires flexible tactile sensors mounted on the curved surface of the robot's fingertip to detect the forces acting on it. To dexterously manipulate and grasp an object while maintaining physical contact between the object and the robot's finger tips, it must be possible to measure normal and tangential forces acting on the object (see Table 1.1.2) [8-9].

Table 1.1.2 Required tactile sensor specification for robot's fingertip [9].

Spatial resolution	1 ~ 2 mm
Sensitivity	< 5 g/mm^2 (0.05 N)
Response range	0 ~ 100 g/mm^2 (1 N)
Frequency response	< 100 Hz (10 ms)
Curvature	< 8 mm
Output response	monotonic and low hysteresis

To enable that measurement, two studies applied displacement control by robot-vision systems (see Figure 1.1.6) [18-19] and another used a force-toque sensor on the fingertips of the robotic hand (see Figure 1.1.7) [20-21]. In consideration of the role of tactile sensors in the domain of human-robot interaction, it is necessary to ensure that the sensors are small and flexible enough to fit onto various surfaces of machinery components as well as have sufficient accuracy to allow precise manipulation of the robotic hand.

Figure 1.1.6 Vision-based displacement control [12].

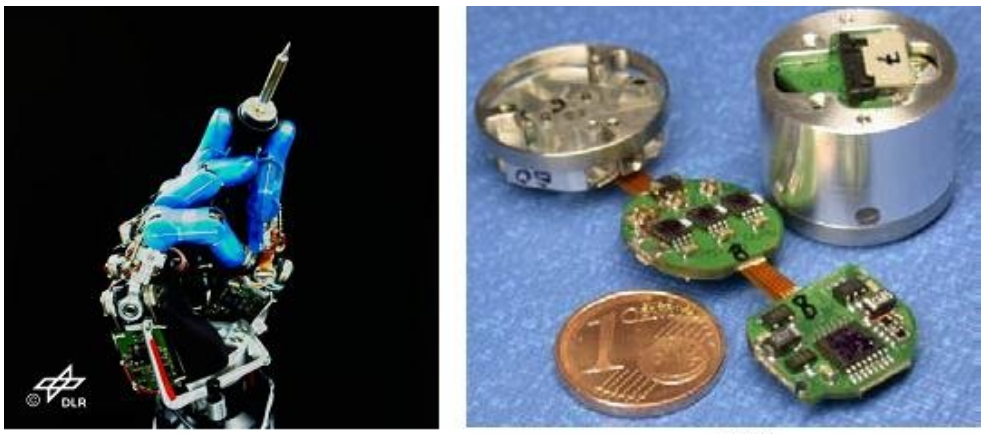

(A) (B)

Figure 1.1.7 DLR hand (A) and force-torque sensor (B) [21].

1.2 Review of previous studies

1.2.1 Development of tactile sensor

Researchers have developed several types of tactile sensor by "microelectromechanical systems" (MEMS) technology based on different materials (e.g., silicon and polymers). Many researchers have proposed MEMS-based tactile sensors, because MEMS can be applied to integrated tiny sensing units.

Silicon based tactile sensors

Sensors based on silicon were tried first [22-27]. In the early stage of developing tactile sensors, Kane et al. [22] and Mei et al. [23] used micromachining to fabricate diaphragm-style tactile sensors composed of triaxial force sensors (see Figure 1.2.1).

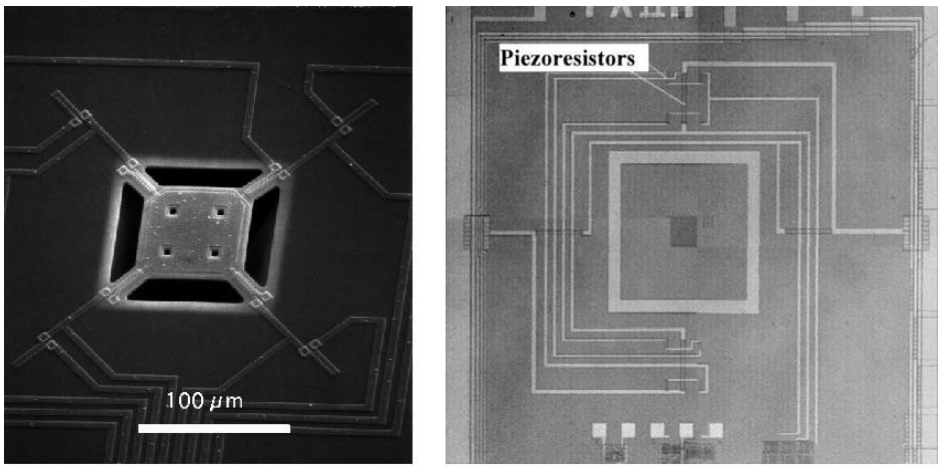

Figure 1.2.1 Silicon based tactile sensor (A) with a diaphragm [22], (B) composed of membrane and mesa structure [23].

Hasegawa et al. [24] have developed active tactile sensor that detects the contact force and hardness using piezo-resistor on the diaphragm by a

pneumatic actuation (see Figure 1.2.2).

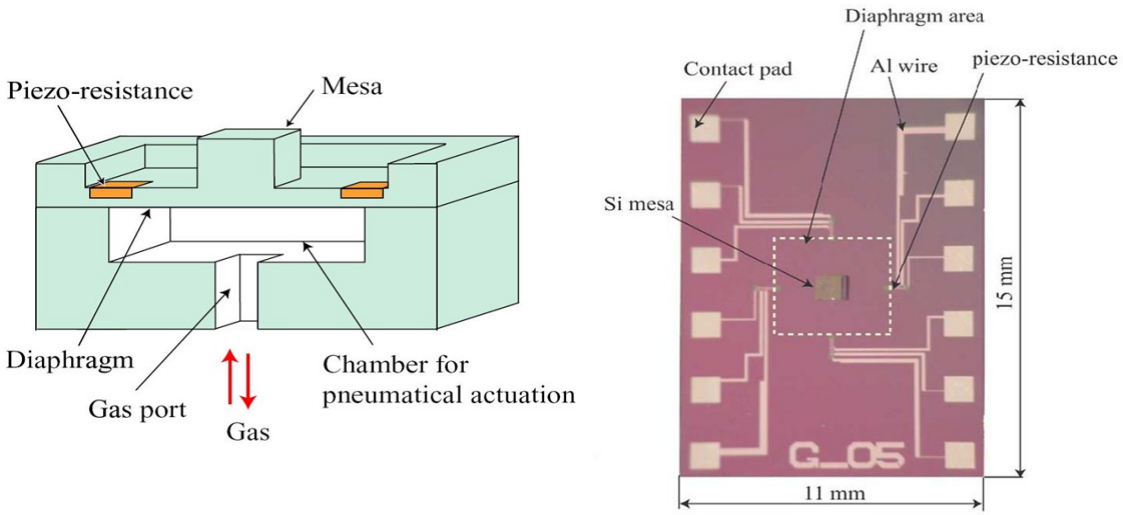

Figure 1.2.2 Silicon tactile sensor with a pneumatic actuation [24].

Beccai et al. [25] have fabricated a tactile sensor using four bridges with a high silicon mesa (see Figure 1.2.3).

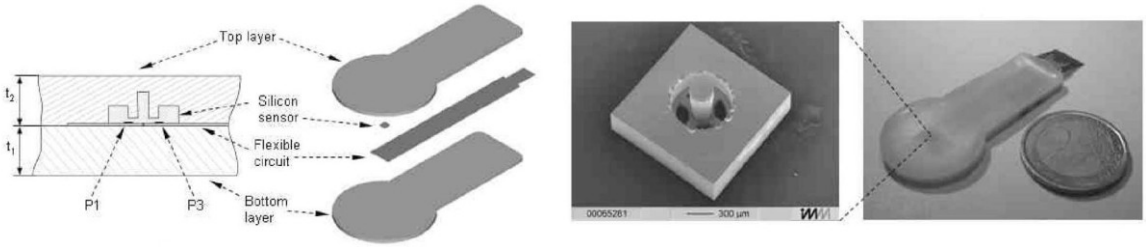

Figure 1.2.3 Silicon-based force sensor with a cylindrical mesa structure [25].

Spinner et al. [26] have developed 3-axial force sensor using thin membrane hinges and suspended probe pin (see Figure 1.2.4).

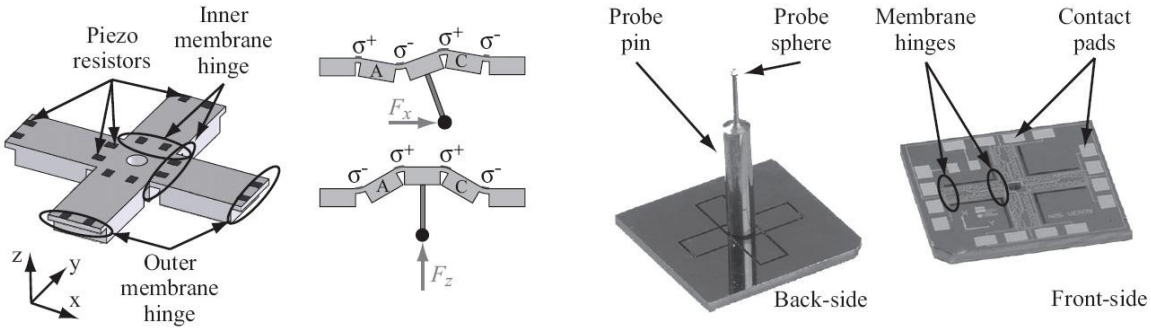

Figure 1.2.4 Silicon force sensor with hinges and suspended probe [26].

Nakazawa et al. [27] have fabricated a force-moment sensor that can independently detect three components of moment (M_x, M_y, M_z) and one component of force (F_z) using a joystick (see Figure 1.2.5).

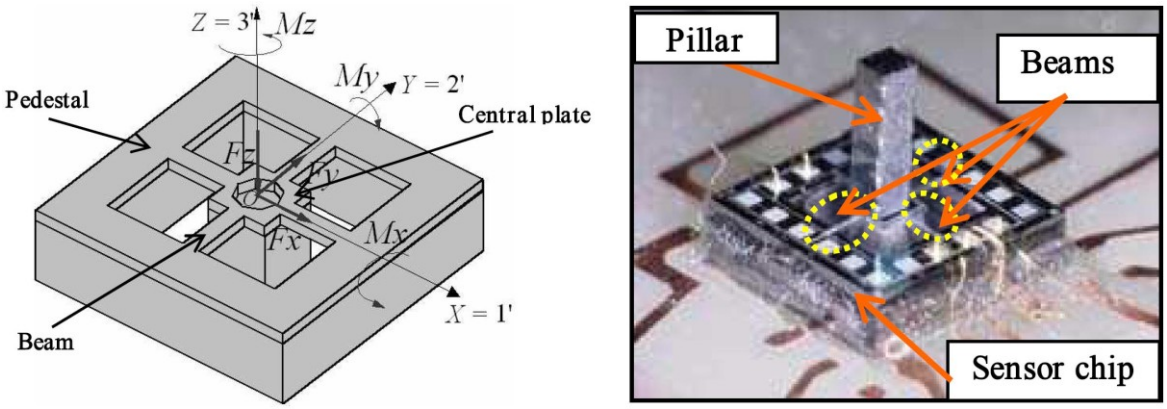

Figure 1.2.5 Force-moment sensor with a joystick [27].

Polymer material based tactile sensors

Another approach is application of the change of capacitance or conductive polymer materials [28-31]. Shimojo et al. [28] have developed tactile sensing sheet using conductive rubber with stitched electrical-wires. Suzuki et al. [29] have fabricated fabric tactile sensor using hollow fibers (see Figure 1.2.6).

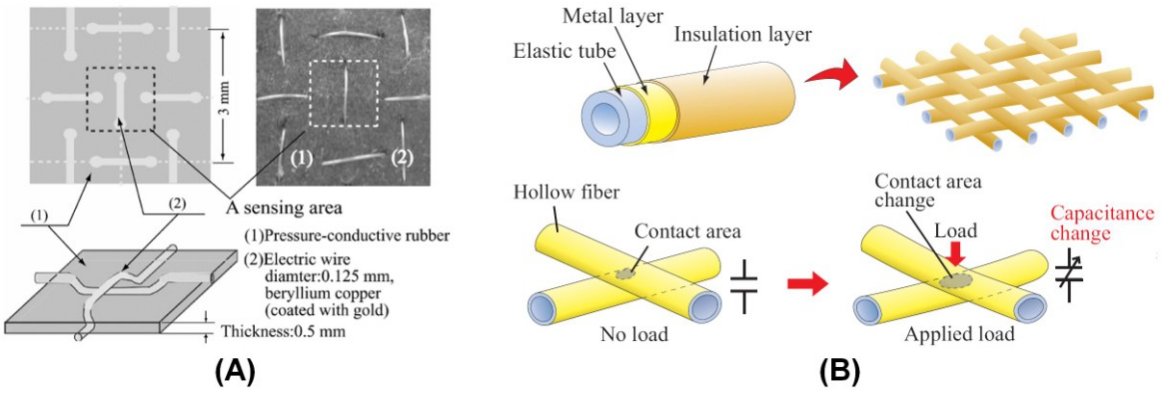

Figure 1.2.6 Tactile sensor using stitched electrical-wires [28] and hollow fibers [29].

Choi et al.[30] have developed tactile sensor for detecting contact force and slip based on polyvinylidene fluoride (PVDF), and pressure variable resistor ink (see Figure 1.2.7). Yang et al. [31] have fabricated temperature and tactile sensing array with conductive polymer film (see figure 1.2.8).

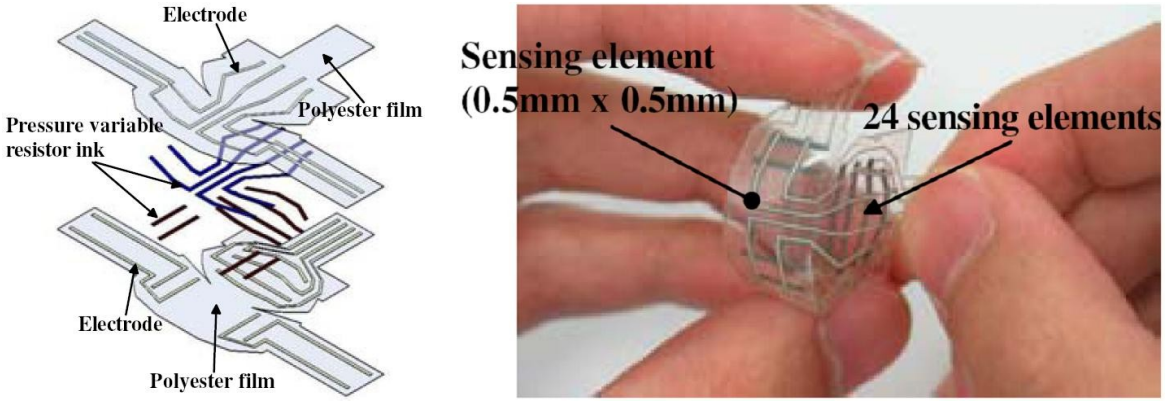

Figure 1.2.7 Tactile sensor using pressure variable resistor ink [30].

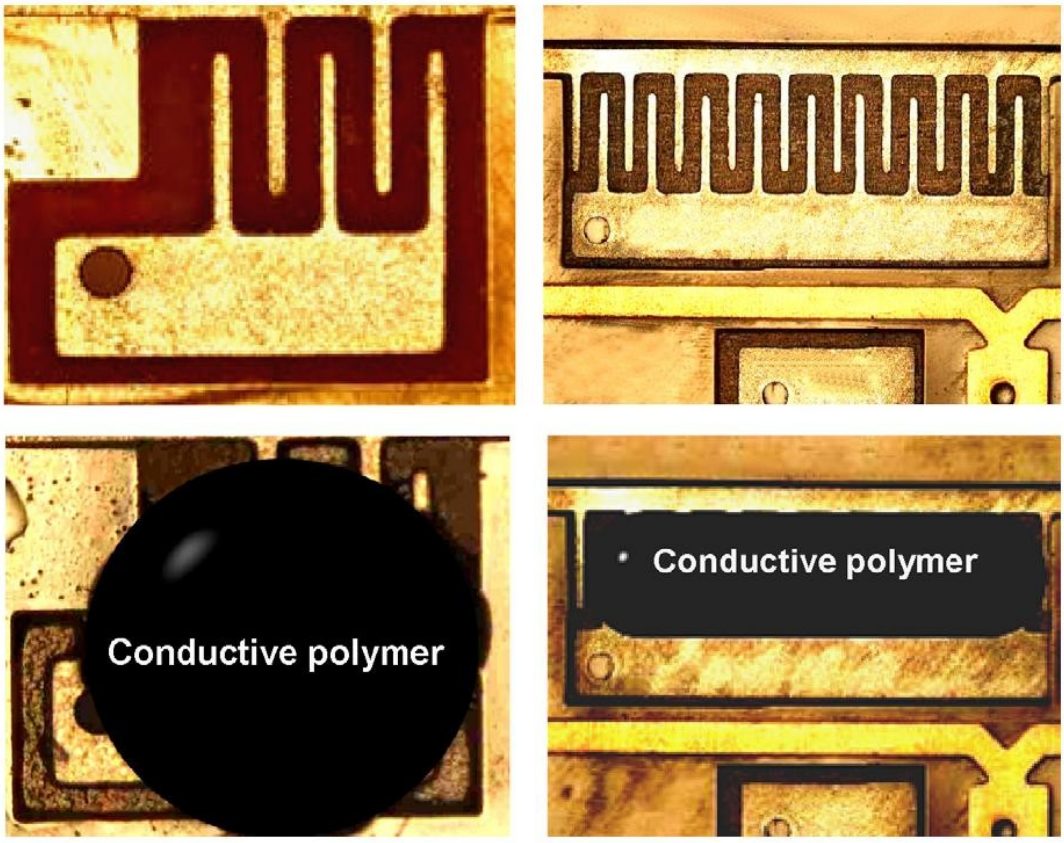

Figure 1.2.8 Temperature and tactile sensor using conductive polymer [31].

Tactile sensors using optical method

The other approach is application of the change of optical signal [32-33]. Hristuy et al. [32] have fabricated tactile sensor using vision system with gel-filled patterned membrane (see Figure 1.2.9).

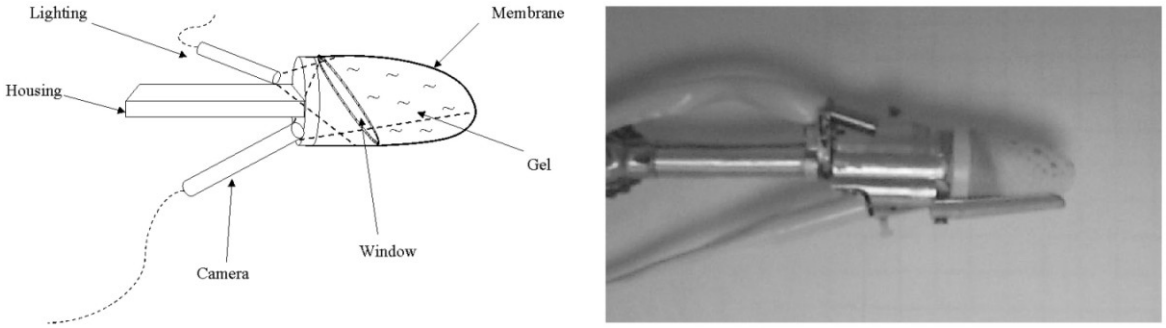

Figure 1.2.9 Tactile sensor using gel-filled patterned membrane [32].

Ohka et al. [33] have developed tactile sensor using vision system with optical fiber (see Figure 1.2.10).

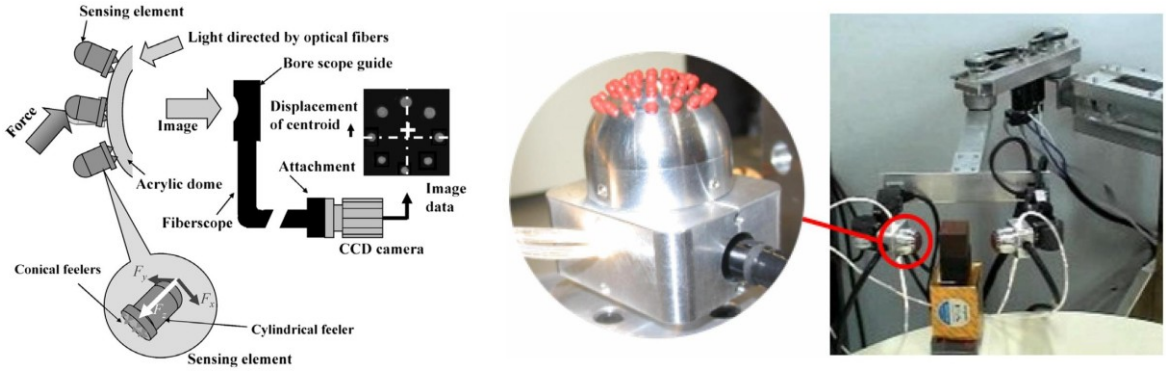

Figure 1.2.10 Tactile sensor using optical fiber and vision system [33].

Tactile sensors using polymer-micromachining I – PDMS-type

According to the demand for small sized sensing device and flexibility, micromachining technology using polymer materials has been proposed. This technology called a polymer-micromachining that enables the integration of MEMS devices on a flexible polymer substrate [34-35]. Two types of full

polymer-based tactile sensors have been proposed based on different physical principles. The capacitance-type tactile sensor composed of polydimethylsiloxane (PDMS) is one type of full polymer-based tactile sensor [36-39]. A capacitive sensor acts on the applied force that expressed changes of the distance between two plates of the capacitor. Capacitor-based tactile sensors are micro-fabricated by two conductive electrodes embedded in flexible dielectric material (PDMS). H. K. Lee et al. have proposed a modular expandable capacitive tactile sensor using PDMS (see Figure 1.2.11) [36], and have upgraded the 3-axial force detecting sensor type (see Figure 1.2.12) [37]. Cheng et al. [38] and Peng et al. [39] have fabricated a flexible capacitive tactile sensor using polymer-micromachining by a method similar to that mentioned above.

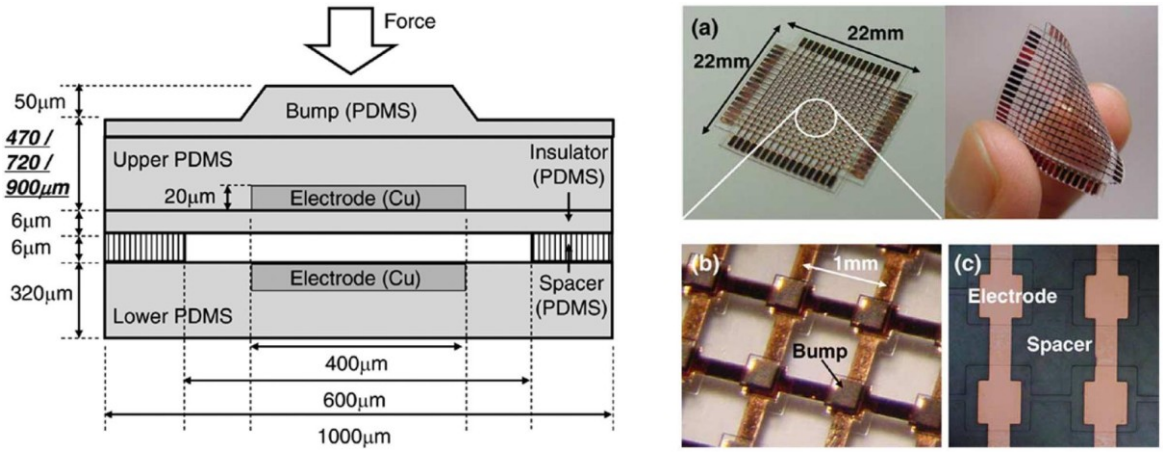

Figure 1.2.11 Modular expandable capacitive tactile sensor [36].

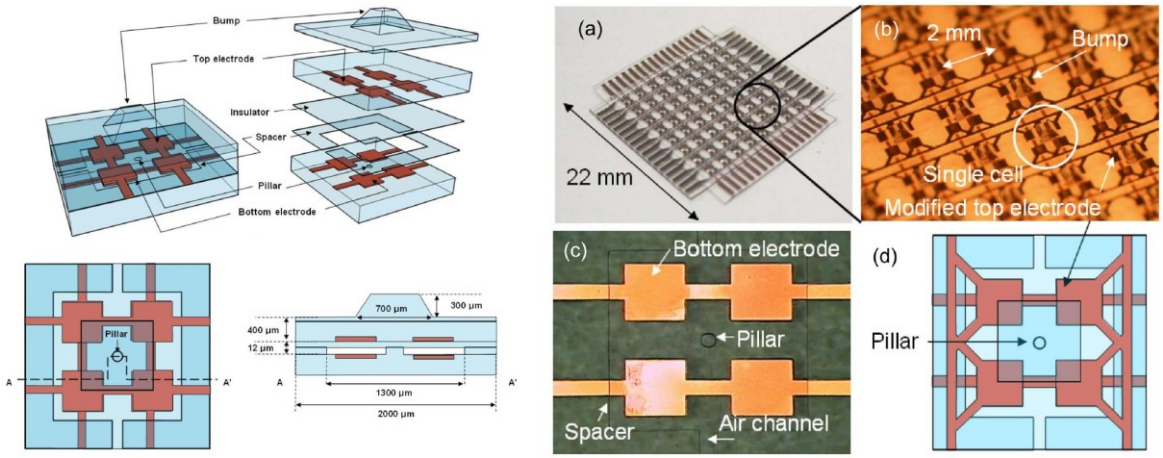

Figure 1.2.12 3-axial force detectable tactile sensor [37].

Tactile sensors using polymer-micromachining II – Polyimide-type

The other type of polymer tactile sensor is the resistance-based sensor composed of a photo-definable polyimide precursor or a wet-etched polyimide film [40-45]. Engel et al. have proposed the first entirely polyimide-based, 10×10 tactile sensor array using polymer-micromachining with an inverted fabrication technique (called etch-release method) (see Figure 1.2.13) [40].

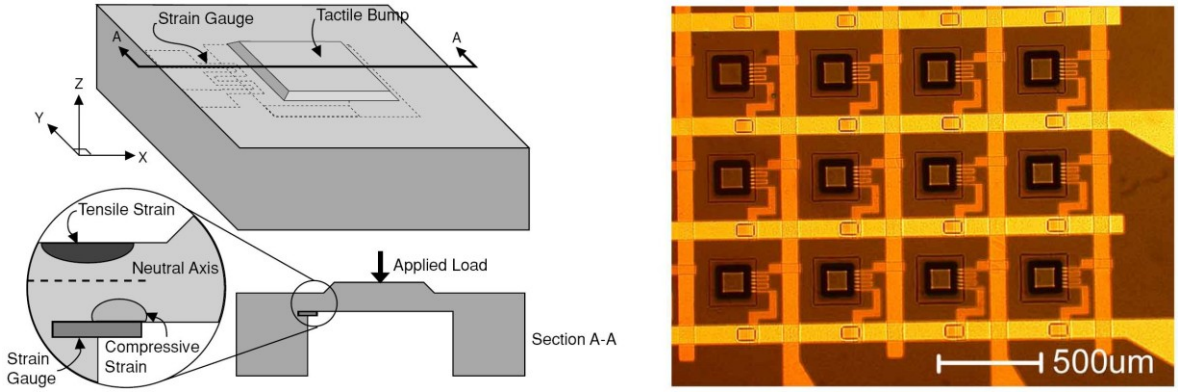

Figure 1.2.13 Tactile sensor using etch-release method [40].

J. H. Kim et al. [41] and J. I. Lee et al. [42] have fabricated a 10×10 array flexible resistive tactile sensor using the etch-release method (see Figure 1.2.14).

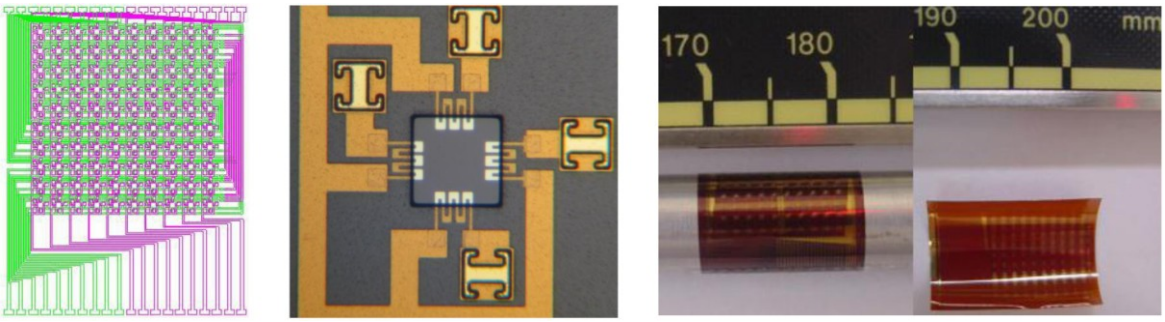

Figure 1.2.14 Tactile sensor using wet-etched polyimide film [42].

Kwon et al. [43-44] have developed a 4×4 array flexible resistive tactile sensor using wet-etched polyimide film (see Figure 1.2.15).

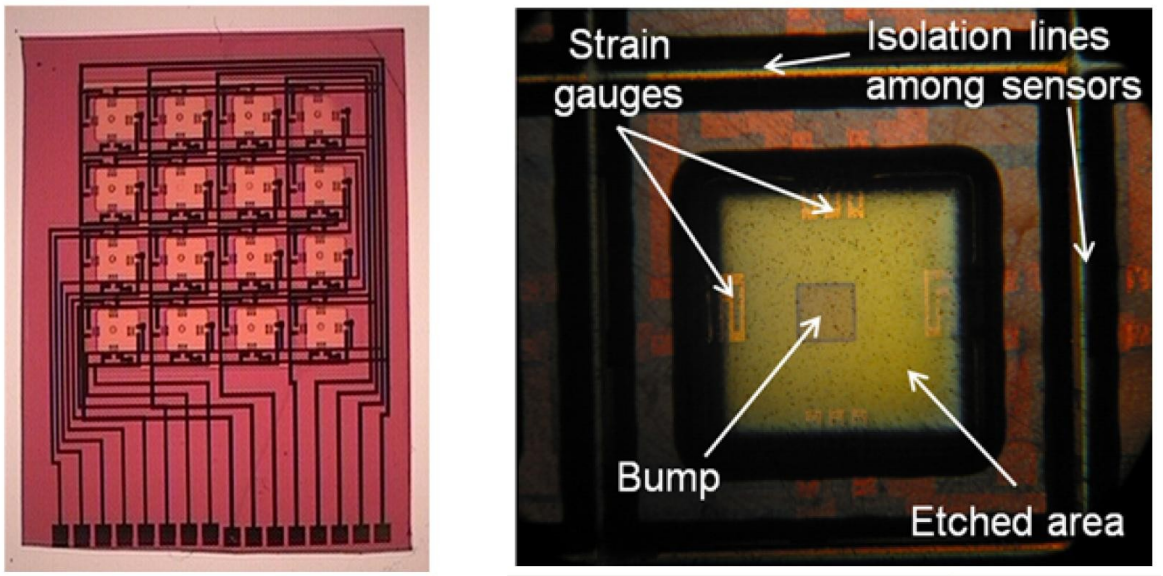

Figure 1.2.15 Tactile sensor using wet-etched polyimide film [43].

K. Kim et al. [45] have fabricated a 32×32 array flexible resistive tactile sensor using the etch-release method with temperature compensation (see Figure 1.2.16).

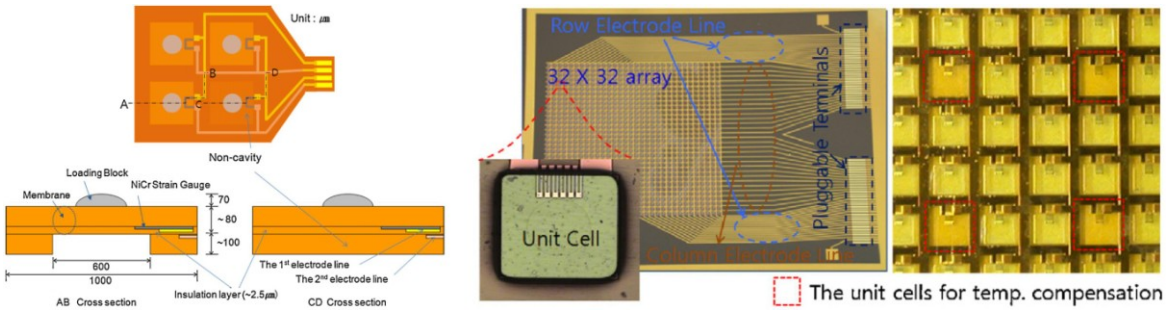

Figure 1.2.16 Tactile sensor using etch-release method with temperature compensation [45].

Hybrid-type tactile sensors

Recently, silicon-polymer-combined hybrid-type tactile sensors have been reported [46-50]. Jiang et al. [46] have developed a 2-dimensional flexible shear-stress sensor array composed of many silicon islands that are interconnected by two layers of polyimide. K. Kim et al. [47] have fabricated

a 3-axis flexible tactile sensor composed of a chip-level silicon sensor array mounted on silicone rubber as a protective layer (see Figure 1.2.17).

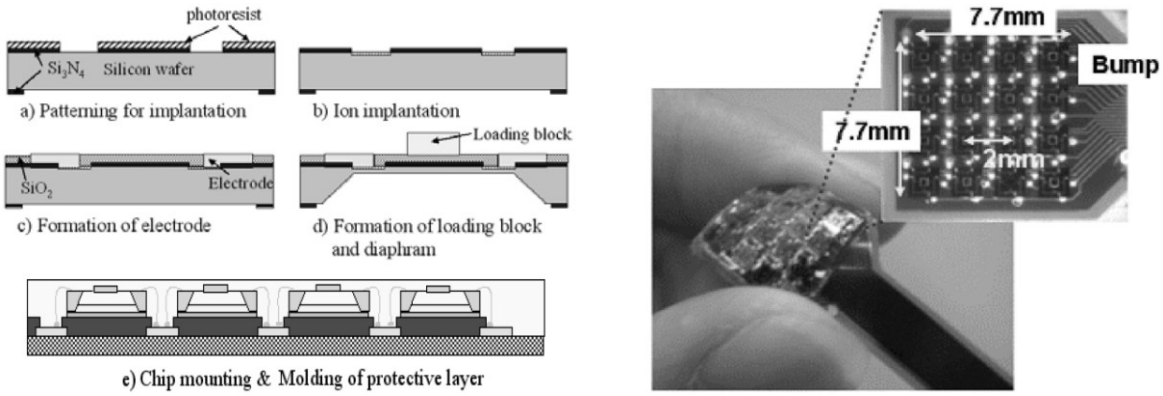

Figure 1.2.17 3-axial tactile sensor array consists of silicon sensor chip mounted silicone rubber [47].

Wen et al. [48] have developed three axes tactile sensor consists of polymer membrane (PDMS) and four sensing cantilevers with piezoresistors on both top and side walls (see Figure 1.2.18).

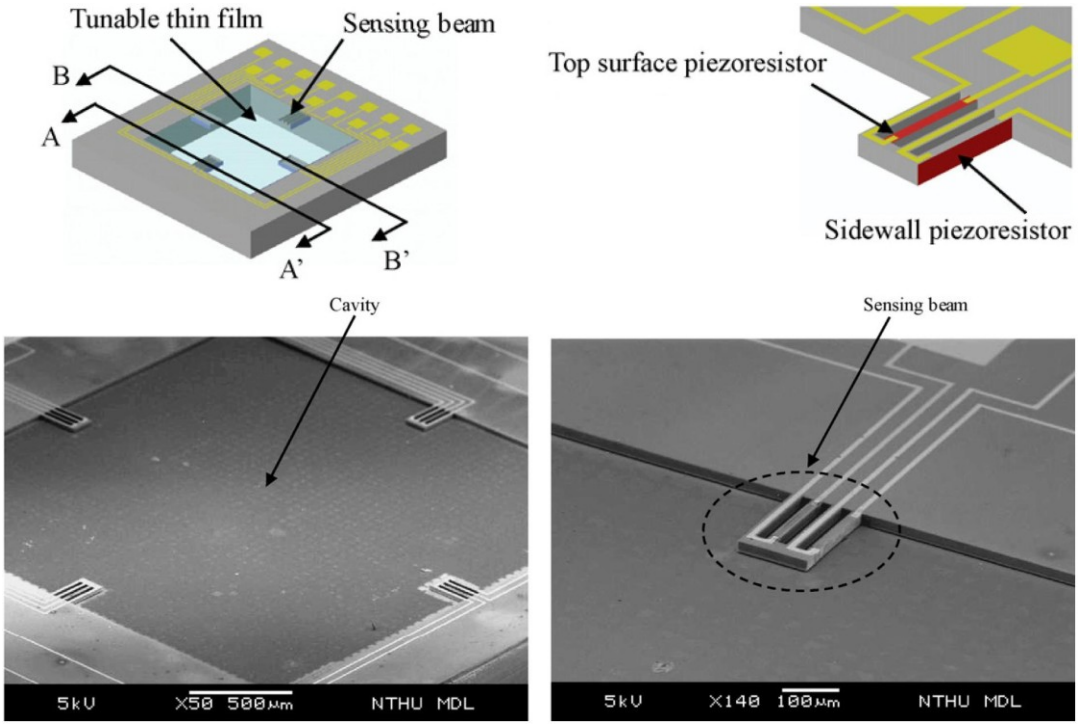

Figure 1.2.18 3-axial tactile sensor composed of polymer membrane and four sensing cantilevers [48].

Noda et al. [49] have fabricated a shear-stress sensor composed of a standing piezoresistive cantilever in an elastic material (PDMS) (see Figure 1.2.19).

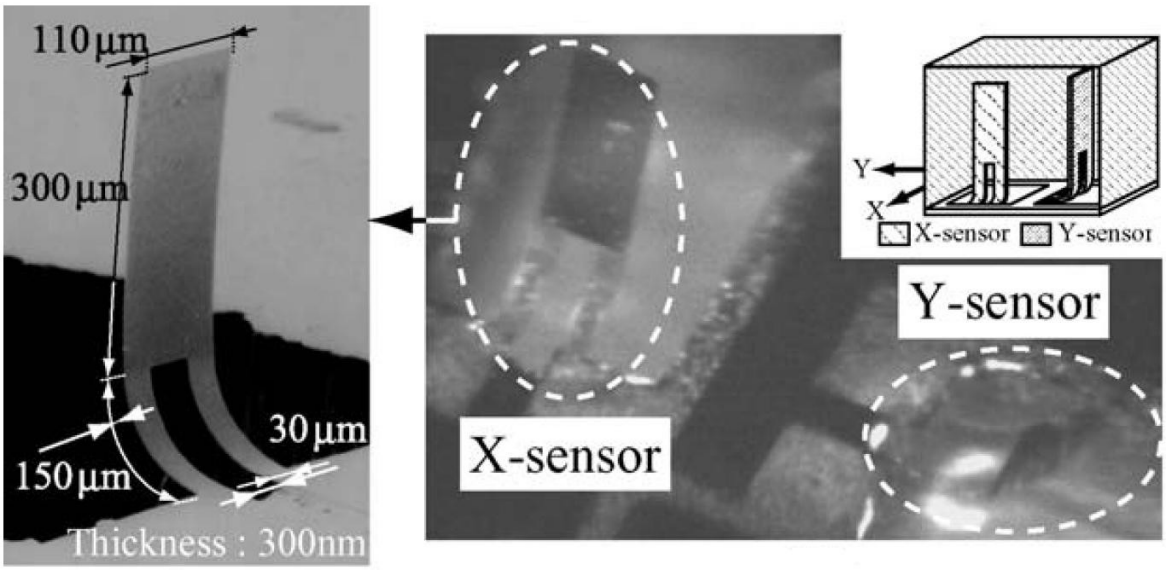

Figure 1.2.19 shear-stress sensor composed of standing piezoresistive cantilever in the elastic material [49].

Onishi et al. [50] have developed a 3-axial tactile sensor consisting of micro-cantilevers covered with elastomer (PDMS) (see Figure 1.2.20).

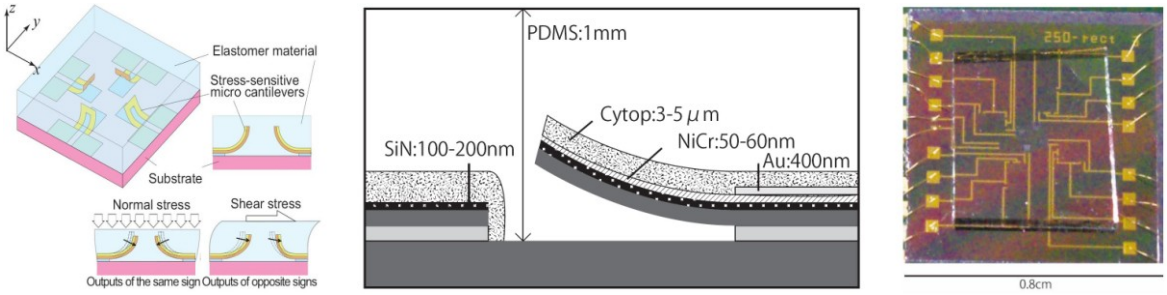

Figure 1.2.20 3-axial tactile sensor composed of four micro-cantilevers covered with PDMS elastomer [50].

1.2.2 Problems of previous studies

Characteristic feature and drawbacks of previously developed tactile sensor

Many types of tactile sensors have been developed in various ways, but these sensors have limitations. Although silicon-micromachined tactile sensors have high sensitivity and triaxial force detection, they are not flexible. Silicon is mechanically brittle, so it cannot sustain large deformations and sudden shocks [8]. Additionally, a rigid silicon substrate makes it difficult to cover contoured surfaces [8, 40]. The characteristics of silicon-based tactile sensors makes it difficult to apply them in wide variety of domains and, at the same time, increases development cost [40].

Meanwhile, other approaches are using change of capacitance or conductive polymer films [36-39]. Polymer-micromachined tactile sensors using PDMS have the advantage of array expandability, but these sensors are capable of measuring only a normal force component except in cases described by H. K. Lee et al. [37] and Hwang et al. [51]. Even if these types of tactile sensors are beneficial in terms of low development cost and higher flexibility, they still have two drawbacks: low sensitivity and poor spatial resolution. To overcome these drawbacks of the silicon-based and polymer-based approaches, “hybrid tactile sensors”—combining silicon and polymers—have recently been developed [46-50]. Various other types of tactile sensor, including optical ones, have been developed [32-33].

Although flexible polymer-based tactile sensors are being increasingly reported (see Table 1.2.1), it is still a great challenge to implement three-axial force detection with a small and flexible tactile sensor.

Table 1.2.1 Comparisons on selected multi-component miniaturized tactile sensors.

Device	Description (materials)	Sensing unit	No. of axes	Flexibility	Unit taxel size (L×W×H)	Force range (normal)	Force range (shear)	Resolution (normal)	Resolution (shear)
Kane et al. [22]	silicon membrane made by CMOS	polysilicon piezoresistors	3	×	0.3×0.3×0.1 mm	35 kPa	60 kPa	1.59 mV/kPa	0.32 mV/kPa
Mei et al. [23]	silicon diaphragm made by CMOS	polysilicon piezoresistors	3	×	4×4×1.5 mm	50 N	10 N	13 mV/N	2.3 mV/N
Valdastri et al. [25]	silicon bridge and pillar made by DRIE	polysilicon piezoresistors	3	×	2.3×2.3×1.3 mm	0.5~2.5 N	0.1~0.4 N	2.6 %/N	5.4 %/N
Lee et al. [37]	sandwich-like PDMS layers	metal capacitors	3	O	2×2×1.2 mm	10 mN	10 mN	2.9 %/mN	2.5 %/mN (x) 3.0 %/mN (y)
Hwang et al. [51]	polyimide layers with SU-8 bump	metal strain gauges	3	O	1.2×1.2×2 mm	< 4 N	< 1.5N	7 mV/N	0.4 mV/N
Kwon et al. [43]	polyimide membrane made by wet etching	metal strain gauges	3	O	2.5×2.5×0.3 mm	< 0.6 N	< 0.6 N	207 mV/N	70 mV/N
Kim et al. [47]	silicon diaphragm interconnected by PCB	polysilicon piezoresistors	3	O	2×2×0.7 mm	< 2N	< 2N	2.1 %/N	0.5 %/N
Onishi et al. [50]	silicon cantilevers covered by PDMS	metal strain gauges	3	×	1×1×1.5 mm	50~250 kPa	< 100 kPa	4 mV/kPa	6 mV/kPa (x) 1 mV/kPa (y)
Human spec.			3	O	2×2×2 mm	< 1 N	< 1 N	< 0.05 N	< 0.05 N
Target of this study			3	O	2×2×0.25 mm	< 1 N	< 1 N	7.5 %/N	2.5 %/N

1.3 Objective and approach to study

Purpose of this study is the realization of a flexible triaxial tactile sensor that has good sensitivity to equip an intelligent robot fingers, and development of a new fabrication approach for a three-dimensional structure.

(1) To accomplish a goal, we propose a new type of tactile sensing pad. It has a three-dimensionally designed, small and thin structure with unique top-head to increase the sensitivity of the sensor. A table-shaped epoxy sensing plate with four legs is built on top of a flexible and thin polymer substrate.

(2) The locations and shape/size of the strain gauges are determined by using the strain distribution obtained from FEA simulation in order to maximize the sensitivity of the sensor.

(3) The normal and shear forces could be detected by combining responses from metal strain gauges on the polymer substrate.

(4) We also present a new thermo-compatible layer-by-layer process for polymer-micromachining without wet/dry etching that is able to make a three-dimensional structure by using a thick sacrificial layer. These new approaches in surface micromachining technique based on a photodefinable polymer material are expected to contribute in polymer micromachining technology.

(5) The fabricated flexible tactile sensor is calibrated under normal and tangential forces by using the evaluation apparatus.

This thesis is composited as follows:

Chapter 1 "Introduction" is an introduction that provides state of the art and demand for tactile sensor in intelligent robot field including detail review of development of previous studies. Then it shows the purpose and approach of this thesis.

Chapter 2 "Table-shaped tactile sensor" describes the design of the proposed tactile sensor starting conception of human mimetic tactile sensor. Conceptual designs are examined among various possibilities by using FEA.

Chapter 3 "Simulation of force detection" describes the force detection algorithm for a decoupling of three-dimensional force by combining two-dimensional mapping data on the basis of strain distribution.

Chapter 4 "Polymer-micromachining" focuses on new approaches in polymer-micromachining technology. Especially, it is described the reason why it moved to polymer-micromachining from silicon-micromachining and problems of the current issues are presented, also. As the solution for the issues, thermo-compatible layer-by-layer process and fabrication of three -dimensional structure using a thick sacrificial layer is proposed.

Chapter 5 "Sensor fabrication" exhibits the process of tactile sensor with table-shaped sensing pad. In particular, fabrication process is shown in detail.

Chapter 6 "Measurement" describes measured directional force results and data analysis of fabricated sensor experimentally.

Finally, summary and future works of this dissertation are presented in Chapter 7 "Concluding remarks".

Chapter 2

Table-shaped tactile sensor

2.1 Conceptual design and principle

2.1.1 Human mimetic tactile sensor

Three components of contact force are generated when a human fingertip and an object come into contact. One component is a force normal to the interface, and the others are shear forces tangentially parallel to the interface. The tangential component of the grasping force is particularly important from the viewpoint of slip detection [22, 52]. The robot's sensory systems have been developed by mimicking human systems and are intended to replace human senses in dangerous or sensitive circumstances. The tactile sensors used for the fingertips of a robot hand must control and manipulate the grasping force on some objects through mechanical contact [8].

To define criteria for desirable performance, the following specifications for a tactile sensor similar to human skin were referenced: a spatial resolution of 2-mm (the approximate minimum separation at which human fingertips can distinguish two points applied to the skin as separate stimuli); and a threshold sensitivity of approximately 0.05 N as a force-sensing element; and stable and repeatable sensor response [9, 52-56]. Based on these requirements, the design specifications of a tactile sensor based on three-component resistance-type force sensors has the following design specifications: a spatial resolution of approximately 2-mm; a sensor curvature of less than 8-mm and normalized force capacity of approximately 1 N (see Table 1.1.2) [9, 52-56].

2.1.2 Table-shaped tactile sensor and its operation principle

To amplify a contact stress, a tactile-sensing pad has a three-dimensional, small and thin structure with a table-shaped top-head. A schematic diagram and cross-sectional view of the table-shaped sensing pad is shown in Figure 2.1.1. A polymer material (SU-8) was used as the three-dimensional structure of the contact plate and four force-transfer pillars built on the surface of a thin polymer substrate to maximize the sensitivity of the sensor. This structure could effectively convert an external acting force into concentrated internal stress. In addition, table-shaped structure could condense well-decoupled force images along each axis to a limited area, functioning as leverage. A three-component force signal, defined as a normal force and tangential forces, could be detected by combining the responses from metal strain gauges, which are located under the column as fulcra on the polymer substrate. Although the sensor has a simple design and intuitive table-shaped structure, a force detecting algorithm that avoids interference is expected.

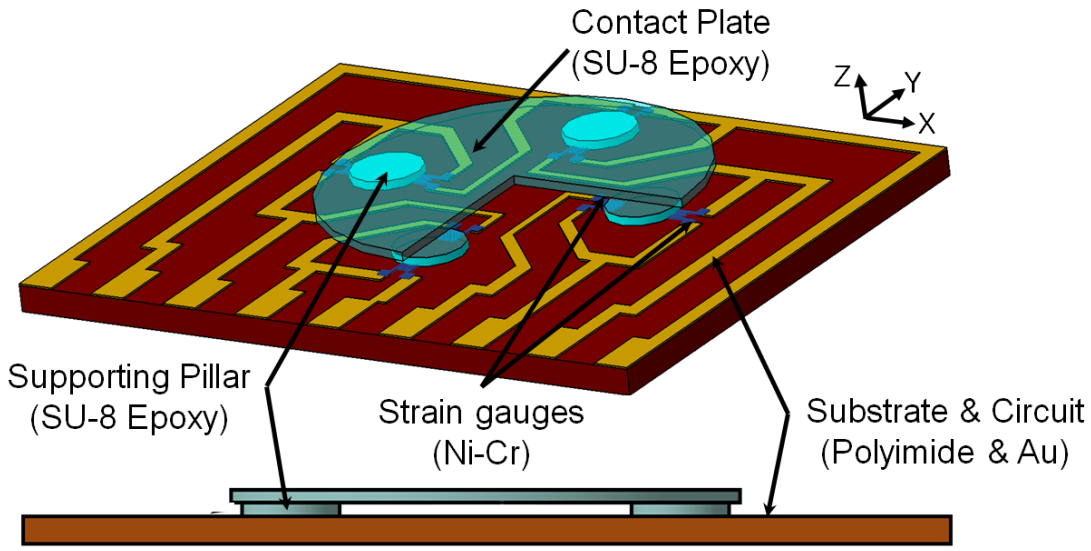

Figure 2.1.1 Schematic diagram and cross-sectional view of the proposed table-shaped tactile sensor.

2.2 Operation by FEA analysis

A table-shaped epoxy sensing plate with four legs was built on the surface of a thin polymer substrate to maximize the sensitivity of the sensor. The design of the sensor was determined by a commercial finite element analysis (FEA) program, i.e., ANSYS Ver. 11. We suppose structural modeling in the elastic region of the simplified two-dimensional cross-section. Because it is meaningless for a sensor, we do not consider the deformation for the plastic zone.

Structure modeling

To design the structure, a commercial FEA program was used to verify the design of the sensing element. We use a model consisting of a surface contact plate and four force-transfer supporting pillars on a substrate. The bottom surface of the substrate is assumed to be fixed as a boundary condition. The constrained substrate and the table-shaped structure were divided by the tetrahedral mesh (Fig. 2.2.1).

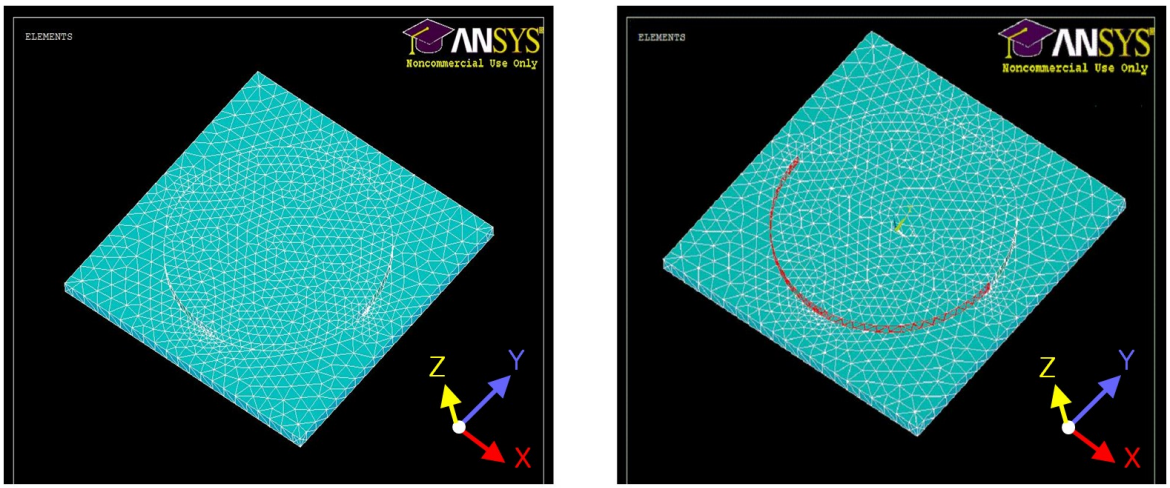

Figure 2.2.1 Tetrahedral mesh (A) and semi-cylindrical side surface of the contact for applying tangential force F_y.

Design of tactile sensing pad for maximum sensitivity

Configuration of strain gauges is carefully investigated to set the area of highest strain. Since the external force applied to the sensing plate is transmitted to the substrate through the force-transfer columns, most strain changes on the substrate appear on the bottom of the strained columns. From the results of the FEA analysis, it is clear that the strain-sensing elements in the tactile sensor must be placed at the periphery of the columns. Figure 2.2.2 shows deformation of the upper plate (A) and the strain distribution result along the inner edge of the column base (B). When normal load F_z is uniformly applied to the top surface of the contact plate increasing from 0 to 0.1 N along the z-direction, the simulation result shows a center-biased symmetrical strain distribution to the origin of the contact plate.

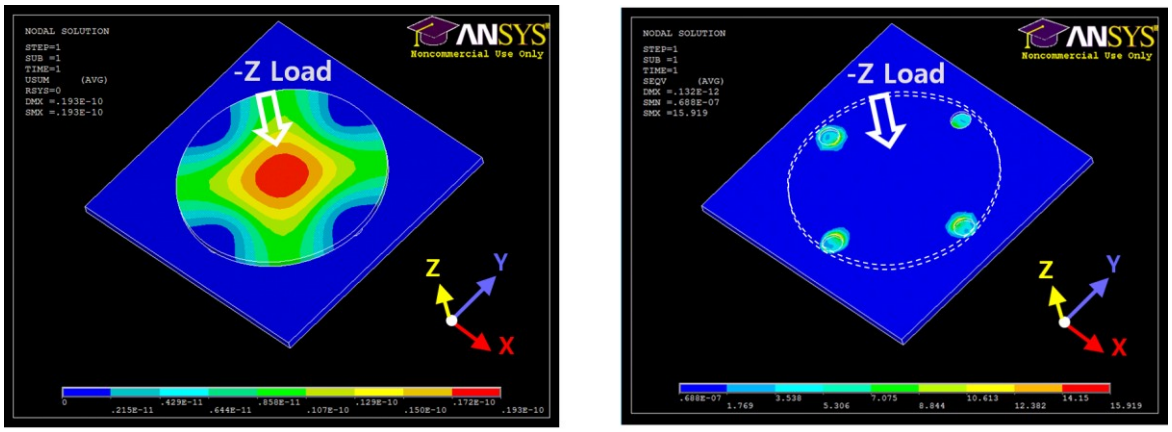

Figure 2.2.2 Deformation of the upper plate (A) and strain distribution of the substrate (B) under normal (-z) load.

In the case of tangential load, F_y is applied to the semi-cylindrical side surface of the contact plate increasing from 0 to 0.1 N along the y-axis. The tangential force was applied along the dotted black line divided by the number of mesh nodes (see Fig. 2.2.3(B)). The simulation result shows strain distributions along the y-axis are biased to the loading direction (+y) and along the x-axis are biased to the origin of the upper plate. This asymmetric feature coincides with the intuitively expected result since four legs (transfer columns) under the upper plate are constrained each other by the upper plate.

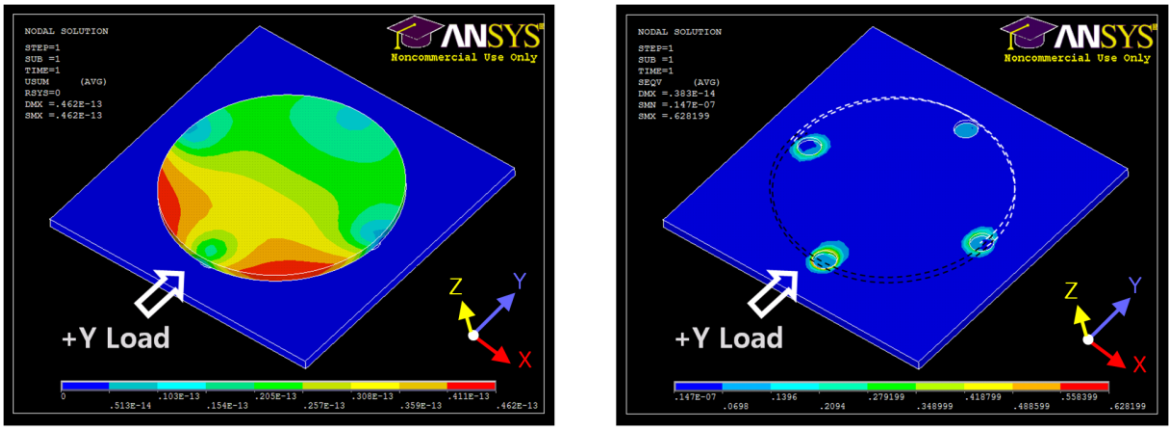

(A) (B)

Figure 2.2.3 Deformation of the upper plate (A) and strain distribution of the substrate (B) under tangential (+*y*) load.

2.3 Structural design

2.3.1 Strain gauges

In this research, resistance-type tactile sensor is used. A strain gauge can convert an external force to change of resistance as an internal strain. To maximize the sensitivity of the sensor, the locations of the strain gauges were determined by the strain distribution obtained by finite element analysis (FEA). The strain distribution was then used to determine the shape of the strain gauge and its size.

Geometry of the strain gauges

Let us consider circle '*A*' enclosed by an inscribed polygon (IP) and a circumscribed polygon (CP), as shown in Figure 2.3.1(A). If subtended angle θ is small, we can consider a curve (arc) as a line (chord), which is called 'straight-line approximation'. This concept is very useful for determining the size and configuration of the strain gauges. To reduce structural error, linearization of the contact line between the strain gauge and the column is required. When the center of the measuring grid of a strain gauge is located under the edge-line of the column, the actual contact line of the strain gauge and the column is the arc of circle *A*'s subtended angle θ. In this case, a chord of CP is the 'effective area (EA)' for the angle θ, because a distance '*e*' between the chords of IP and CP is the error of circle *A*'s arc subtended by angle θ. In the case of dodecahedrons, an error of 'EA' and the real length of circle *A*'s arc subtended by the angle 30° is 3.4 % of radius *r*, see Figure 2.3.1(B).

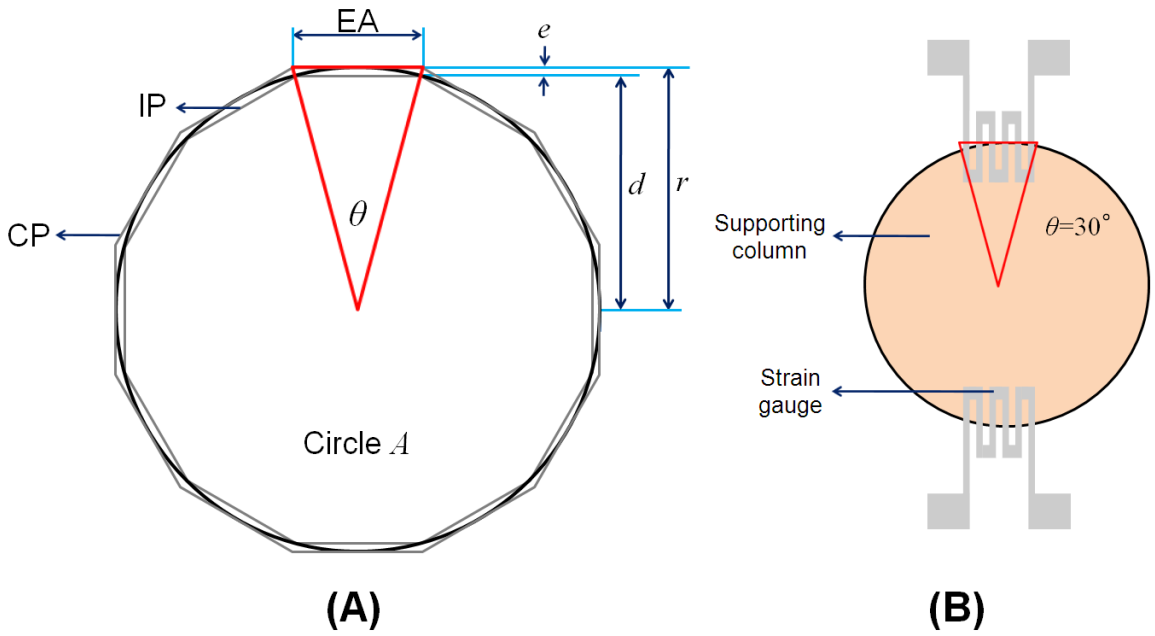

Figure 2.3.1 (A) Straight line approximation. (B) Configuration of strain gauge applied straight line approximation.

Scale of the strain gauges

The designed strain gauges have a serpentine trace of nickel-chrome-alloy in a 110×110-μm square measuring grid area. The line-width of the measuring grid (10-μm) is determined by the finest width that can be deposited on the polymer substrate by the mask aligner (PEM-800, Union Optical Co. Ltd.) under well-controllable conditions. To avoid transverse strain, the region of the transverse connections (end loops) has a 20-μm line-width [57]. Moreover, to satisfy the maximum active gauge length for the highest strain measuring, the active length of the measuring grid (110-μm) is determined by considering half of the column's notch radius (220-μm) [57-58]. The total grid width of the strain gauge (110-μm) is determined by straight-line approximation of the column's radius (220-μm) (Figure 2.3.1 (B)). From the FEA simulation results, the maximum strain is distributed into ±55-μm under the edge line of the column (in detail, see chapter 3.2). Figure 2.3.2 shows the determined size of the strain gauge.

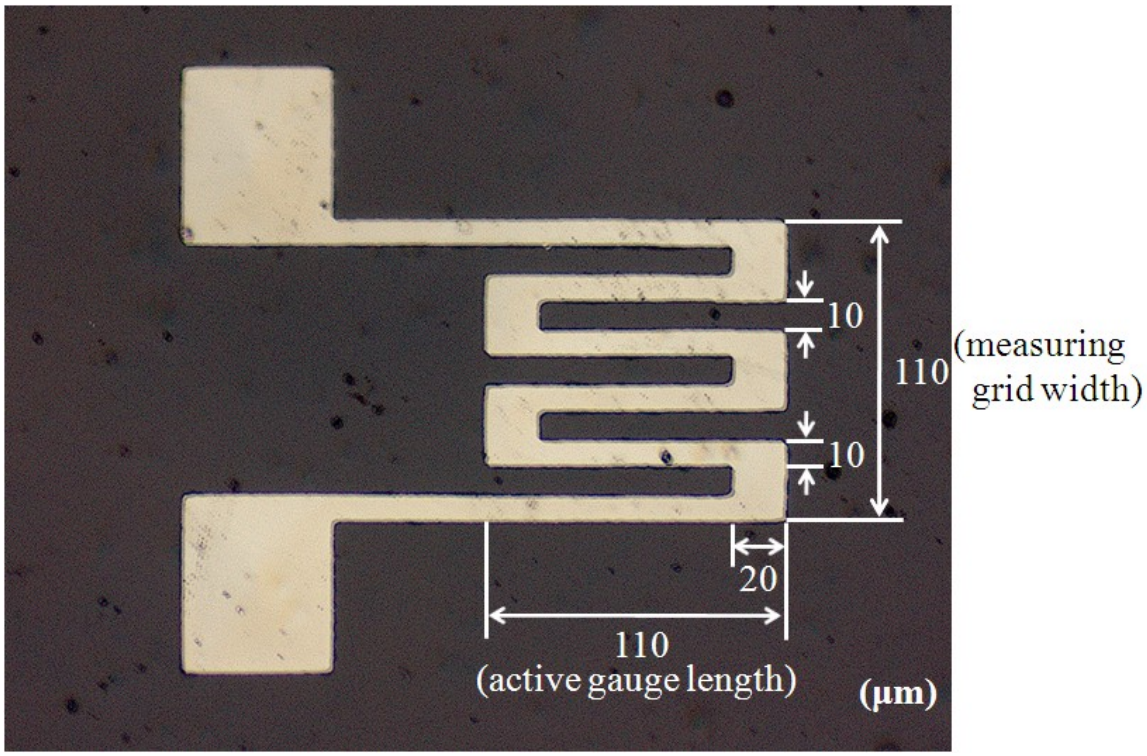

Figure 2.3.2 Specification of designed strain gauge.

2.3.2 Structure configuration

Determining diameter of contact plate and supporting column

Based on the referenced specifications for a tactile sensor (chapter 2.1.1), we consider a circular sensing pad with a radius of approximately 1-mm following the spatial resolution of the human fingertips. A circle exhibits perfect symmetry in every direction, in contrast to a square, which experiences a distortion caused by the dissipation or concentration of force transmission at the vertex of the square. Therefore, a circular shape is used for the sensing pad. Let us consider the table-shaped structure as a sensing element that has a contact 'plate' and four force-transfer 'columns'. We investigated various combinations of sensing element sizes using a finite element method (FEM) simulation.

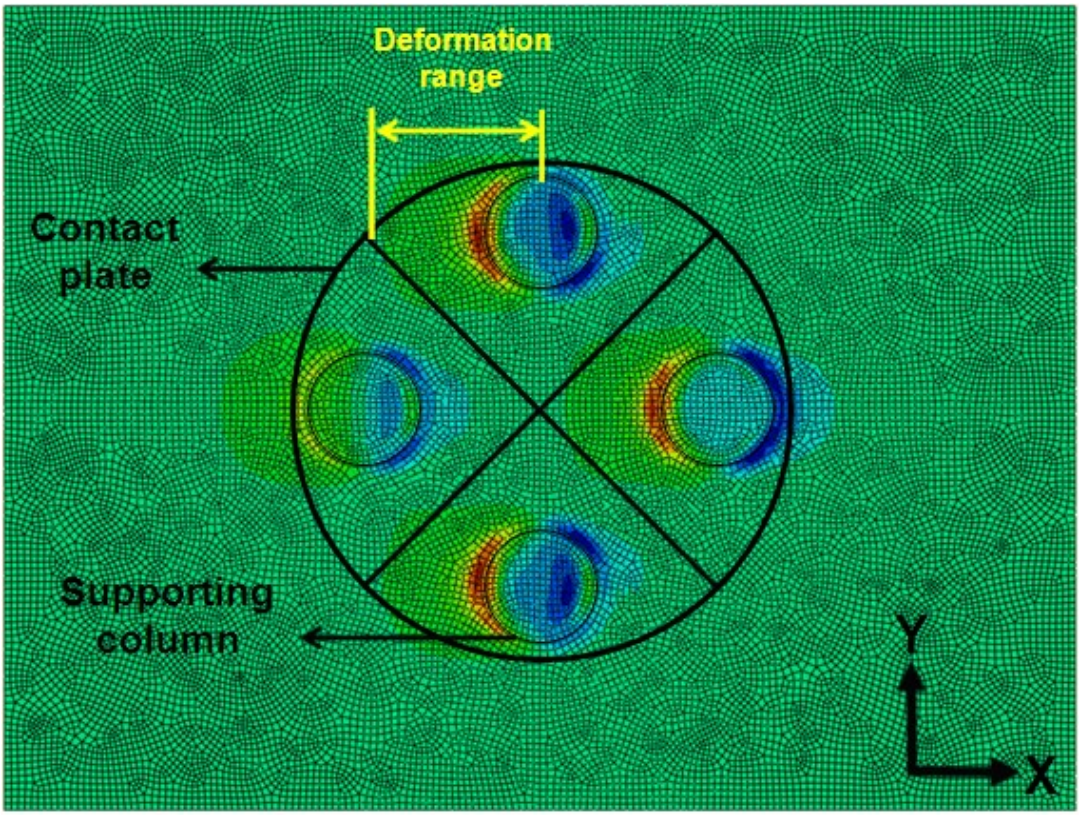

Figure 2.3.3Deformation ranges which have ±3 times of column radius around an origin of each column.

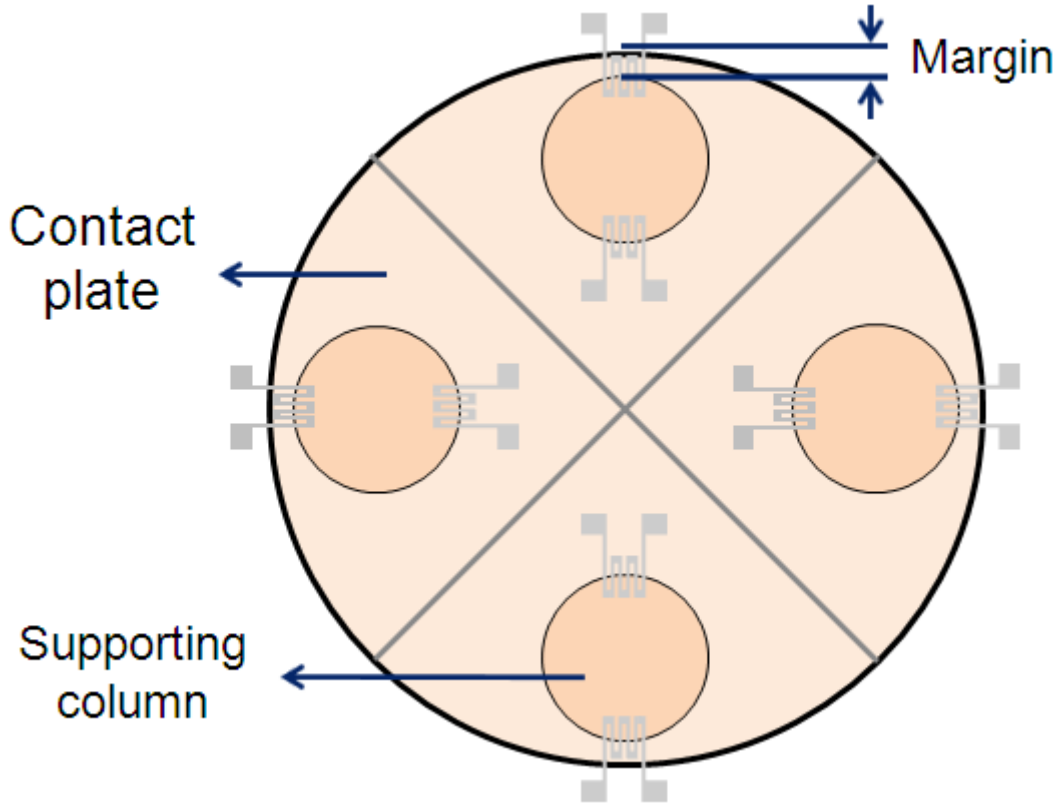

Figure 2.3.4 Symmetrically determined configuration of strain gauge and force-transfer columns applied by tetragonal area partitioning.

Most of the results are restricted by deformation ranges (~660-μm) which have ±3 times of column radius around an origin of each column against a targeted maximum loading of 1 N (Figure 2.3.3). To avoid interference of the output signals caused by overlapping of the deformed area of each independent column, the size and configuration of the force-transfer columns are symmetrically determined by tetragonal area partitioning to minimize influence on the strain gauges under the neighboring column (Figure 2.3.4). Therefore, the determined column diameter (440-μm) is approximately half of the contact plate's radius (935-μm). The edge of the contact plate has a margin (a 55-μm ring) that is designed to minimize misalignment problems caused by different coefficient of thermal expansion (CTE) of the polymer materials (SU-8: 52 ppm/°C) [59].

Determining height of support column and thickness of contact plate

To determine the appropriate height of the support column, we set the maximum height to 90-μm, which is the limit height of well-controllable three-dimensional microfabrication. Then, we choose three cases, 30-, 60-, and 90-μm, as candidates for the height of the support column. From the results of FEA, Figure 2.3.5 shows the decrease and increase of the maximum change of the strain according to the height of the support column. When a normal force (F_z) is applied to the sensing pad, the maximum change of the strain decreases as the height increase (Figure 2.3.5(A)). However, in the case of tangential force (F_y) loading, the maximum change of the strain increases with the height of the support column (Figure 2.3.5(B)). Therefore, to satisfy every case, the intermediate height value, 60-μm, is chosen.

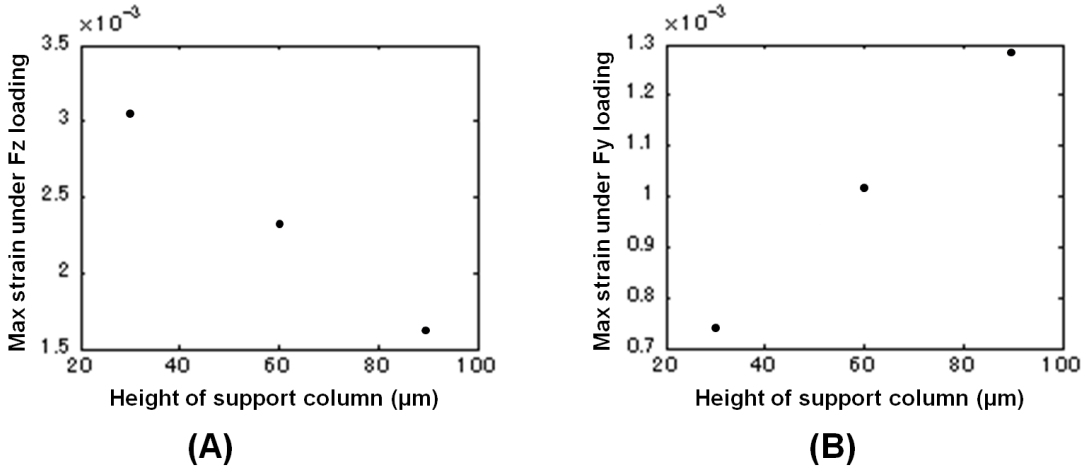

Figure 2.3.5 The maximum change of the strain under normal loading F_z (A) and tangential loading F_y (B) according to the height of support column.

To determine the appropriate thickness of the contact plate, we analyze through FEA in a similar way. When a normal force (F_z) is applied to the sensing pad, the maximum change of the strain decreases as the thickness increases (Figure 2.3.6(A)). However, in the case of tangential force (F_y) loading, the maximum change of the strain increases with the thickness of the contact plate (Figure 2.3.6(B)). Therefore, to satisfy every case, the intermediate height value, 60-μm, is chosen.

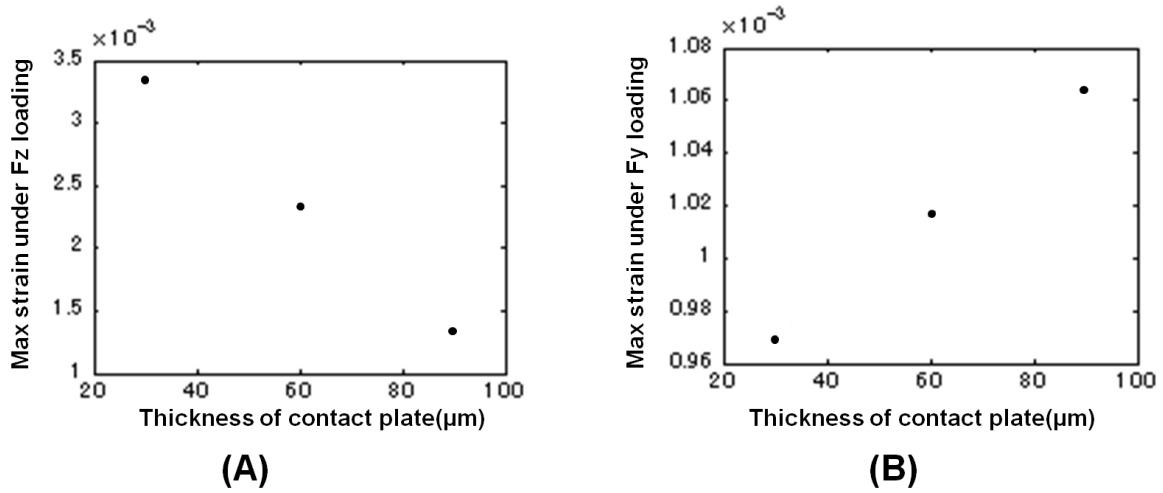

Figure 2.3.6 The maximum change of the strain under normal loading F_z (A) and tangential loading F_y (B) according to the thickness of contact plate.

Specification of designed tactile sensor

The designed tactile sensor consists of a 60-μm-thick, 1870-μm-diameter upper plate as a sensing element and four 60-μm-high, 440-μm-diameter force-transfer columns on a 125-μm-thick, 4.18×2.91-mm rectangular membrane. The membrane material is polyimide film (with a Young's modulus (E) of 2.5 GPa and a Poisson's ratio (ν) of 0.34). For the column and upper-plate materials, SU-8, which has a Young's modulus of 4.4 GPa and a Poisson's ratio of 0.22, is used (see Table 2.3.1) [59].

Table 2.3.1 Specification of designed tactile sensor.

Structure	Size	Material	Property
Upper plate	60-μm-thick 1870-μm-diameter	SU-8	E : 4.4 GPa ν : 0.22
Force-transfer columns	60-μm-high 440-μm-diameter	SU-8	E : 4.4 GPa ν : 0.22
Membrane	125-μm-thick 4.18x2.91-mm	polyimide film	E : 2.5 GPa ν : 0.34

2.3.3 Circuit design

As shown in Figure 2.3.7, four strain gauges (R_2, R_1, R_5, and R_6) along the x-axis and four additional strain gauges (R_4, R_3, R_7, and R_8) along the y-axis are arranged as pairs under the four force-transfer columns. The resistance of the strain gauges is changed symmetrically as they are physically deformed according to the applied direction of external force. Put simply, to measure the direction and magnitude of the applied external force, just four strain gauges (R_1, R_3, R_5, and R_7) inside of the contact plate are needed. The direction and magnitude of applied force could therefore be measured by combination of either increasing or decreasing the output resistance.

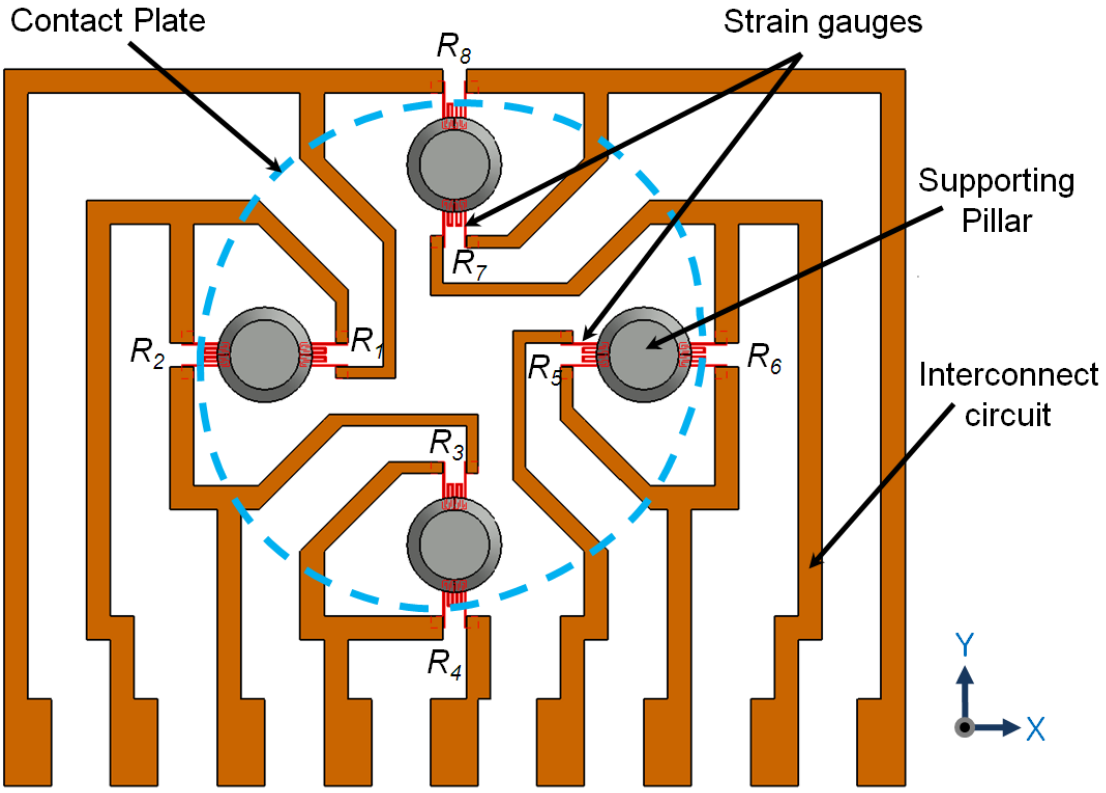

Figure 2.3.7 Schematic representation of the configuration of the resistor and interconnects. Eight strain gauges are candidates for quarter-bridge or moment-compensation circuit. Four strain gauges (R_1, R_3, R_5, and R_7) were used to measure applied normal and 2D tangential forces in this study.

2.3.4 Mask Design for photolithography

Arrangement on the polyimide substrate

One wafer process yields two 2-different types of tactile sensor. Designed sensors are arranged on the silicon substrate as shown in Figure 2.3.8. The edge circle is left blank as a margin of encapsulation between polyimide film and carrier silicon wafer (in detail, see chapter 5.2).

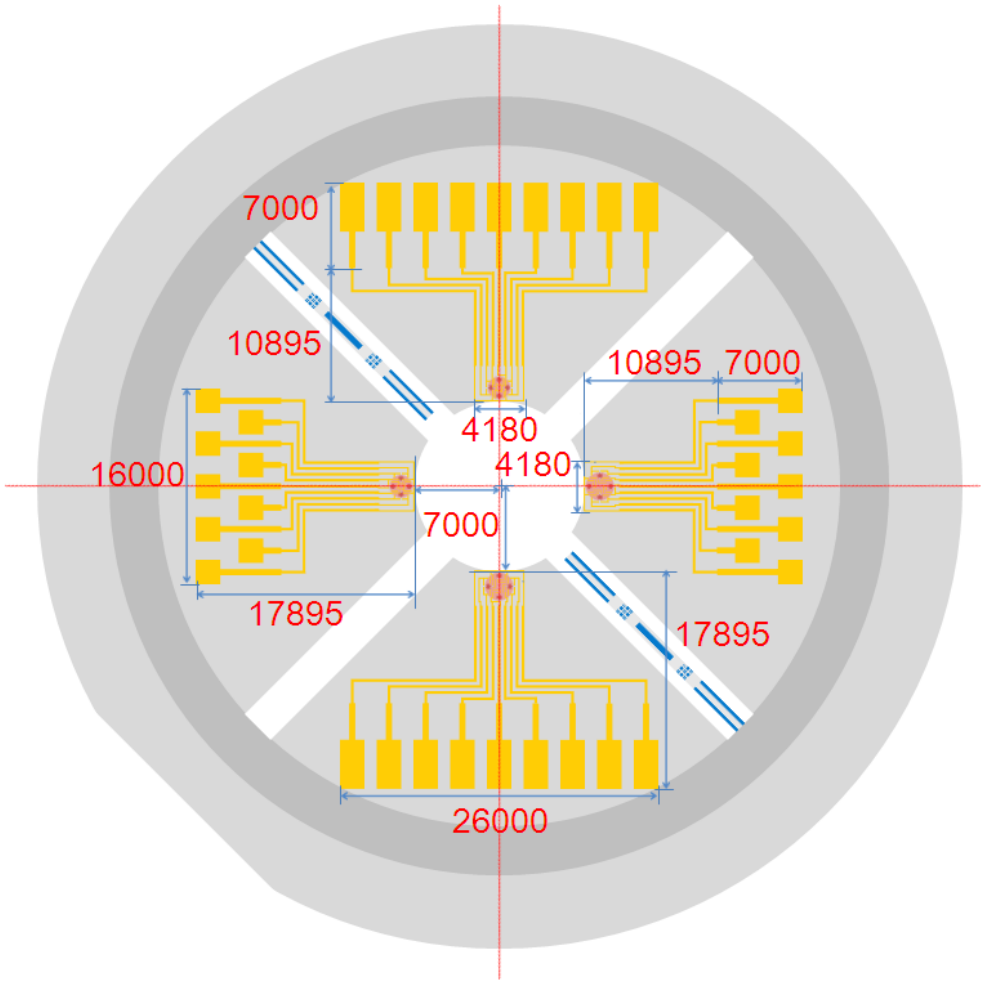

Figure 2.3.8 Arrangement on the polyimide substrate (Unit : μm).

Layout Editor as a CAD tools

A CAD (Computer-aided design) tool program, GPL(General Public License) licensed LayoutEditor™ which is a software to design and edit layouts for MEMS/IC fabrication, is used to mask design for photolithography process (see Figure 2.3.9).

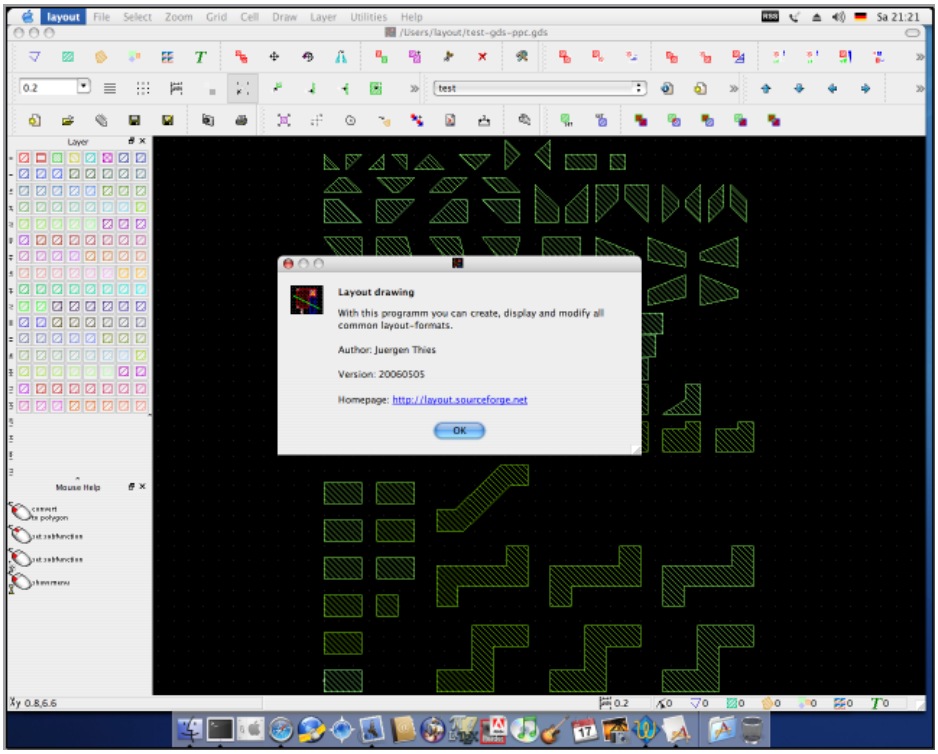

Figure 2.3.9 GPL CAD program, The LayoutEditor™.

Completion of the mask

Coarse designed layout was translated by GDSII format to applicable for chrome (mask-1) and emulsion (mask-2, -3, -4) photo masks. Photo masks consist of four pieces; strain gauges (Ni/Cr resistors; mask-1), lead lines (Au interconnects; mask-2), support pillar/sacrificial layer (mask-3), and circular contact plate (mask-4) as a table-shaped structure. When we consider characteristics of the photo resist whether positive or negative, mask-1 for metal strain gauges and mask-2 for metal lead lines are made positive photo mask because of positive-toned photo resist OFPR-800LB/100Cp (TOK).

Mask-3 for support pillar and mask-4 for circular contact plate are produced negative photo mask because of negative-toned photo-definable epoxy SU-8 3050 (Microchem). Mask-3 is also considered a role of sacrificial layer. Although sacrificial layer is used by positive-toned photo resist PMER P-HA 1300PM (TOK), it is no problem since sacrificial layer has mirror image of support pillar (see Figure 2.3.10).

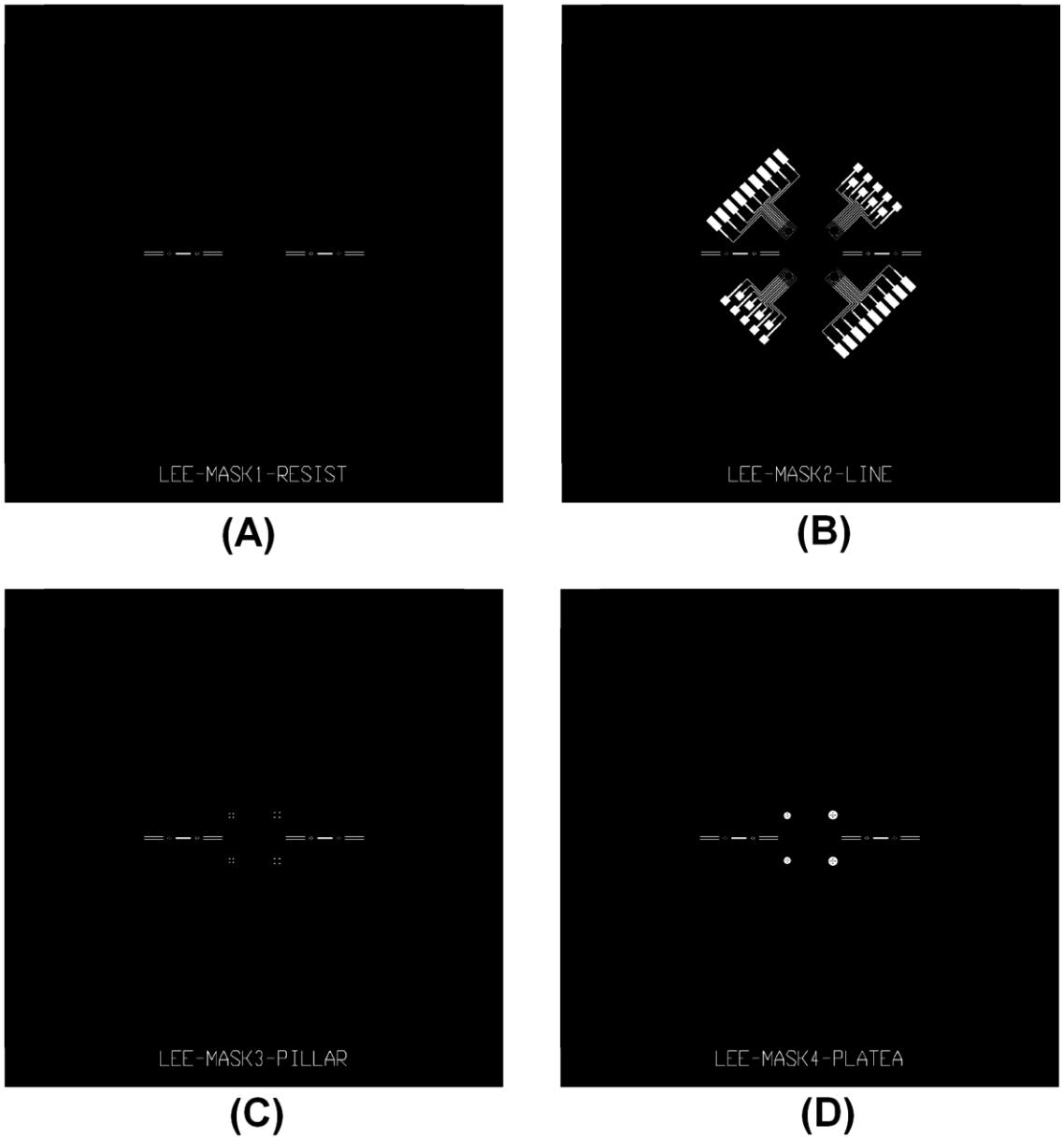

Figure 2.3.10 Fabricated photomasks for (A) metal strain gauges (Ni/Cr resistors), (B) metal lead lines (Au interconnects), (C) support pillar and sacrificial layer, (D) circular contact plate as a table-shaped structure.

Chapter 3

Simulation of force detection

3.1 Triaxial force detection

In the resistance-type tactile sensor, a strain gauge can convert an external force to change of resistance as an internal strain.

Changes of resistance of the strain gauges

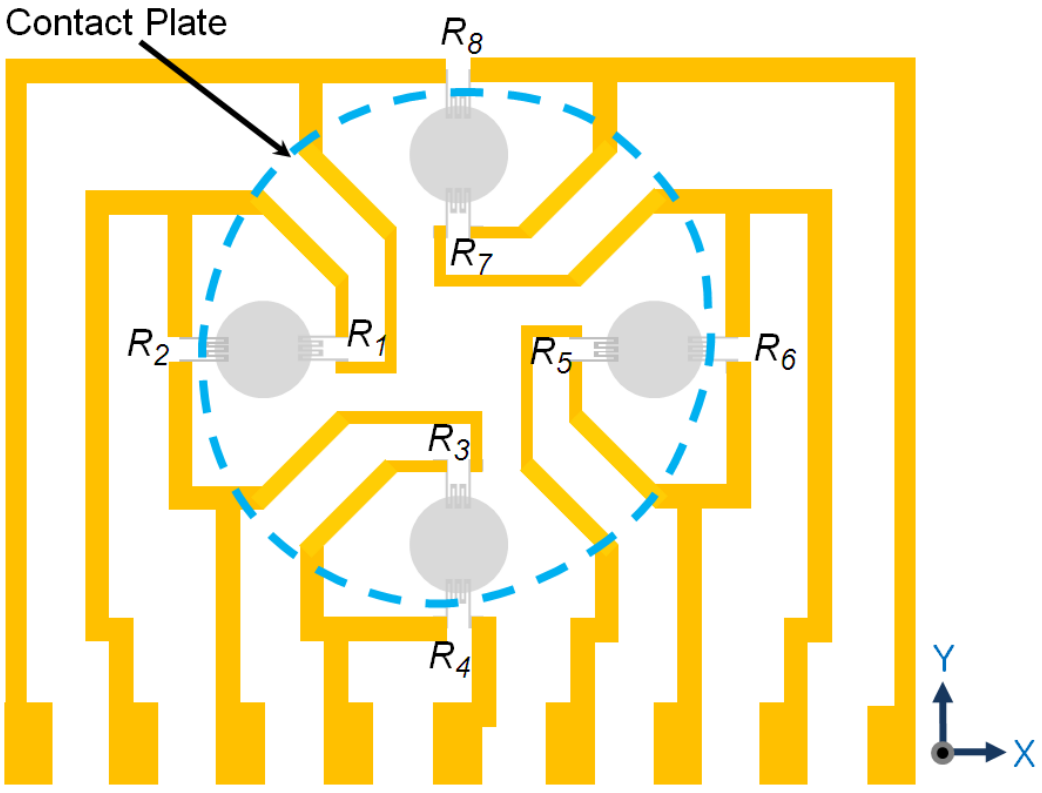

Figure 3.1.1 Schematic representation of the configuration of the resistor.

Increases and decreases in change of resistance according to direction of applied external force are listed in Table 3.1.1. In the table, "(+)" and "(-)" signs indicate increase and decrease in resistance against the initial value, respectively.

Table 3.1.1 Increase and decrease of resistance according to direction applied external force.

		Sign of the strain gauges by applying direction				
		+x	**-x**	**+y**	**-y**	**-z**
Strain gauges on the axis along the +x-direction	**R_2**	**(+)**	**(-)**	**0**	**0**	**(-)**
	R_1	**(-)**	**(+)**	**0**	**0**	**(+)**
	R_5	**(+)**	**(-)**	**0**	**0**	**(+)**
	R_6	**(-)**	**(+)**	**0**	**0**	**(-)**
Strain gauges on the axis along the +y-direction	**R_4**	**0**	**0**	**(+)**	**(-)**	**(-)**
	R_3	**0**	**0**	**(-)**	**(+)**	**(+)**
	R_7	**0**	**0**	**(+)**	**(-)**	**(+)**
	R_8	**0**	**0**	**(-)**	**(+)**	**(-)**

For example, when an external force is applied in the +x-axis direction, strain gauges R_1 and R_5 adopt compressive and tensile states, respectively. The resistances therefore decrease ((-); R_1) and increase ((+); R_5), respectively. Meanwhile, when an external force is applied in the -x-axis direction, strain gauges R_1 and R_5 adopt tensile and compressive states, respectively. These resistance changes are opposite to those in the case that external force is applied in the +x-axis direction. Note here that R_3 and R_7 lie along the y-axis and the change of resistance is negligibly small. When an external force is applied in either the ±x or ±y-axis direction, the other axial change of resistance should be designed to be as small as possible. When an external force is applied in the +y-axis direction, the resistance changes of R_3 and R_7 are decreased and increased, respectively. Here, R_1 and R_5 (lying along the x-axis) are also not physically changed. On the other hand, when an external

force is applied in the normal direction (i.e. the -*z*-axis direction) relative to the contact plate surface, the resistances of all the strain gauges (R_1, R_3, R_5, and R_7) increase.

Normalized triaxial force

The strain distributions due to the configuration of the strain gauges give the decoupling solution derived from the directional force components in the following equations. Generally, this decoupling solution has been widely applied to resistance-type tactile sensors [41-44];
for $-F_z$ loading; from strain gauge signals of R_1, R_3, R_5 and R_7:

$$\Delta R(F_{-z}) = \Delta R(R_1) + \Delta R(R_3) + \Delta R(R_5) + \Delta R(R_7) \tag{3.1.1}$$

for $+F_x$ loading; from strain gauge signals of R_1 and R_5:

$$\Delta R(F_{+x}) = \Delta R(R_1) - \Delta R(R_5) \tag{3.1.2}$$

for $+F_y$ loading; in a similar way:

$$\Delta R(F_{+y}) = \Delta R(R_3) - \Delta R(R_7) \tag{3.1.3}$$

Here, ΔR means the change of resistance of the strain gauge. The positive sign represents a tensile state, and the negative sign represents a compressive state. From Equations (3.1.1) to (3.1.3), the magnitude of loadings can be calculated. Applied loadings along the *x*-, *y*-, and *z*-axes can be estimated through calculation of the resistance change from the output signals of the four strain gauges arranged inside contact plate (R_1, R_3, R_5 and R_7). In Figure 3.1.1, the four extra strain gauges (R_2, R_4, R_6, and R_8) arranged outside of the contact plate (which are candidates for a quarter-bridge or moment-compensation circuit) are also shown. However, these extra strain gauges are not considered for force detection in this study.

3.2 Two-dimensional force mapping

3.2.1 FEA analysis

The strain distribution of the strain gauges was determined by a commercial finite element analysis (FEA) program, i.e., ABAQUS Ver. 6.10. The sensing unit that consists of a substrate and table-shaped contact plate were divided by the tetrahedral mesh (see Figure 3.2.1). The sensor was simulated by applying normal and tangential forces between zero and 1.0 N.

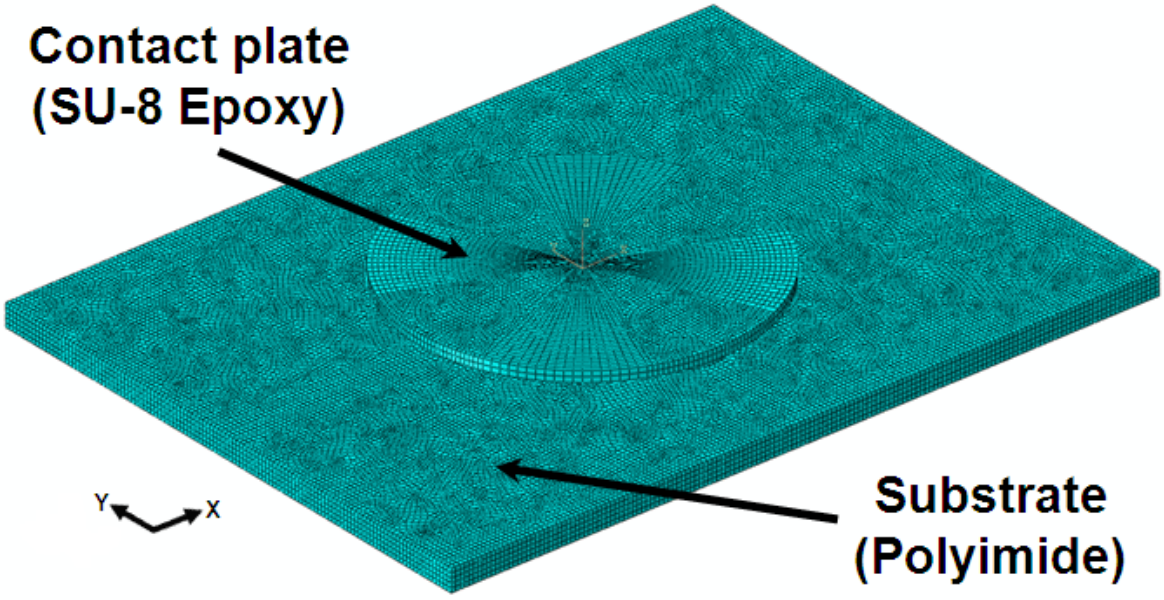

Figure 3.2.1 Tetrahedral meshes of the sensing unit for FEA analysis.

Normal loading F_z

When distributed F_z loading (applying uniform 1 N along the -z-direction) was applied to the sensor, the schematic modeling is shown in Figure 3.2.2.

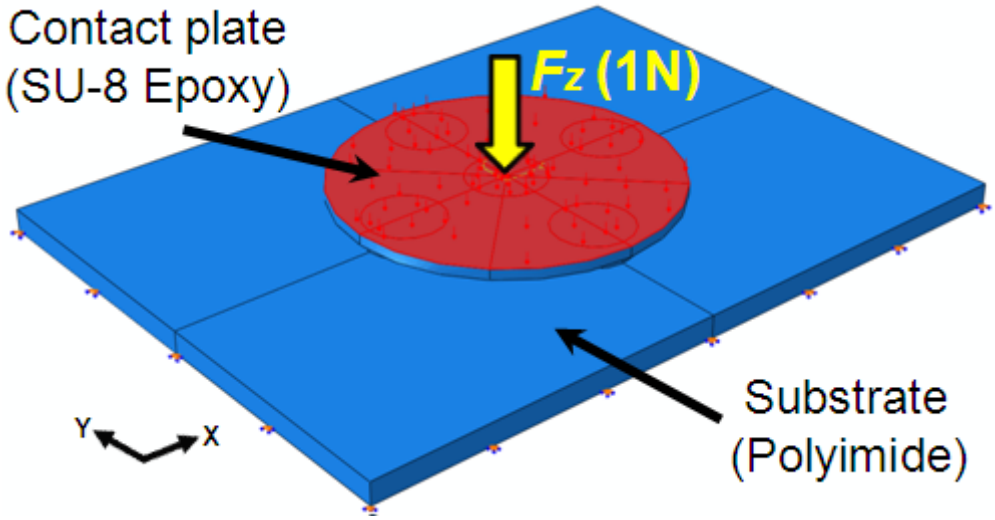

Figure 3.2.2 Schematic representation of the loading simulations for 1-N normal loading.

The analyzed FEA result shows a center-biased symmetrical strain distribution to the origin of the contact plate. Especially, Figure 3.2.3 and Figure 3.2.4 show the strain distributions against principal strain directions along +x-axis (ε_{xx}) and +y-axis (ε_{yy}), respectively. The strain gauges R_1, R_3, R_5 and R_7 (arranged inside of contact plate) take tensile and R_2, R_4, R_6 and R_8 (arranged outside of the contact plate) take compressive states. This increase ((+); R_1, R_3, R_5 and R_7) and decrease ((-); R_2, R_4, R_6 and R_8) states simply symbolized by "(+)" and "(-)" signs such as Table 3.1.1. Note here that strain distributions against principal strain direction along +x-axis (ε_{xx}) in the Figure 3.2.3, the changes of resistance R_4, R_3, R_7 and R_8 (lying along the +y-axis) are meaningless. And strain distributions against principal strain direction along +y-axis (ε_{yy}) in the Figure 3.2.4, the changes of resistance R_2, R_1, R_5 and R_6 (lying along the +x-axis) are also meaningless. Figure 3.2.5 shows the symbolized distributions by "(+)" and "(-)" signs from superposition results of the Figure 3.2.3 and Figure 3.2.4.

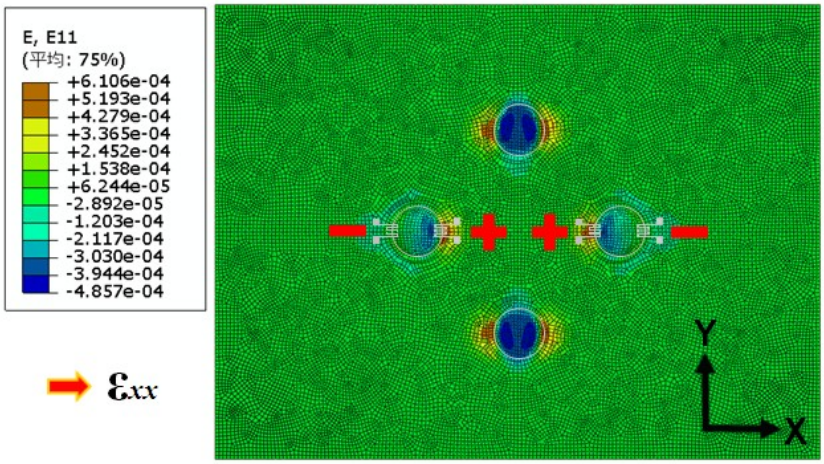

Figure 3.2.3 (ε_{xx}) strain distributions for 1-N normal loading.

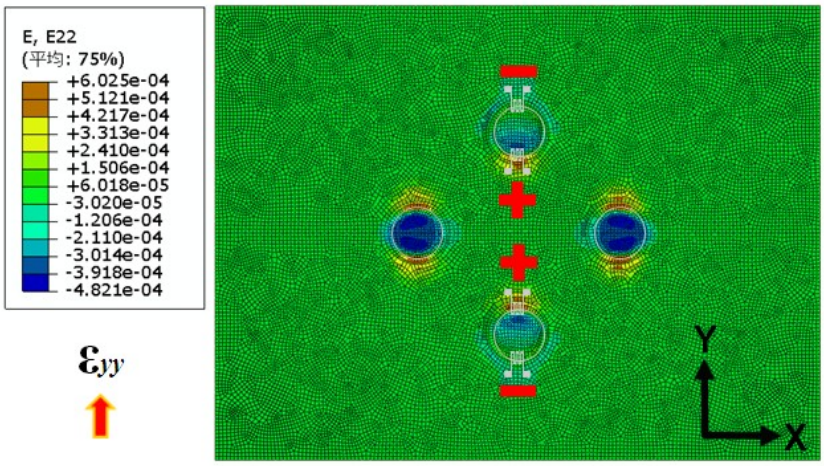

Figure 3.2.4 (ε_{yy}) strain distributions for 1-N normal loading.

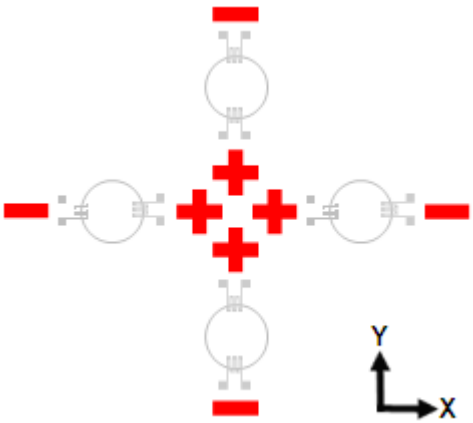

Figure 3.2.5 Schematic representation of the symbolized distributions due to application of 1-N normal loading.

Tangential loading F_x

In the case of applied F_x loading (applying uniform 1 N along the +x-direction), the schematic modeling is shown in Figure 3.2.6.

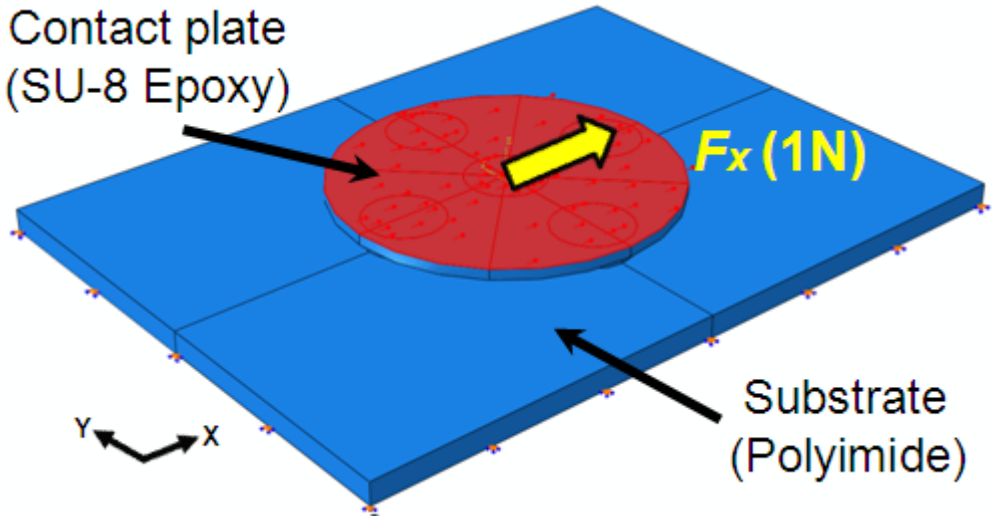

Figure 3.2.6 Schematic representation of the loading simulations for 1-N +x-direction (0°) tangential loading.

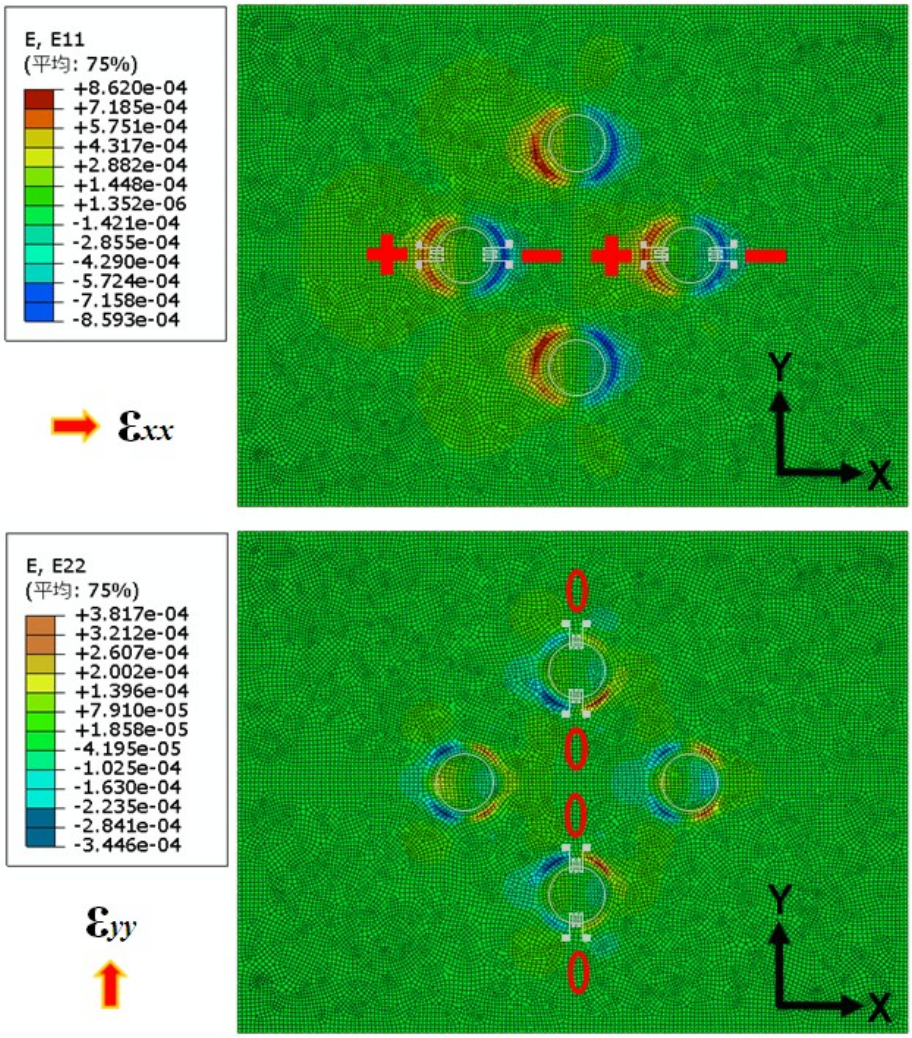

Figure 3.2.7 (ε_{xx}) and (ε_{yy}) strain distributions for 1-N tangential loading.

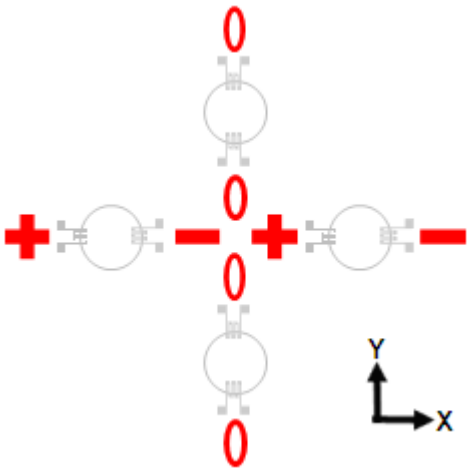

Figure 3.2.8 Schematic representation of the symbolized distributions due to application of 1-N tangential loading.

Resultant loading F_{z+x}

In the case of applied F_{z+x} loading (applying uniform 1 N along the $-z$-direction and $+x$-direction), the schematic modeling is shown in Figure 3.2.9.

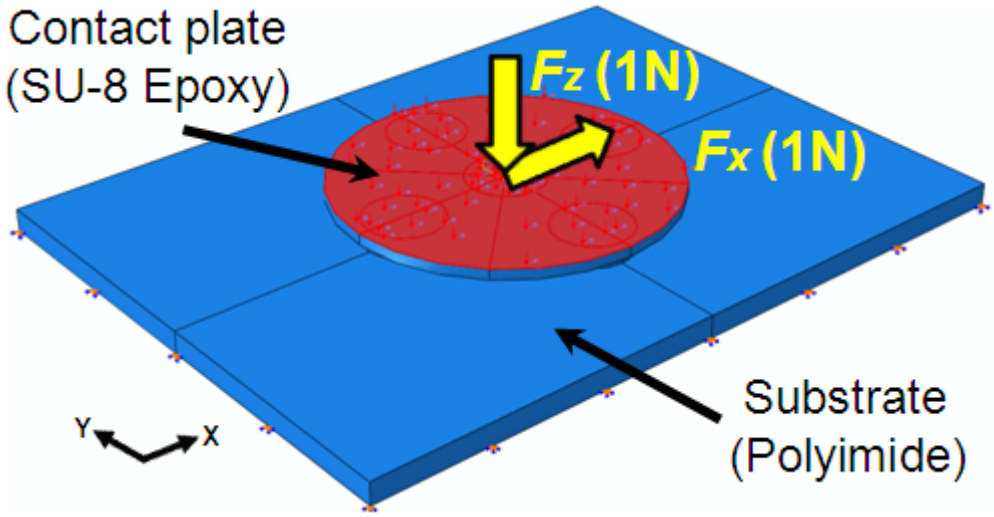

Figure 3.2.9 Schematic representation of the loading simulations for superposition of normal and tangential load.

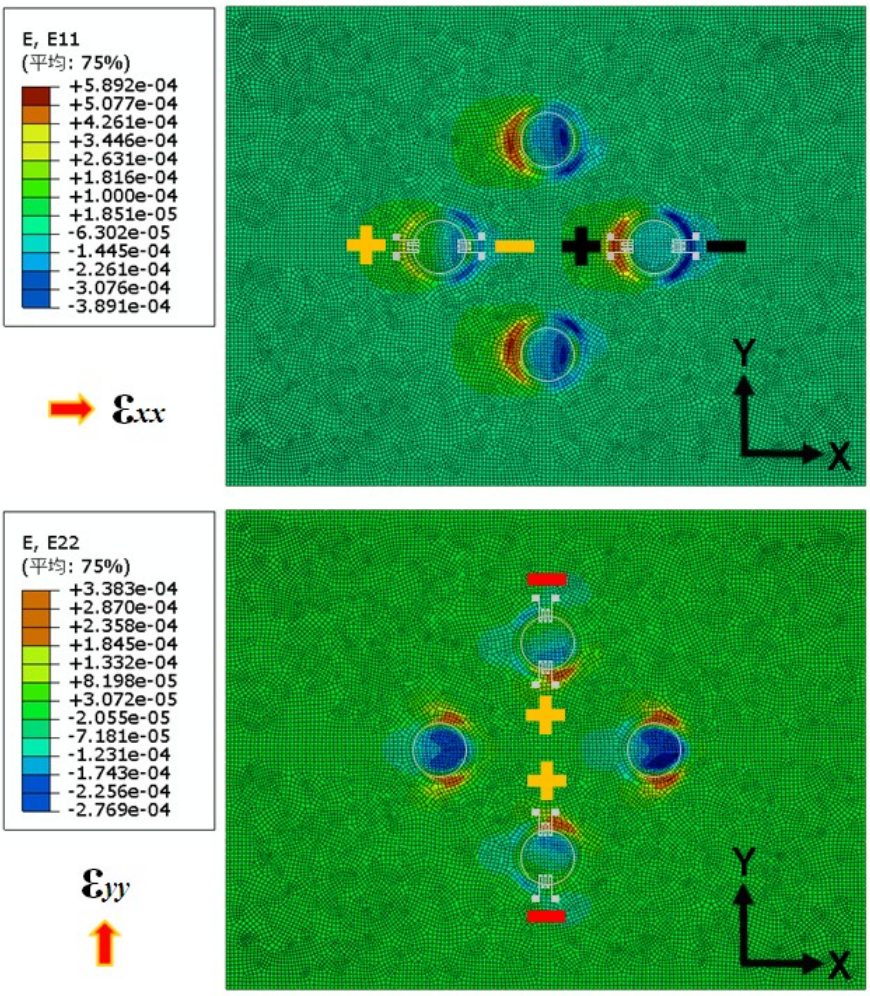

Figure 3.2.10 (ε_{xx}) and (ε_{yy}) strain distributions due to application of superposition of normal and tangential load.

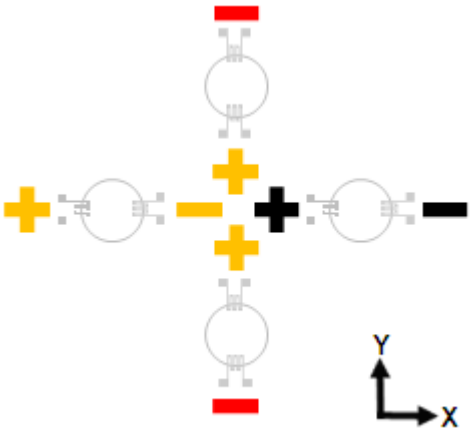

Figure 3.2.11 Schematic representation of the symbolized distributions due to application of superposition of normal and tangential load.

Tangential loading F_{xy}

In the case of applied F_{xy} loading (applying uniform 1 N along the 45° parallel to the +x-axis), the schematic modeling is shown in Figure 3.2.12.

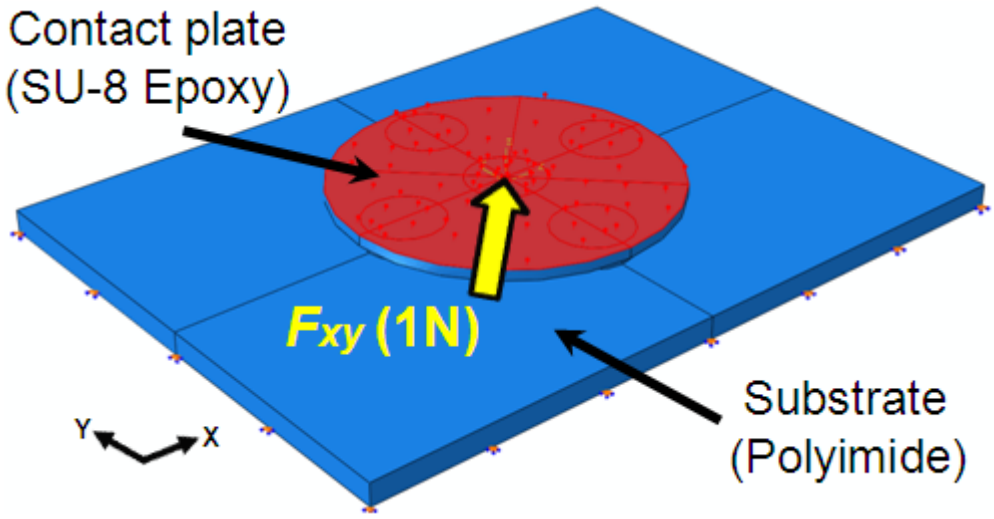

Figure 3.2.12 Schematic representation of the loading simulations for 1-N diagonal-direction (45°) tangential loading.

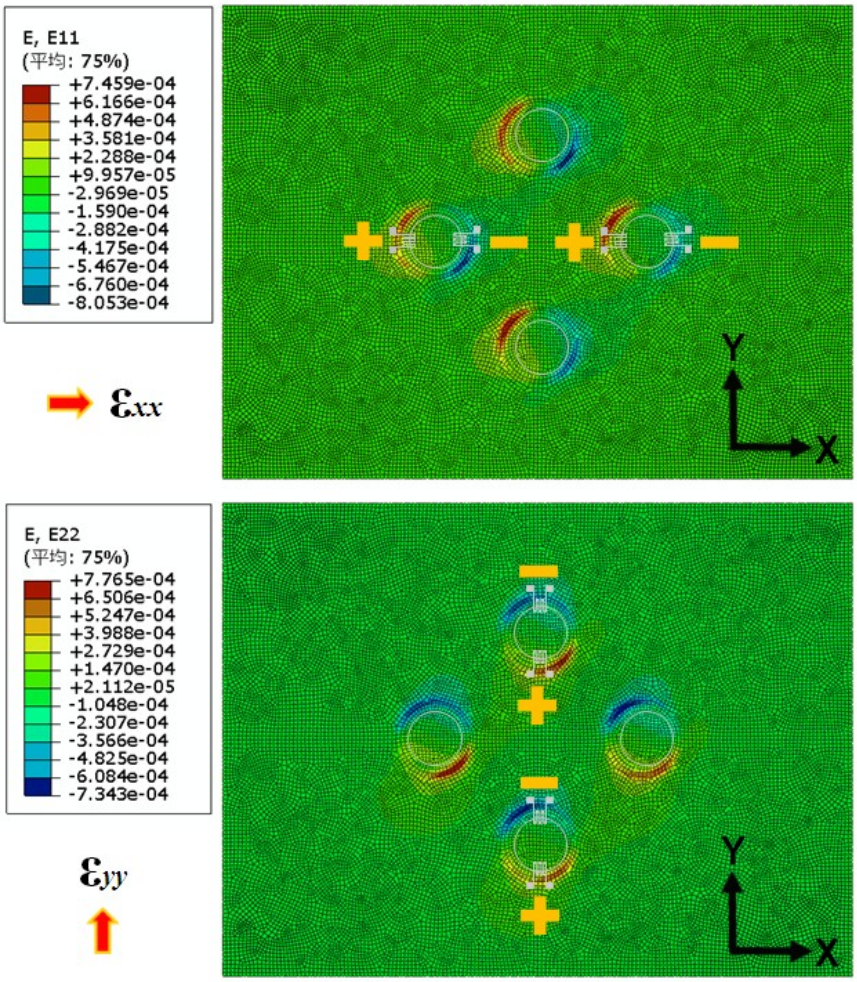

Figure 3.2.13 (ε_{xx}) and (ε_{yy}) strain distributions due to application of 1-N tangential loading.

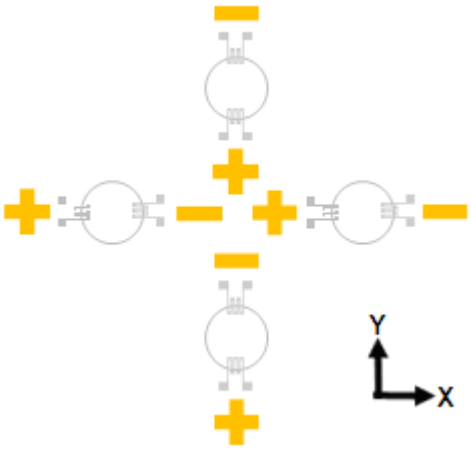

Figure 3.2.14 Schematic representation of the symbolized distributions due to application of 1-N tangential loading.

Resultant loading F_{z+xy}

In the case of applied F_{z+xy} loading (applying uniform 1 N along the 45° parallel to the +x-axis and –z-direction), the schematic modeling is shown in Figure 3.2.15.

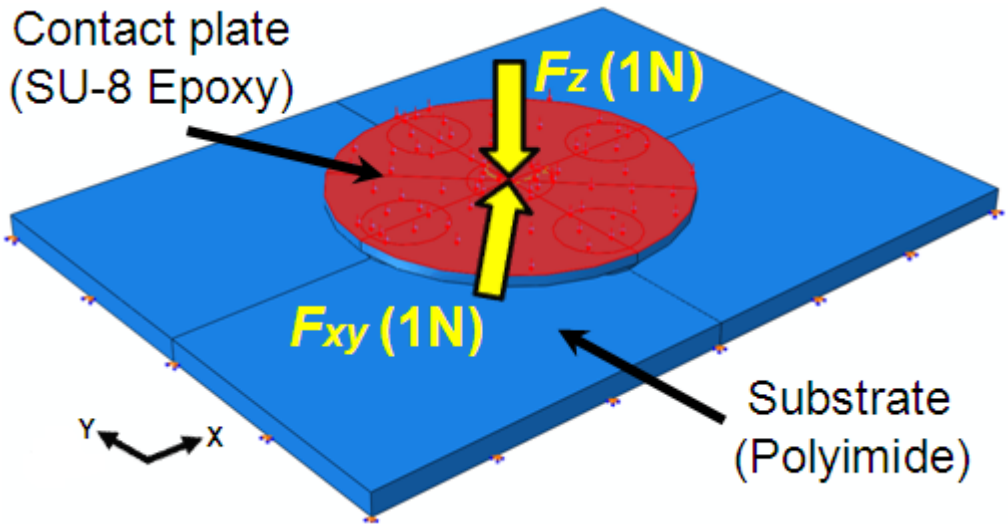

Figure 3.2.15 Schematic representation of the loading simulations for superposition of normal and tangential load.

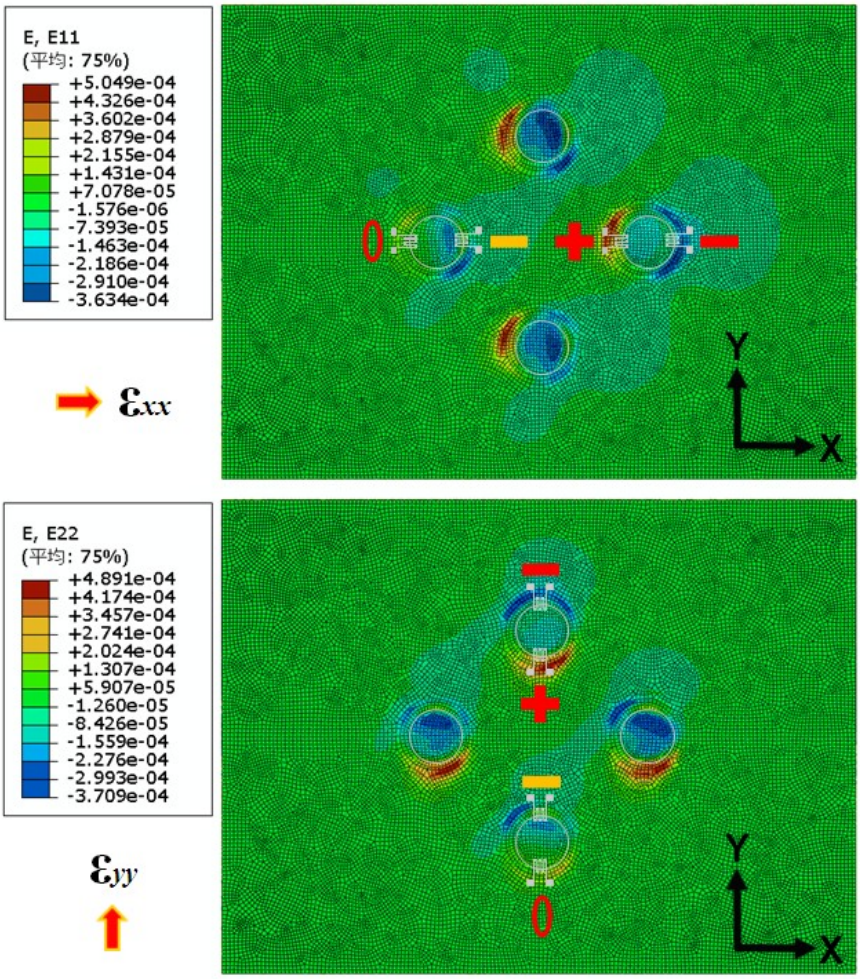

Figure 3.2.16 (ε_{xx}) and (ε_{yy}) strain distributions due to application of superposition of normal and tangential load.

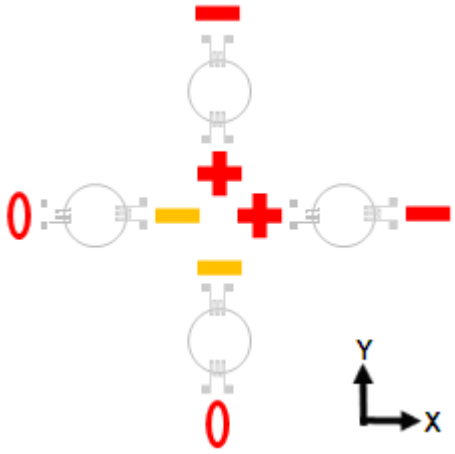

Figure 3.2.17 Schematic representation of the symbolized distributions due to application of superposition of normal and tangential load.

The combined results of Figures 3.2.2 to 3.2.17 and Table 3.1.1 are shown in Figures 3.2.18(A) to (C).

The FEA simulation result for superposition of normal force and tangential force at 0° parallel to the +*x*-axis is shown in Figure 3.2.18 (A). When a normal load is uniformly applied to the top surface of the contact plate, the simulation result shows a symmetrical feature under the support column. Four strain gauges inside the contact plate undergo tensile state (see Figure 3.2.18 (F_z)). However, the state of the four strain gauges arranged outside the contact plate becomes compressive.

Meanwhile, in the case that a tangential load is uniformly applied to the contact plate, the simulation result shows two different results. The state of the strain gauges arranged in the forward direction of the columns parallel to the loading direction becomes compressive, while the state of the strain gauges arranged in the backward direction of the columns parallel to the loading direction becomes tensile. Notice that the four strain gauges at a right angle to the loading direction do not change state (see Figure 3.2.18 (F_{xy})). Therefore, superposition of normal force and tangential force at 0° parallel to the +*x*-axis shows the sum of the strain change at each strain gauge. However, tangential variation is more dominant compared to normal variation in the case of the resultant force, if the magnitudes of applied normal and tangential forces are the same. Accordingly, when the positive sign of a tangential force meets the negative sign of a normal force, it does not give zero (see Figure 3.2.18 (F_{z+xy})).

In the figure, red indicates the strain change values under applied loading of 1 N. Black indicates duplicated red. Yellow indicates counterbalanced value when (+) and (-) red meet each other. Similarly, results for superposition of normal force and tangential force at 45° and 90° parallel to the +*x*-axis are shown in Figures 3.2.18 (B) and 3.2.18 (C), respectively.

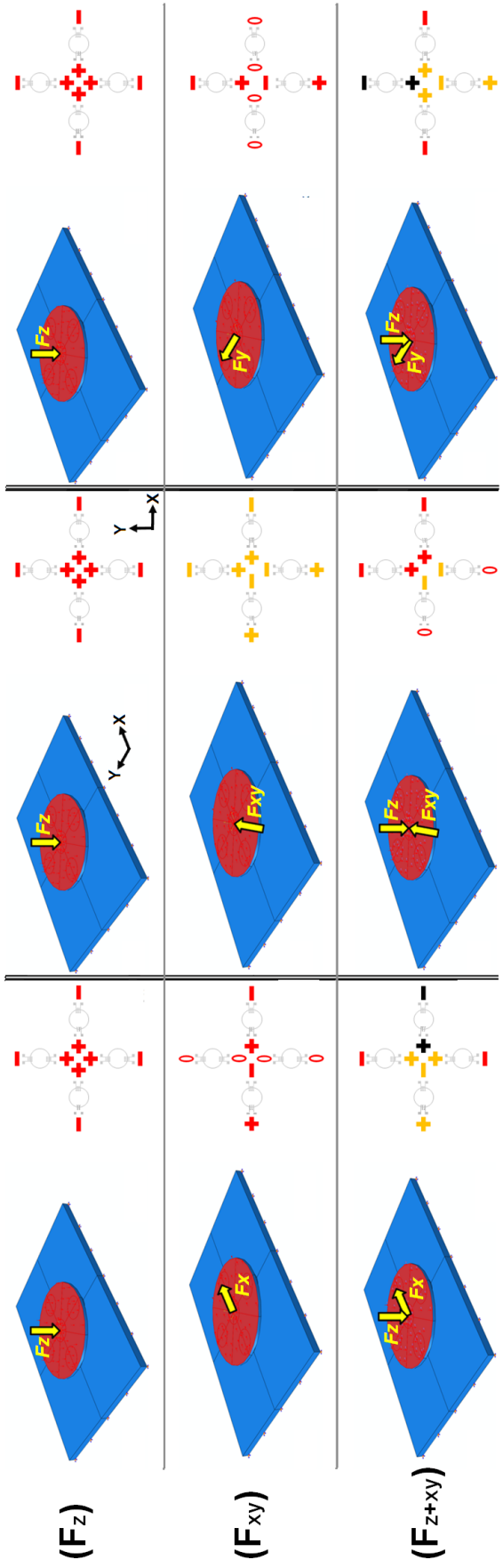

Figure 3.2.18 (A) Strain distribution under applied normal load, +*x*-direction (0°) tangential load, and superposition of normal and tangential load; (B) Strain distribution under applied normal load and diagonal-direction (45°) tangential load and superposition of normal and tangential load; (C) Strain distribution under applied normal load and +*y*-direction (90°) tangential load and superposition of normal and tangential load.

3.2.2 Detection of arbitrary tangential force direction

A schematic representation of the design of loading simulations for each directional tangential loading is shown in Figure 3.2.19.

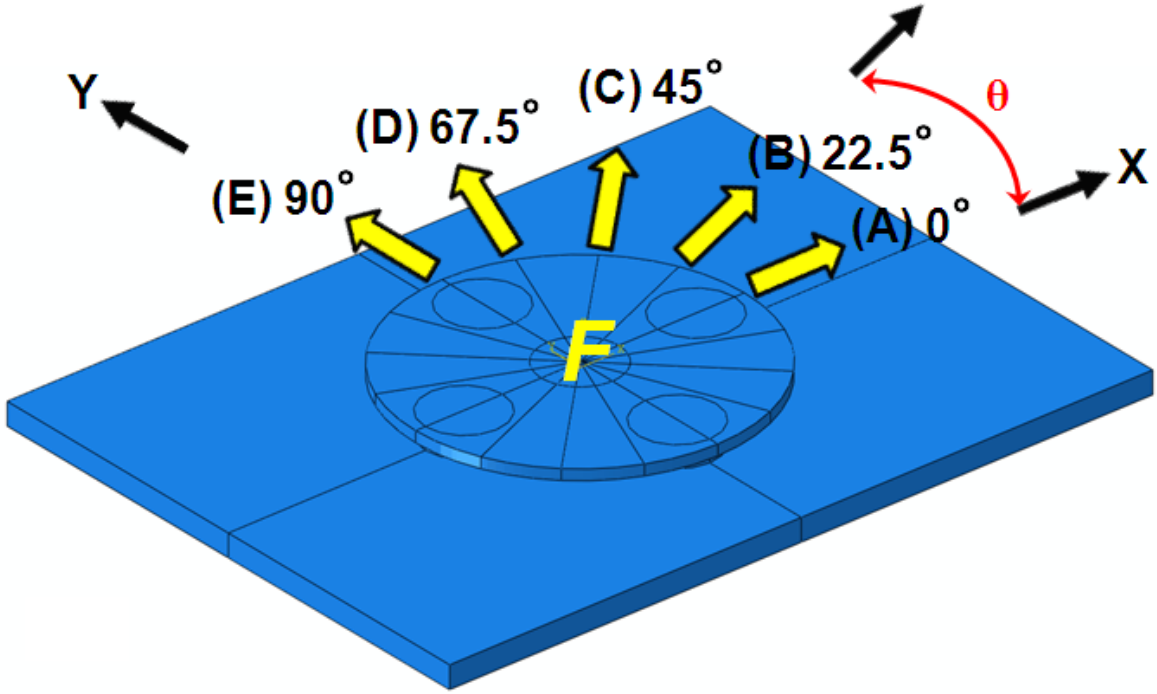

Figure 3.2.19 Schematic representation of the design of loading simulations for each directional tangential loading.

Maximum strain change under 1-N directional tangential loading is plotted against principal strain variation in the $+x$ direction (ε_{xx}) in Figure 3.2.20(A), and principal strain variation in the $+y$ direction (ε_{yy}) is plotted in Figure 3.2.20(B). These data are measured every 22.5° from 0° to 360° parallel to the $+x$-axis. These asymmetric sinusoidal results caused by the configuration of the support pillar could be expandable in two-dimensional mapping. We are able to produce a two-dimensional strain distribution map to directional loading divided into five cases.

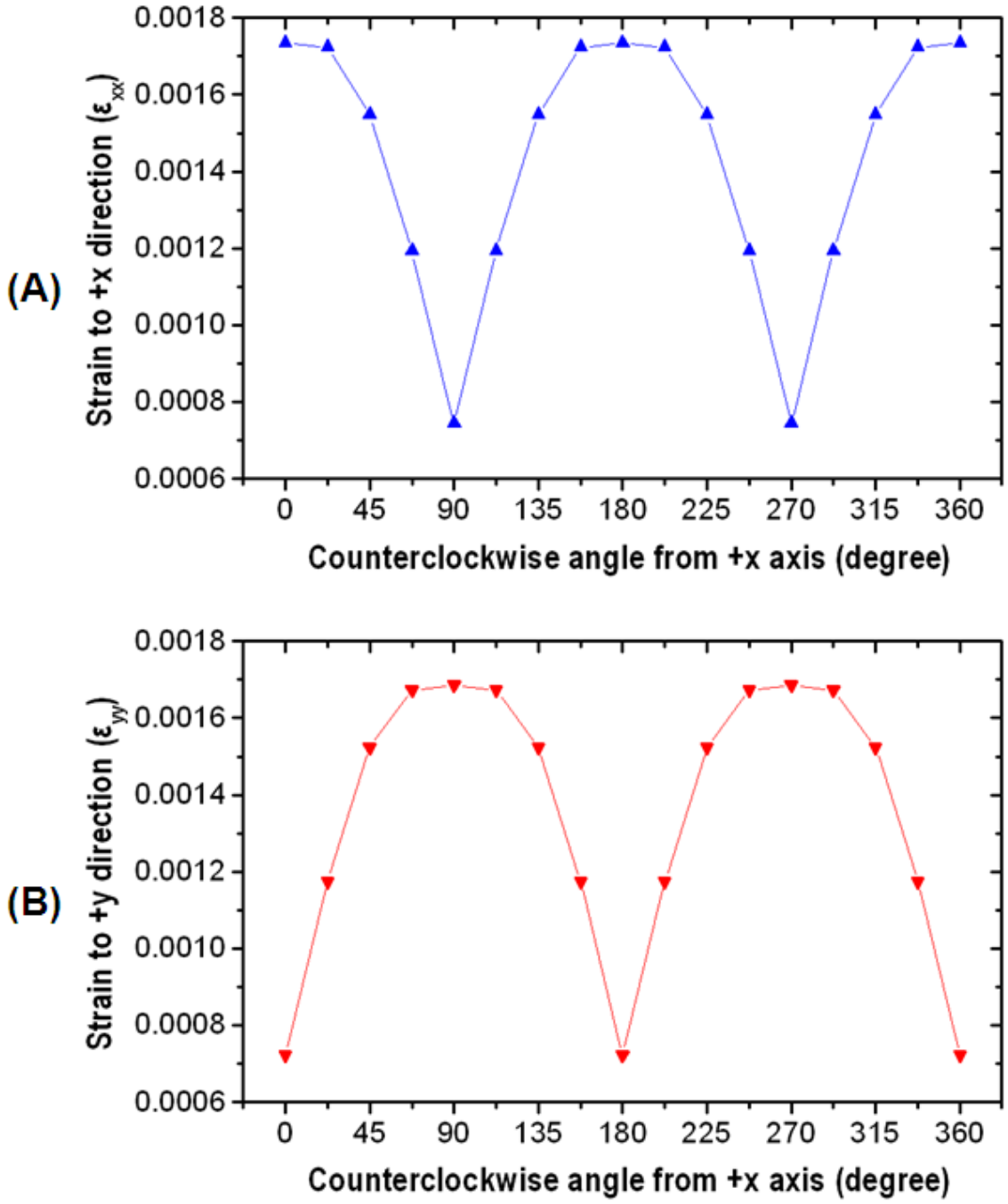

Figure 3.2.20 (A) Maximum strain change under 1-N directional tangential loading against principal strain variation in the $+x$ direction (ε_{xx}) and (B) principal strain variation in the $+y$ direction (ε_{yy}). These data are measured every 22.5° from 0° to 360° parallel to the $+x$-axis.

3.3 Force detection by simulations

Superposition principle of vector force

Force applied to a monolithic sensor is a vector combination of normal and tangential forces. The mixed components of normal and tangential forces must be decoupled. However, it is a problem that the decoupling cannot be done directly. To solve this problem, output resistance can be related to applied loading. A distribution map of the strain gauges (which depends on the configuration of the gauges) can then be drawn (see Figure 3.3.1). It is therefore possible to approximately calculate the direction and magnitude of the applied loading through the reconstruction of the contributing directional forces (which are combined by using calibration data).

FEA loading simulations

The results of FEA loading simulations, namely, displacement contour (U) and strain distribution due to application of 1-N directional tangential loading [(ε_{xx}) and (ε_{yy})] at 0°, 22.5°, 45°, 67.5°, and 90° against the +x-axis, are plotted in Figures 3.3.1 (A) to (E), respectively. A displacement contour (U) and strain distribution due to application of 1-N normal loading [(ε_{xx}) and (ε_{yy})] are plotted in Figure 3.3.1 (F). A displacement contour (U) and strain distribution due to application of normal and tangential loading [(ε_{xx}) and (ε_{yy})] at 0° against the +x-axis are plotted in Figure 3.3.1 (G). Notice the configuration of the strain gauges lies along the principal strain directions ((ε_{xx}), (ε_{yy})). To find the origin of the applied force, we are able to use two-dimensional mapping data obtained from the directional force contribution of the strain distribution. Direction and magnitude of the applied loading can therefore be back-calculated by reconstructing an image of the total-axial-force components.

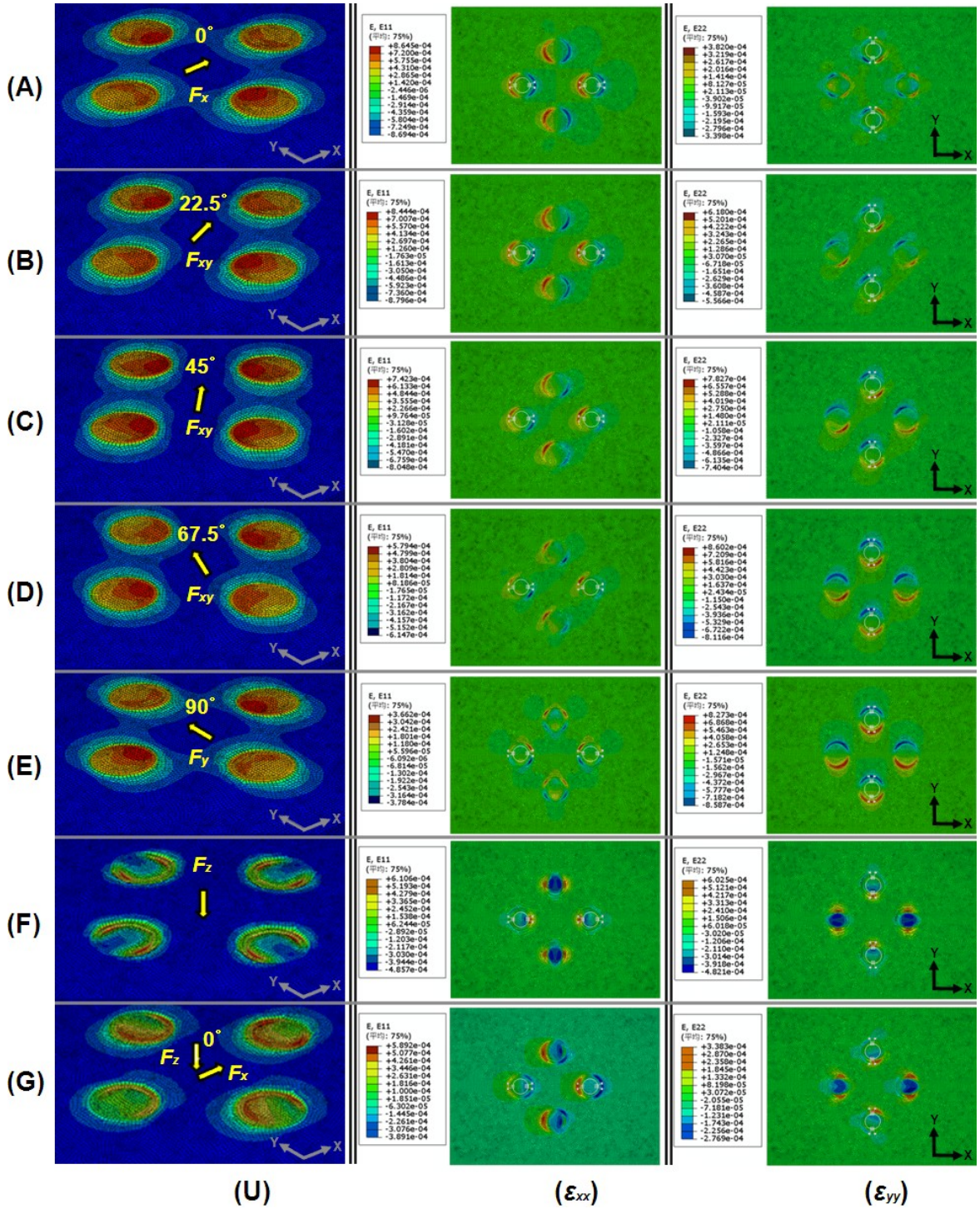

Figure 3.3.1 FEA results of loading simulations. Displacement contour (U) and (ε_{xx}), (ε_{yy}) strain distribution due to application of 1-N directional tangential loading at (A) 0°, (B) 22.5°, (C) 45°, (D) 67.5°, and (E) 90° against the +x-axis, respectively; (F) due to application of 1-N normal loading; (G) Resultant force of normal and tangential loading at 0° against the +x-axis.

Reconstructing an image of the total-axial-force components

The signal combinations of all possible arrangements of the strain gauges and the predicted direction are listed in Table 3.3.1. The directions of applied tangential force can be predicted by comparing the configuration of settled standard feature using Figures 3.2.18 due to Table 3.1.1 and Figures 3.2.20 and Figures 3.3.1. Prediction resolution is shown as three levels of color (i.e., black, red, and yellow). Note that the prediction resolution can be increased by increasing the number of color levels.

Table 3.3.1. The signal combinations of all possible arrangements of the strain gauges and the predicted direction.

	Signals and decisions				
	R_1	R_3	R_5	R_7	Decision
1	+	+	+	+	F_{-z}
2	-	0	+	0	F_{+x}
3	+	0	-	0	F_{-x}
4	0	-	0	+	F_{+y}
5	0	+	0	-	F_{-y}
6	-	-	+	+	F_{+x+y}
7	+	-	-	+	F_{-x+y}
8	+	+	-	-	F_{-x-y}
9	-	+	+	-	F_{+x-y}
10	-	+	+	+	$F_{-z} + F_{+x}$
11	+	+	-	+	$F_{-z} + F_{-x}$
12	+	-	+	+	$F_{-z} + F_{+y}$
13	+	+	+	-	$F_{-z} + F_{-y}$
14	-	-	+	+	$F_{-z} + F_{+x+y}$
15	+	-	-	+	$F_{-z} + F_{-x+y}$
16	+	+	-	-	$F_{-z} + F_{-x-y}$
17	-	+	+	-	$F_{-z} + F_{+x-y}$

Chapter 4

Polymer-micromachining

4.1 State of the art for polymer-micromachining

For a wide variety of applications, sensors have to be mounted on non-planar surfaces or even on flexible objects (see Figure 4.1.1) [9, 52]. To create a tactile sensor with both small size and high flexibility, polymer micromachining (which makes it possible to integrate MEMS devices on a flexible polymer substrate) has been introduced. Polymer-based triaxial tactile sensors could solve troubles of the current issues because polymer materials are flexible, and have good thermal, electrical, mechanical, and chemical stabilities. That is the reason why it moved to polymer-micromachining from silicon-micromachining.

Meanwhile, although polymer micromachining technology has been developed for a variety of polymer materials, a fabrication technique that can control fabrication-conditions well on reproduction needs to be developed. Polymer-micromachining has disadvantages compared to silicon-micromachining in fabrication, such as limitation of the uniform coating, alignment difficulty in the photolithographic process because of thermal deformation of polymer substrate, and restrictions due to using a thick sacrificial layer for the three-dimensional structure. Furthermore, a dry/wet etching technique has also been used for fabricating a polymer-micromachined sensing membrane for tactile sensors [40-45].

However, this etching technique weakens the robustness of polymer material through physical/chemical damages. Therefore, as the solution for the issues mentioned above, we propose a thermo-compatible layer-by-layer fabrication method in a surface polymer-micromachining without wet/dry etching and fabrication technique of three-dimensional structure by using thick sacrificial layer for the full polymer-based sensing body. It includes a deposition accumulation process by a layered deposition process at low-temperature. It is very efficient for economical fabrication considering minimum process step.

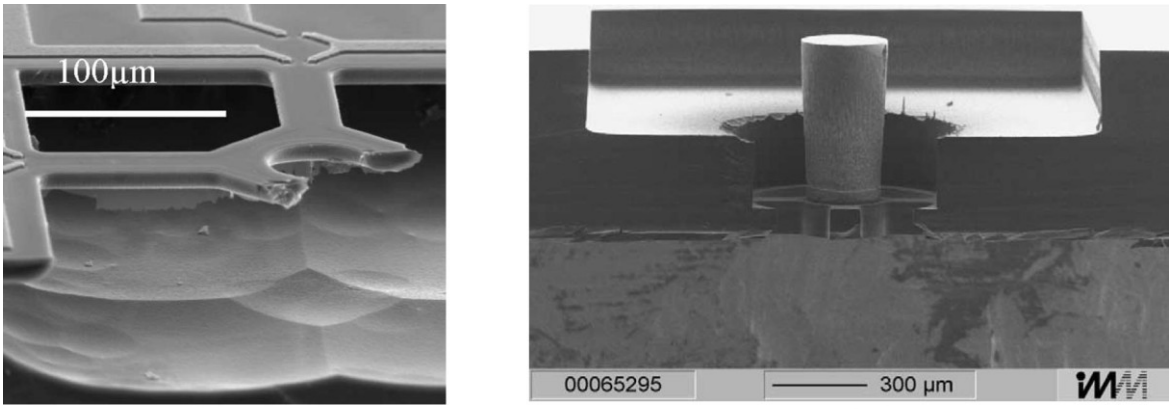

Figure 4.1.1 Silicon-based sensors have brittleness, (A) [60] and (B) [25].

4.2 Thick sacrificial layer technique

4.2.1 Three-dimensional structure using photolithography

Polymer micromachining technology has been developed by a variety of polymer materials. According to the demand for three-dimensional structure patterning, some methodologies of micromachining technology using polymer materials have been proposed. Most of methods are belonged in category of stereolithography technique as a photopolymerisation [61-62]. However, it is hard to apply photo-definable process to fabrication which has process-compatibility in a surface polymer-micromachining. Accordingly, we consider using sacrificial layer for a process-compatibility, then, the sacrificial layer material was chosen carefully.

Some kinds of sacrificial layer techniques for three-dimensional structure patterning have been developed having process-compatibility in the SU-8 polymer-micromachining fields with different materials [63-66]. One is the polydimethylglutarimide (PMGI) as a sacrificial material [63] or polycarbonates using air degassing method [64]. However, the achieved maximum thickness is only 20-μm or less [63-64].

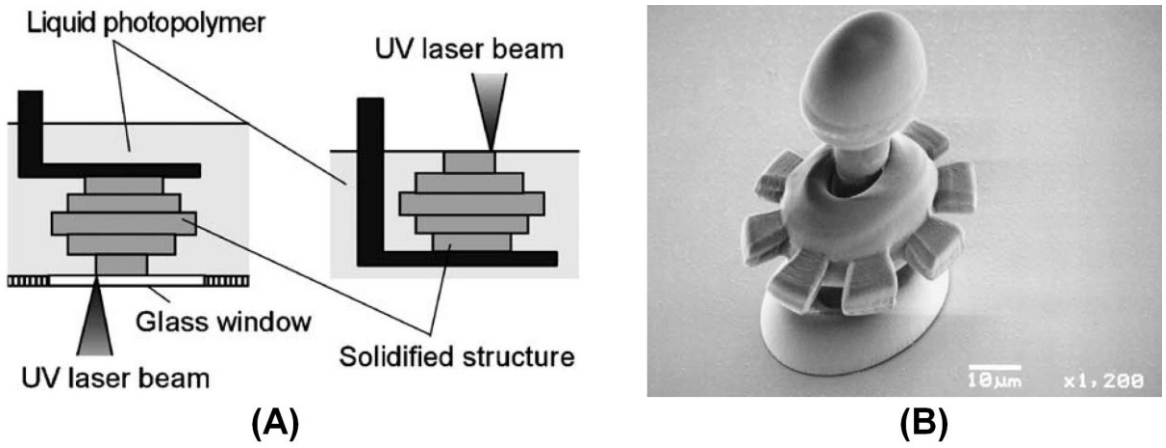

Figure 4.2.1 (A) Schematic diagram of the stereolithography technique and (B) three-dimensional structure used by stereolithography [62].

Another way is using uncrosslinked SU-8 as a sacrificial multilayer itself with a UV-blocking [65]. Because thickness of the exposed SU-8 layer has to be precisely dosage-controlled UV exposure, this method has many critical process steps [65]. The other approach is using thick photoresist material such as AZ 4562 [66]. Although thick photoresist has two problems (*outgassing effect* and *scission effect*), it was possible to achieve up to 100-μm thickness sacrificial layer [66]. From previous research study (see Table 4.2.1), we propose a new surface polymer-micromachining technique for a three-dimensional monolithic sensor structure using unexposed photoresist as a thick sacrificial layer. A schematic diagram of the proposed fabrication technique is shown in Figure 4.2.2.

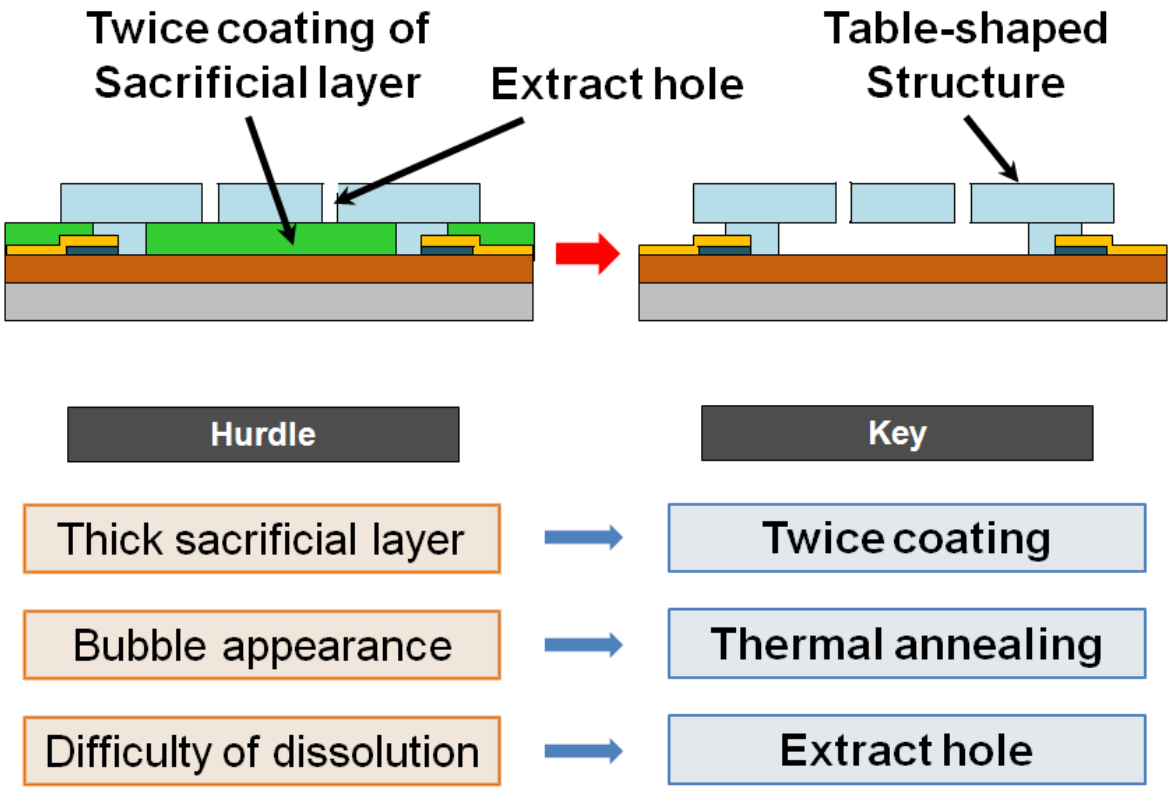

Figure 4.2.2 Schematic diagram of the proposed fabrication technique.

Table 4.2.1 Comparisons on selected three-dimensional structure fabrication using photolithographic sacrificial layer technique in the SU-8 polymer-micromachining fields.

	Fabrication technique	**Sacrificial layer material**	**Maximum sacrificial layer thickness**	**Drawbacks**
Foulds et al. [63]	Lift-off and release	Polydimethylglutarimide (PMGI)	< 4 μm	Low sacrificial layer thickness
Metz et al. [64]	Heat-depolymerizable air degassing	Polycarbonates	< 20 μm	Low sacrificial layer thickness
Foulds et al. [65]	UV-blocking (uncrosslinked SU-8)	Uncrosslinked SU-8	< 20 μm	Low sacrificial layer thickness
Bao et al. [66]	thick photoresist (directly deposited)	AZ 4562	~ 100 μm	Outgassing effect and scission effect
Target of this study	thick photoresist (twice coating)	PMER P-HA 1300PM	~ 60 μm	-

4.2.2 Twice coating of thick photoresist

To make a table-shaped three-dimensional structure as a contact detector of the tactile sensor, a sacrificial layer is fabricated using a photodefinable lithography process with a novel thick photoresist material, positive-toned PMER (TOK, PMER P-HA 1300PM). There are two reasons for PMER photoresist was selected as the sacrificial layer in this study. First, PMER can be fabricated by standard photolithography equipment with process-compatibility. Additionally, PMER is able to have considerable thickness up to 60-μm by repeating of the spin coating, that is desired specific needs of a sacrificial layer.

The parameters for the fabrication were investigated in advance. Although maximum thickness of PMER is possible up to 40-μm at once, that is not recommended over 30-μm at once because of its reproducibility with uniform coating. To achieve desired height of up to 60-μm-thick, we conducted photolithographic process through twice coating of PMER. Trice coating once a 20-μm is also not recommended, because of difficulty of exposure by change of physical property caused fine difference of refraction index at interface of each layer. In addition, trice coating may causes segregation between deposited layers. Figure 4.2.3 shows deposited PMER photoresist and Figure 4.2.4 shows measured height of sacrificial layer by surface profiler (Mitutoyo Co., SV-3000 CNC), around 62-μm-thick is coincide with desired height.

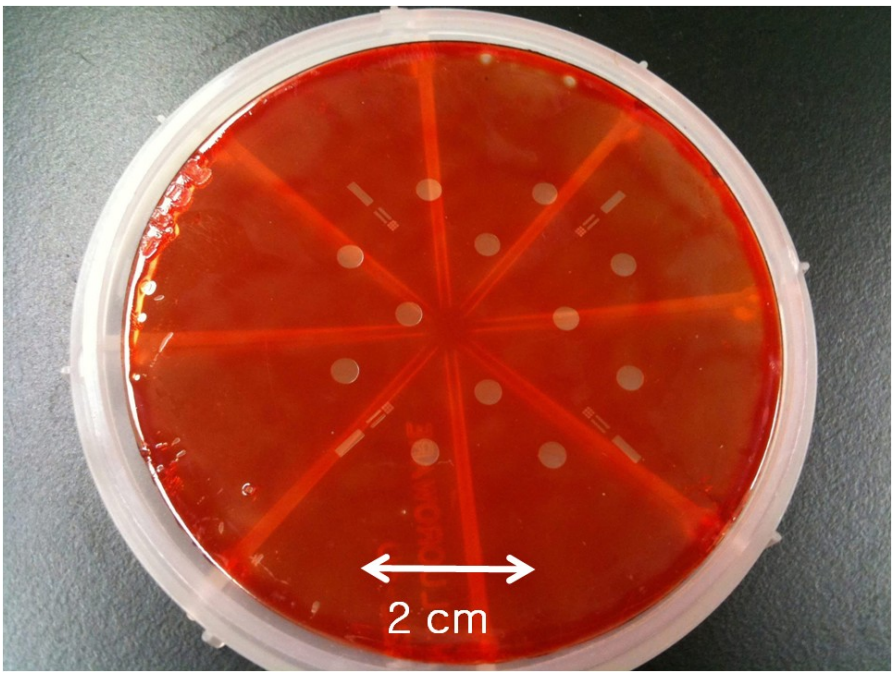

Figure 4.2.3 Deposited PEMR resist as a sacrificial layer which has 60-μm-thick achieved by twice coating.

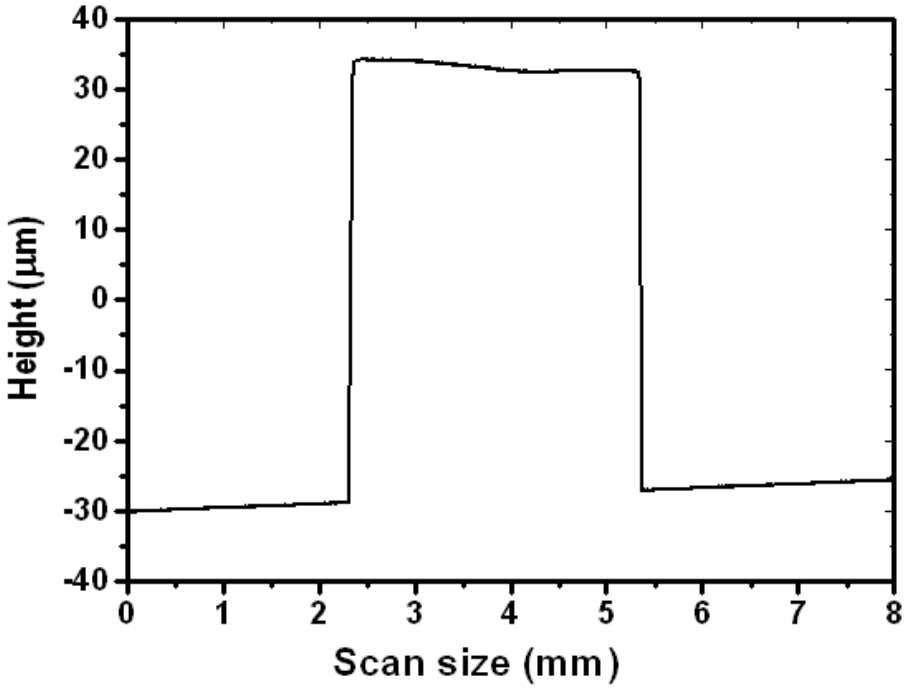

Figure 4.2.4 Measured thickness profile of the sacrificial layer which has 60-μm-thick achieved by twice coating.

4.2.3 Thermal annealing and extract-hole technique

Outgassing and scission effects

There exist two problems in twice coating of PMER like using by photoresist AZ 4562 [66]. One is bubble appearance at interface between 1st and 2nd deposited layers (see Figure 4.2.5). It is well-known the *outgassing effect* [66-68]. The *outgassing effect* is caused by seized vapor from chemical reaction of 1st deposited layer under thermal treatment of 2nd deposited layer. Moreover, twice coating of polymer materials can make chance to insert air into tiny chasm of interface made by different hardening rate which caused process time interval between 1st and 2nd deposition.

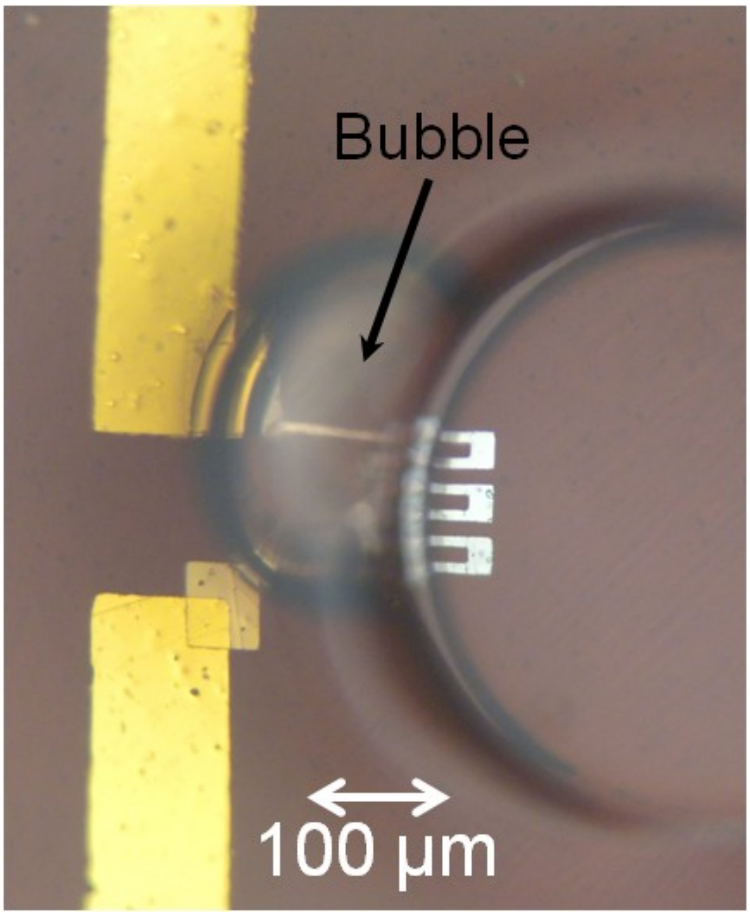

Figure 4.2.5 Bubble appearance at interface between 1st and 2nd deposited sacrificial layers.

The other problem is difficulty of dissolution of the sacrificial layer. Dissolution process of exposed photo-definable material depends on a variety of physical and chemical conditions. For example, shape of the structure, covered roof area, wall height, surface roughness of surroundings, solubility of sacrificial material, viscosity of dissolved polymer and so on. Meanwhile, one of the contributions in the difficulty of dissolution is caused by called the *scission effect* [66-68]. The reason of the *scission effect* is very simple. The molecular chains of a photoresist are easily broken by the energy absorption through UV exposure [66-68]. While the upper SU-8 layer was exposed, the underlying photoresist sacrificial layer may lightly expose because SU-8 layer is transparent. The exposure dose was carefully controlled for the minimum transparent expose to the surface of the sacrificial layer [66-68]. However, sacrificial layer and SU-8 layer are very thick (60-μm). Thus sacrificial layer surface has a little exposure, since most of the sacrificial layer would not be exposed. Therefore, most considerable reason of dissolution difficulty in this study is an area of upper plate and configuration of the structure including upper plate and pillar.

Thermal annealing of sacrificial layer

First, in order to overcome bubble appearance, we performed thermal annealing which made by slow downing of *post coating delay time* after soft bake during temperature lowering. This treatment very effectively eliminates bubble appearance, because it may to contribute to thermal uniformity of the PMER photoresist caused by reducing the residual stress. We conducted temperature lowering from soft bake temperature (110 °C) to room temperature through 4-steps per 20 minutes (see Figure 4.2.6).

Extract-hole for removal of sacrificial layer

Meanwhile, the sacrificial layer is removed by PMER stripper. When dissolving time gets longer and longer, SU-8 epoxy and polyimide substrate are attacked chemically, because a component of the PMER stripper is PGMEA (Propylene Glycol Methyl Ether Acetate), it is also a component of

the developer of SU-8 epoxy.

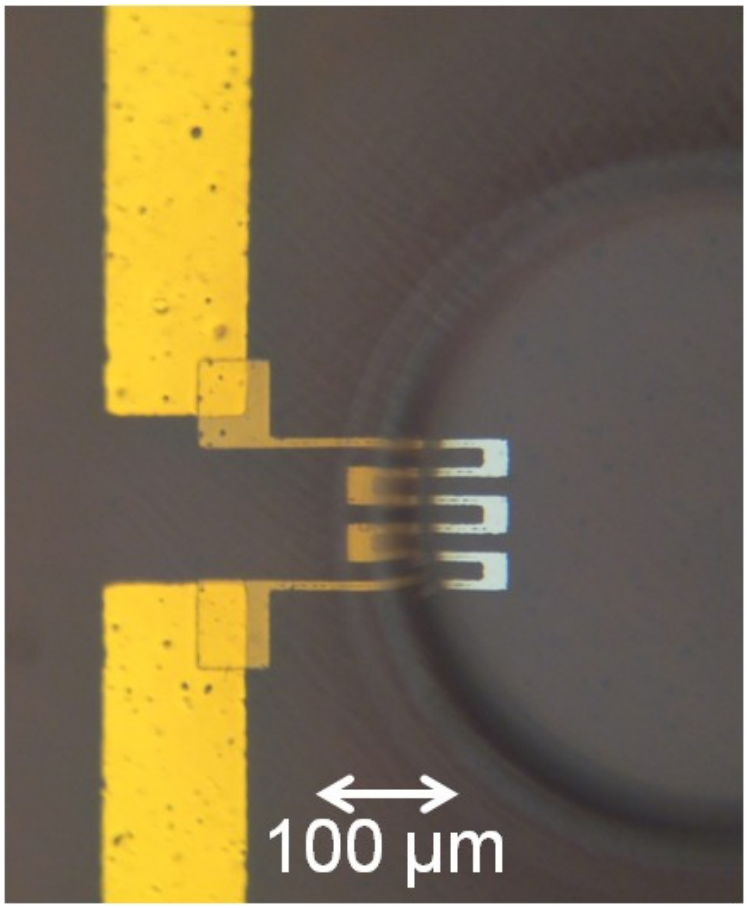

Figure 4.2.6 Improved feature of bubble problem after 4-steps thermal annealing.

Therefore, to enhance the dissolution rate of the sacrificial layer under the large covered plate, we propose extract-holes on the covered epoxy surface. Designed contact plate has five-holes with 110-μm-radii which are configured symmetrically to avoid shadowed area by four pillars (see Figure 4.2.7). It was possible to solve the problem, since sacrificial layer was past through contraction of the dissolving time. Figure 4.2.8(A) shows microscopic view of cross-section of table-shaped structure and scanning electron microscope (SEM: S-3000NA, HITACHI Ltd.) feature (see Figure 4.2.8(B)) which was pre-treated by 50-nm-thick Au coating (Quick coater: SC-701AT, Sanyu electron Ltd.). We are able to see the success of the three-dimensional structure that realized by dissolution of the sacrificial layer.

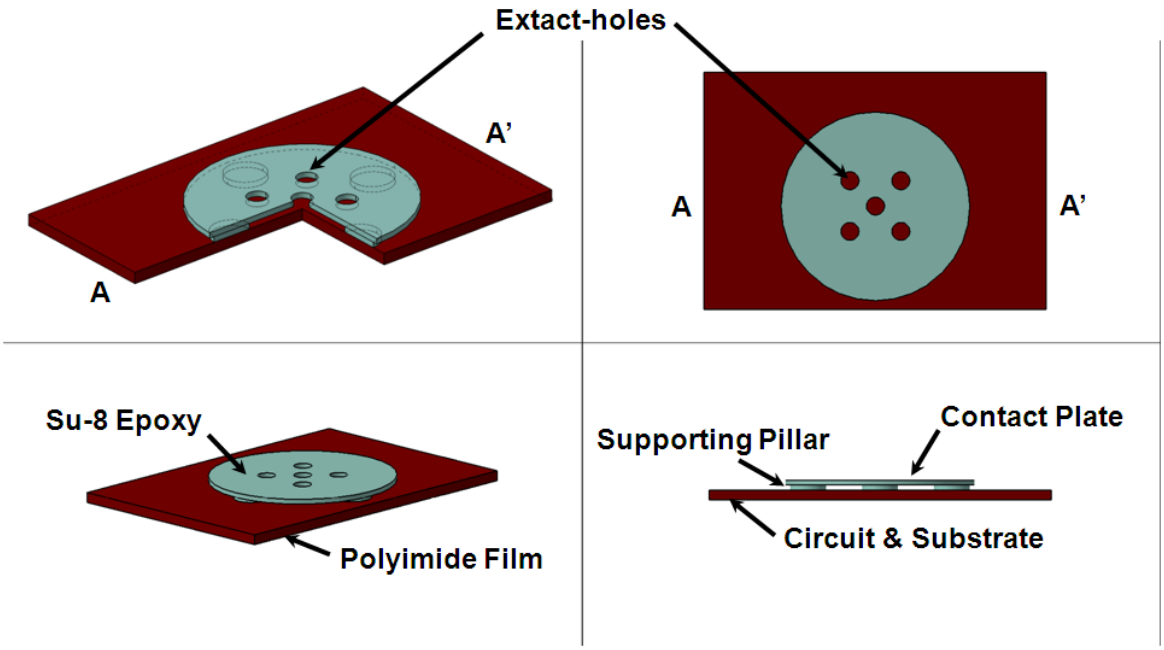

Figure 4.2.7 Configuration of extract-holes on the epoxy surface.

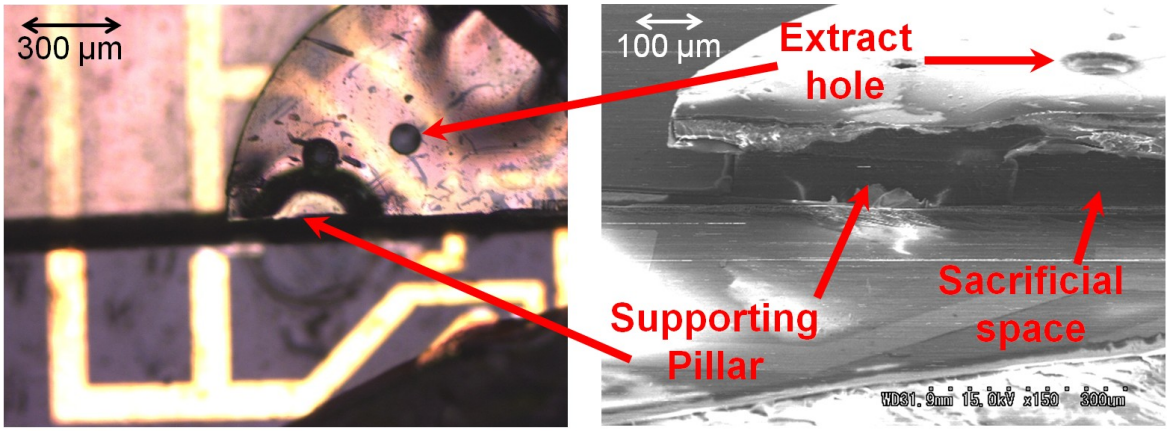

Figure 4.2.8 Microscope (A) and SEM (B) feature for the cross-sectional view of table-shaped structure (A-A' of Figure 4.2.7). It shows clearly the three-dimensional structure achieved by the sacrificial layer and symmetrically configured five extract-holes with 110-μm-radii on the contact plate.

4.3 Thermo-compatible fabrication

When several polymer materials are used in the same polymer-micromachining process, the design of fabrication process step needs to tune without interference among them. Comparing to silicon-micromachining, polymer-micromachining has disadvantage of alignment difficulty in the photolithographic process because of thermal contraction. It is very important point to repeat photolithographic fabrication process. To accomplish process-compatibility in the polymer micromachining by using photo-definable polymer materials which have different coefficient of thermal expansion (CTE), all processes were designed considering chemical stability such as safe development without extra dissolving caused by chemical reaction of interference. Moreover it includes a layered deposition process at low-temperature below 110°C as a threshold temperature of thermal deformation in this study (see Table 1).

These strategies were possible to make sensor minimizing thermal/chemical damages with robust structure through the simplification of process step. It is very efficient for economical fabrication for consideration of minimum-process-step. The advantages of the approach to fabricate are obviously, because this technique can overcome the restrictions such as damage of the polymer material by the etching technique.

Table 4.3.1 Thermal property of polymer materials [59].

Fabrication process turn	Polymer Material	Coeff. of Thermal Expansion (ppm/°C)	Maximum Process Temperature (°C)
1	Kapton® HN polyimide film	20	-
2	OFPR-800LB/100Cp	-	90
3	PMER P-HA 1300 PM	Approx. 38	110
4	SU-8 3050	52	95
5	Parylene C	35	-

The designed sensor was fabricated by using the surface micromachining technique based on a photo-definable polymer material, SU-8 series epoxy, which has a negative-toned and solvent-developable. Table 4.3.1 shows a thermal property of used polymer materials (polyimide film - Kapton® HN (DuPont™), photo resist - OFPR-800LB/100Cp (TOK), photo resist - PMER P-HA1300PM (TOK), photodefinable epoxy - SU-8 3050 (Microchem), passivation coating - Parylene C (SCS)) for the designed fabrication process in this study.

Chapter 5

Sensor fabrication

5.1 Fabrication summary

A tactile sensor was fabricated by the following process. Figure 5.1.1 shows a schematic diagram of the step of fabrication process.

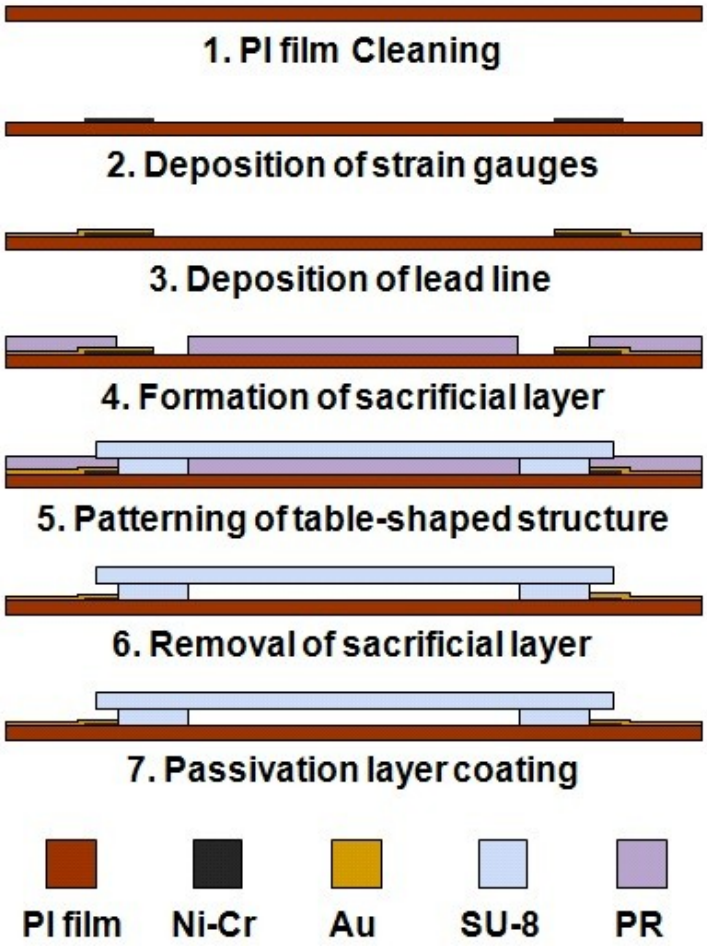

Figure 5.1.1 Flow chart of fabrication process.

All photolithographic fabrication processes were performed inside yellow-lighted clean room (Fig. 5.1.2).

Figure 5.1.2 Aspect view of yellow-lighted clean room.

5.2 Fabrication

5.2.1 Preparation of substrate

Pre-treatment of polyimide film

A 64-mm-diameter circle is cut from a sheet of 125-μm-thick DuPont™ Kapton® HN polyimide film for use as a substrate of the sensor-body and cleaned in a standard acetone-methanol soak and D.I. rinse (Fig. 5.2.1).

(1) Acetone soak : 1 min / 5 inch pyrex vessel
(2) Methanol soak : 1 min / 5 inch pyrex vessel
(3) D.I water rinse : 1 min / 5 inch pyrex vessel
(4) D.I water immersion : 10 min / 5 inch pyrex vessel

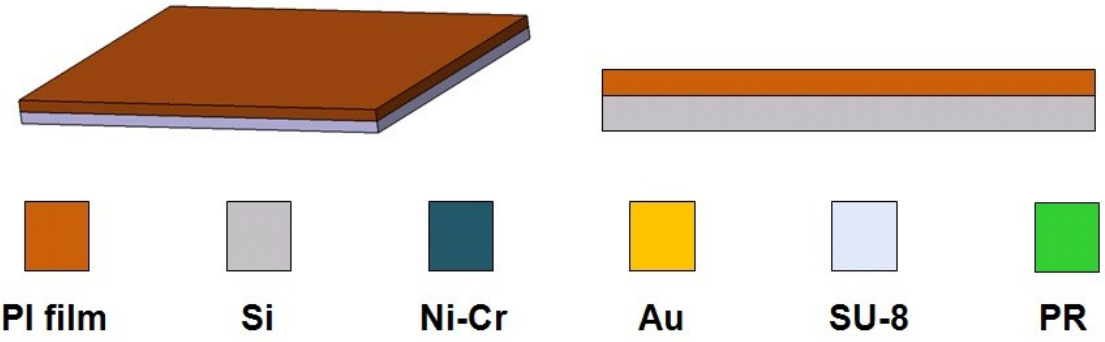

Figure 5.2.1 Cleaning and attachment of polyimide film to silicon carrier wafer.

Attachment of polyimide film to silicon carrier wafer

To avoid misalignment problems in the mask align processes, the carrier wafer must be prepared prior to device fabrication. It is need for thick carrier wafer against thermal contraction force of polymer film. The polyimide film

is carefully attached without air discharging to a 3 inch, 800-μm-thick silicon wafer via surface tension by wetting the substrate with a drop of de-ionized water, and then the polyimide film and silicon wafer is encapsulated with 10-mm-width 0.035-mm-thick Kapton polyimide tape (Fig. 5.2.2).

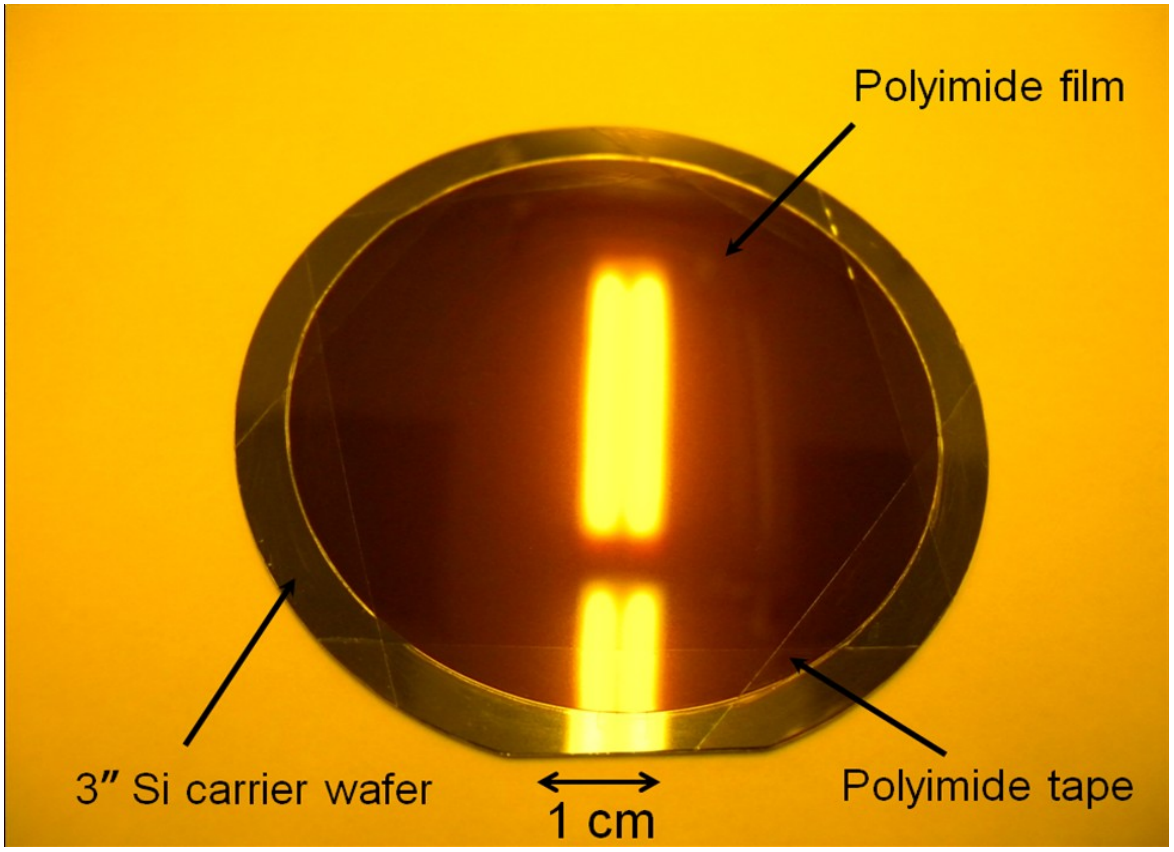

Figure 5.2.2 Attached and encapsulated polyimide film on silicon carrier wafer.

5.2.2 Patterning of metal strain gauges

Using a standard photolithographic technique with OFPR-800 photo resist (TOK, OFPR-800LB/100Cp), metal strain gauges were patterned by sputtering and lift-off techniques. A nickel-chrome-alloy material (Ni-Cr, 80:20) is used as the strain gauges. In detail, a 400 Å-thick of Ni-Cr layer was deposited on a 100 Å-thick chromium adhesion layer a 125-μm-thick polyimide substrate (Fig. 5.2.3).

Photolithography of the resistors

(1) spin coating : photo resist OFPR-800LB(100Cp) / spin coater
- step1 : 1500 rpm , 5 sec
- step2 : 3000 rpm, 20 sec

(2) soft bake : 90 °C, 30 min / hot plate
(3) align and exposure : i-line 178 mJ/cm^2 / PEM-800 mask aligner
- align mask : #1 resistor
- print gap : 0 μm
- alignment gap : 50 μm

(4) development : NMD-3 developer, 70 sec / 5 inch pyrex vessel
(5) D.I water rinse and dry : 1 min / 5 inch pyrex vessel

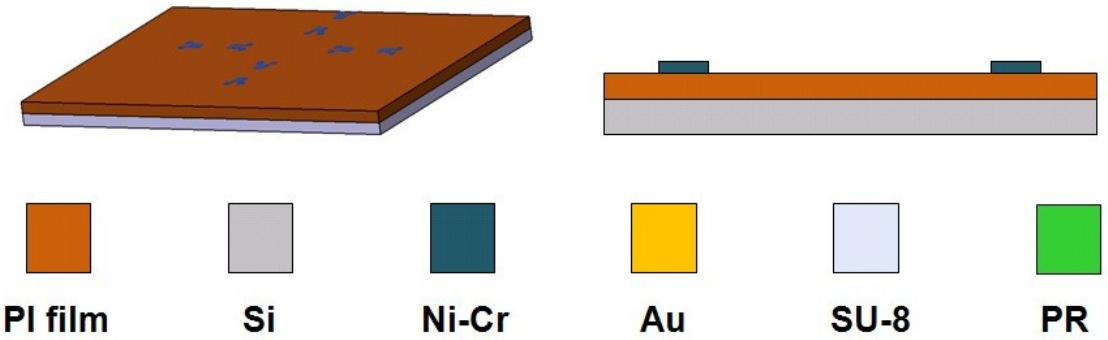

Figure 5.2.3 Ni/Cr resistors deposition.

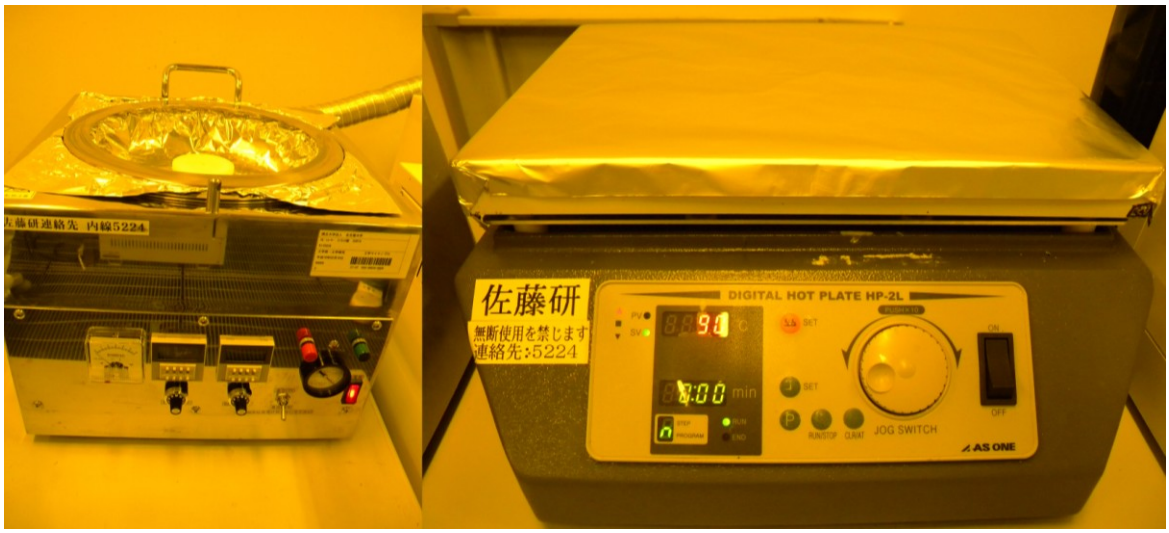

Figure 5.2.4 Spin coater and hot plate.

Figure 5.2.5 PEM-800 mask aligner and wet-bath for development.

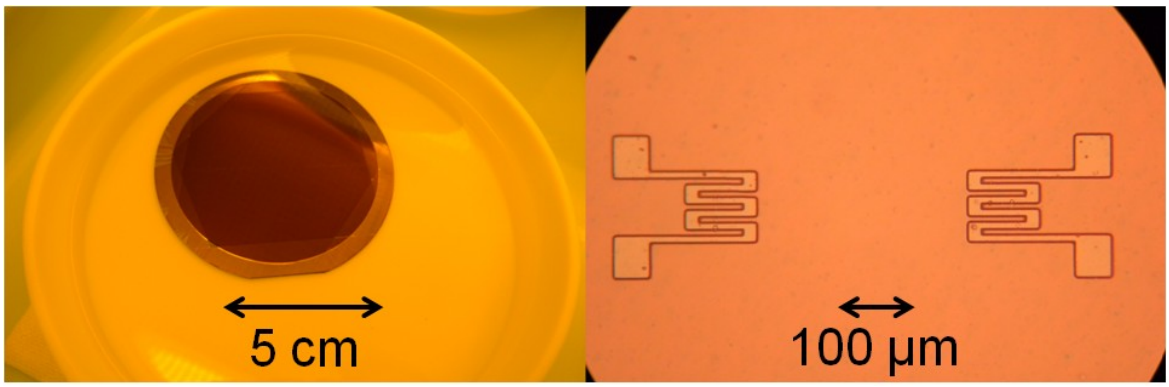

Figure 5.2.6 Development of PR and developed resistors.

Adhesion improvement technique by O_2 plasma treatment

After trial and error, to improve adhesion of the metal layers and polyimide film, the substrate is de-scummed by using 2 minutes of oxygen plasma at 100 W after photolithography and prior to sputtering [69-70]. Figure 5.2.7 shows plasma-asher and Figure 5.2.8 shows optical feature of effect of O_2 plasma treatment.

(1) descum : 2 min / O_2 plasma asher
- plasma power : 100 W
- chamber pressure : 30 Pa
- O_2 : 50 cc

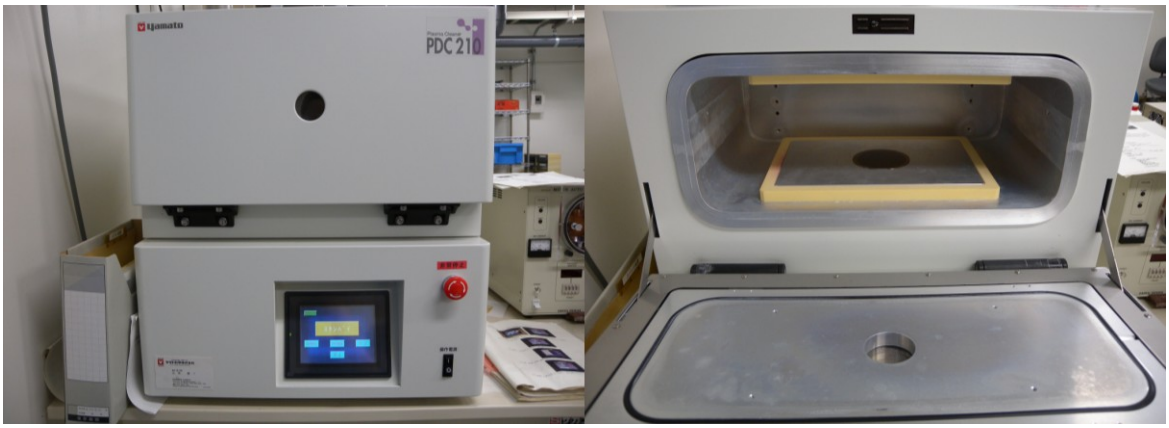

Figure 5.2.7 O_2 plasma asher and mounted wafer.

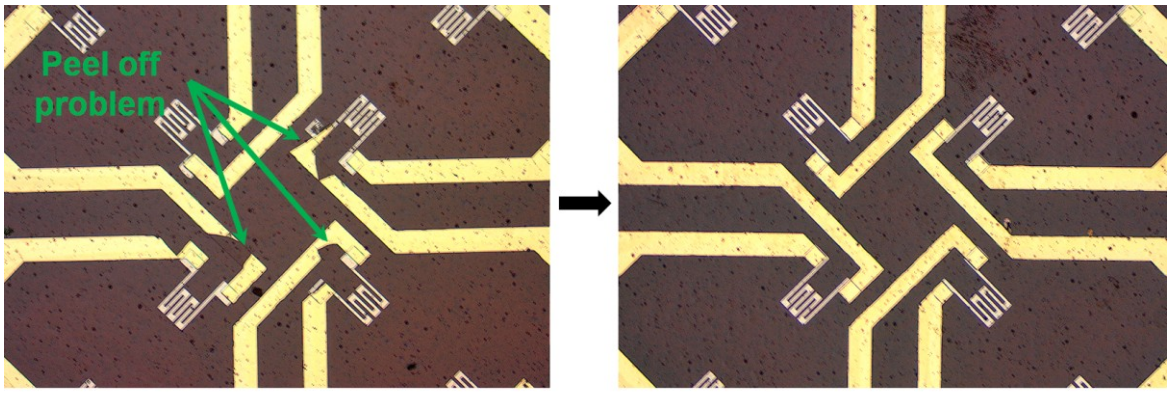

Figure 5.2.8 Effects of O_2 plasma treatment on the adhesion strength of metal layer and polyimide film [69-70].

Ni/Cr resistors deposition

(1) Cr sputtering : 100 Å / sputter
    - 61 Å/min × 1min 40sec
(2) Ni-Cr sputtering : 400 Å / sputter
    - 70 Å/min × 5min 40sec

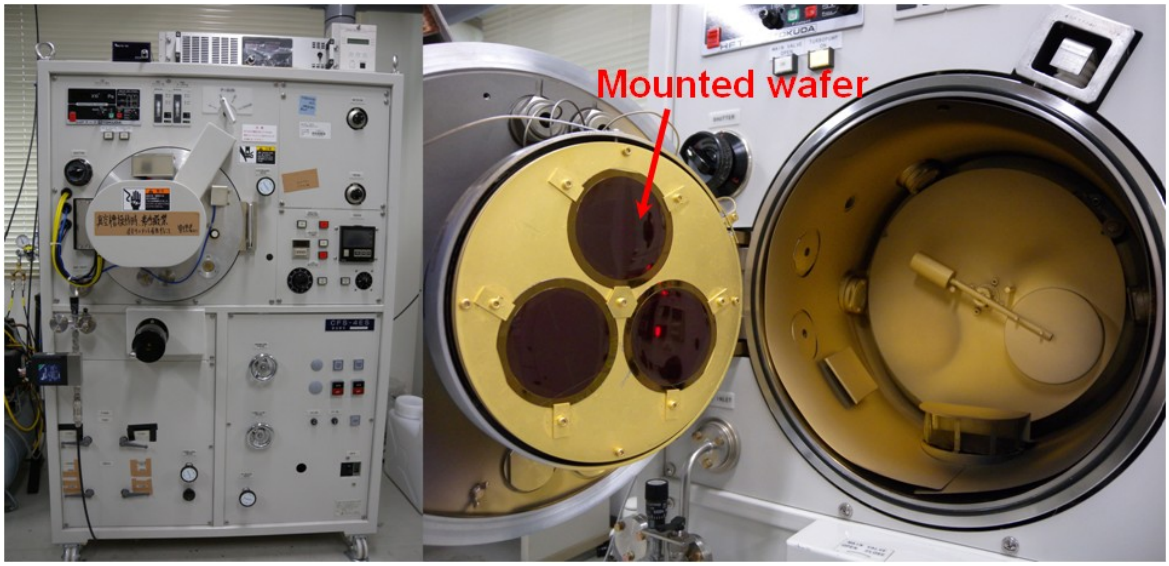

Figure 5.2.9 Sputter and wafer holder.

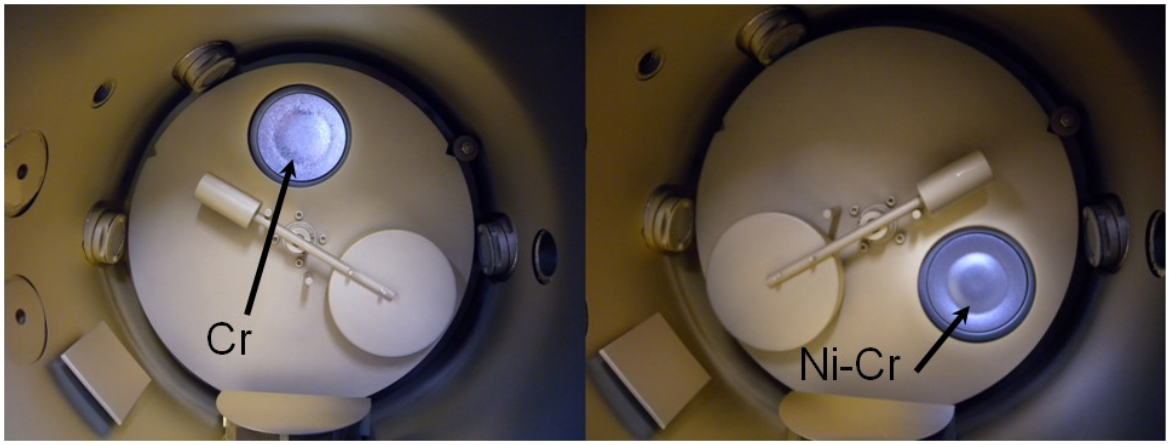

Figure 5.2.10 Cr target and Ni-Cr target inside the sputtering chamber.

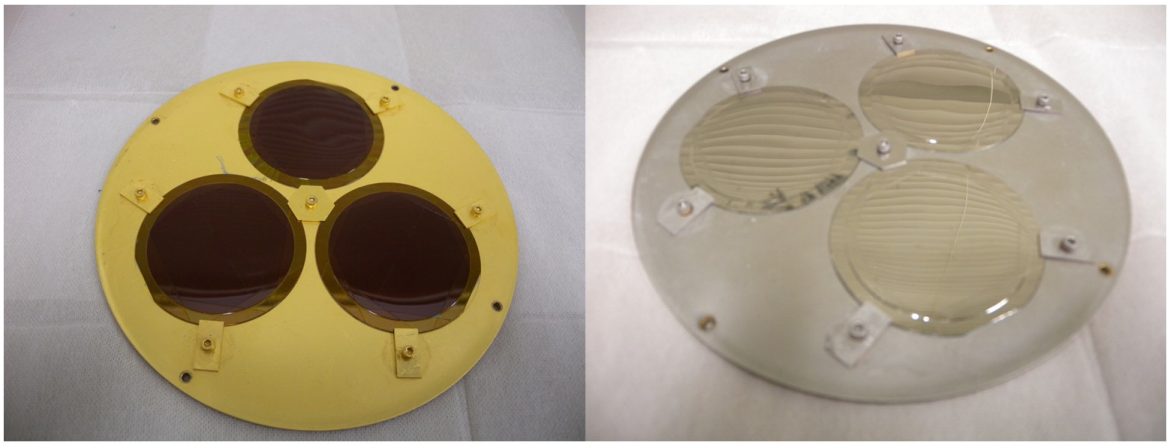

(A) (B)

Figure 5.2.11 (A) Mounted wafer and (B) Cr/Ni-Cr deposited wafer.

Lift-off of the resistors

(1) PR stripping : acetone immersion, 30 min / 4 inch teflon vessel
(2) Ultrasonic : 20 min / Ultrasonic bath
(3) D.I water rinse and dry : 1 min / 5 inch pyrex vessel

Figure 5.2.12 Ultrasonic bath and lift-off process.

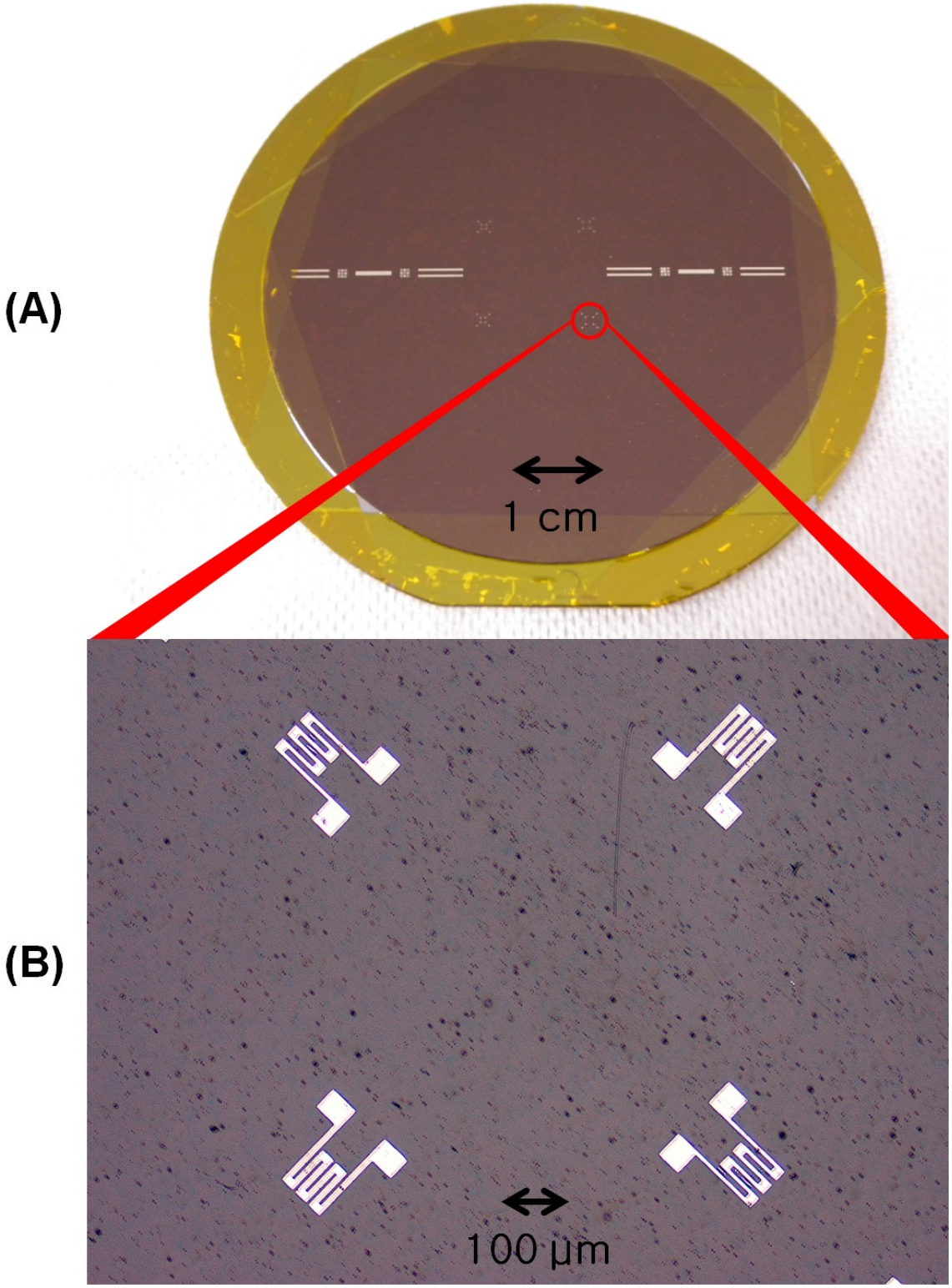

Figure 5.2.13 (A) Carrier wafer after Cr/Ni-Cr deposition and (B) magnified resistors.

5.2.3 Deposition of metal interconnects

2000-Å-thick gold interconnects were patterned on a 200-Å-thick chromium adhesion layer by sputtering, and they were patterned by lift-off process (Fig. 5.2.14).

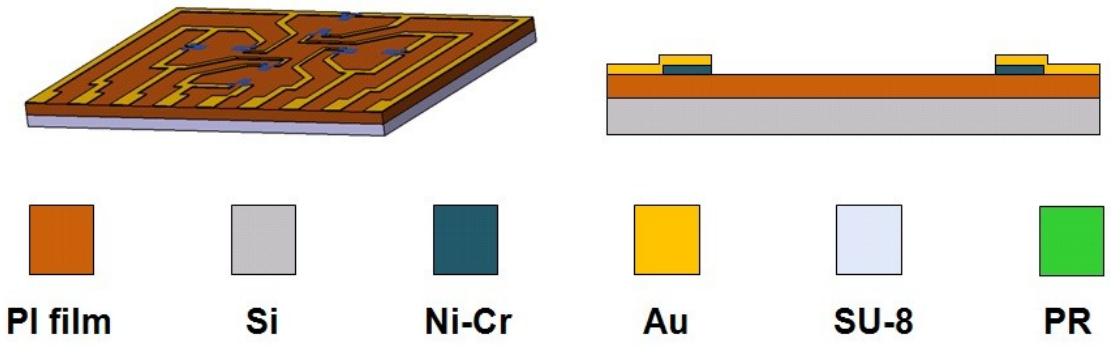

Figure 5.2.14 Metal lead lines deposition.

Photolithography of the interconnects

(1) spin coating : photo resist OFPR-800LB(100Cp) / spin coater
- step1 : 1500 rpm , 5 sec
- step2 : 3000 rpm, 20 sec

(2) soft bake : 90 °C, 30 min / hot plate
(3) align and exposure : i-line 178 mJ/cm^2 / PEM-800 mask aligner
- align mask : #2 lead line
- print gap : 0 μm
- alignment gap : 100 μm

(4) development : NMD-3 developer, 70 sec / 5 inch pyrex vessel
(5) D.I water rinse and dry : 1 min / 5 inch pyrex vessel

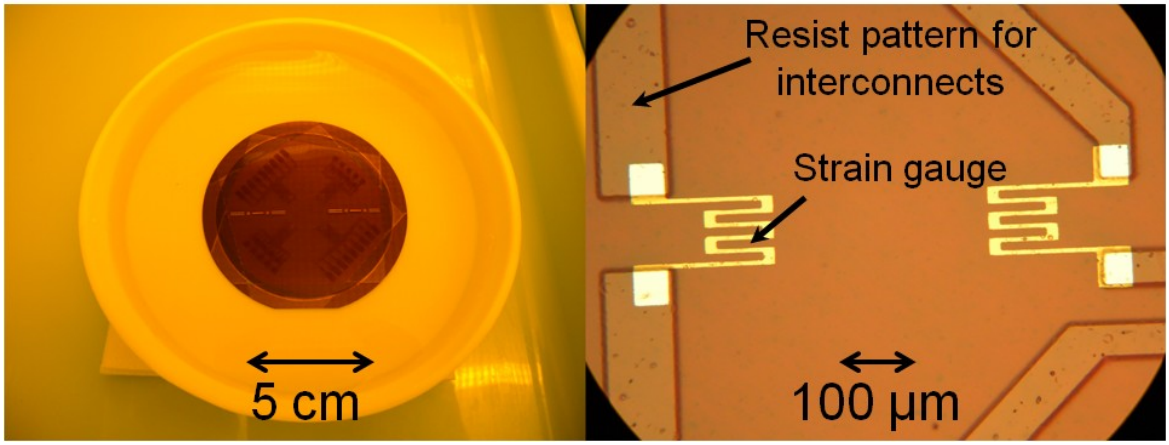

Figure 5.2.15 Development of PR and developed interconnects.

Au interconnects deposition

(1) descum : 2 min / O_2 plasma asher
- plasma power : 100 W
- chamber vacuum : 30 Pa
- O_2 : 50 cc

(2) Cr sputtering : 200 Å / sputter
- 61 Å/min × 3m 20s

(3) Au sputtering : 2000 Å / sputter
- 170 Å/min × 11m 46s

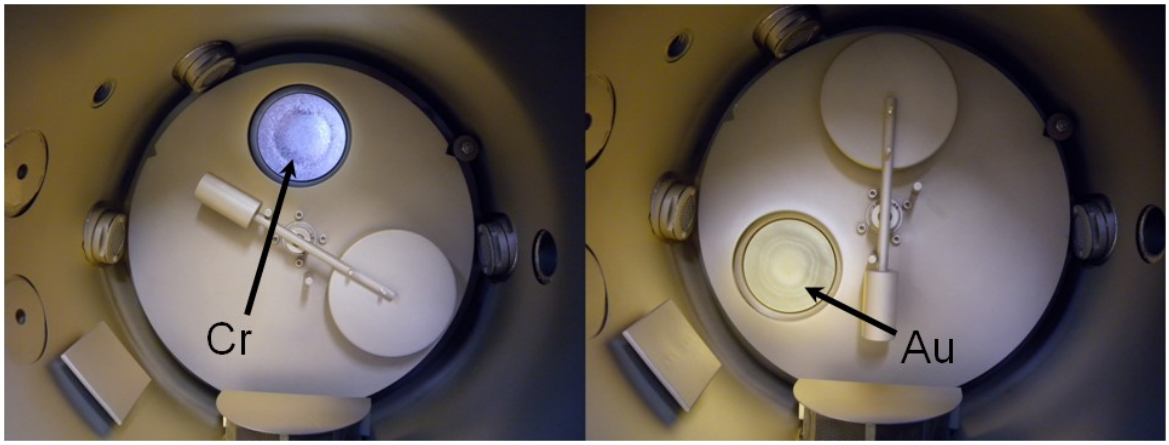

Figure 5.2.16 Cr target and Au target inside the sputtering chamber.

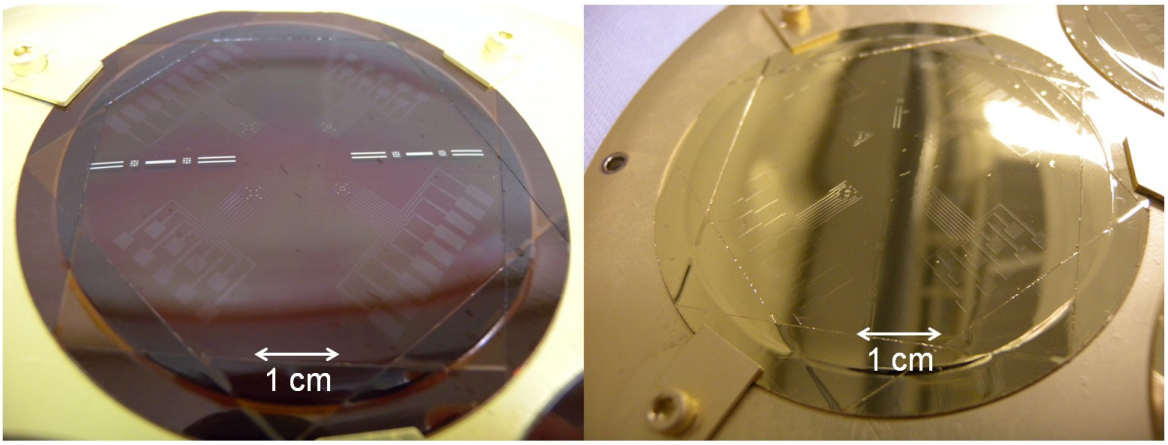

Figure 5.2.17 (A) Mounted wafer and (B) Cr/Au deposited wafer.

Lift-off of the resistors

(1) PR stripping : acetone immersion, 20 min / 4 inch teflon vessel
(2) Ultrasonic : 15 min / Ultrasonic bath
(3) D.I water rinse and dry : 1 min / 5 inch pyrex vessel

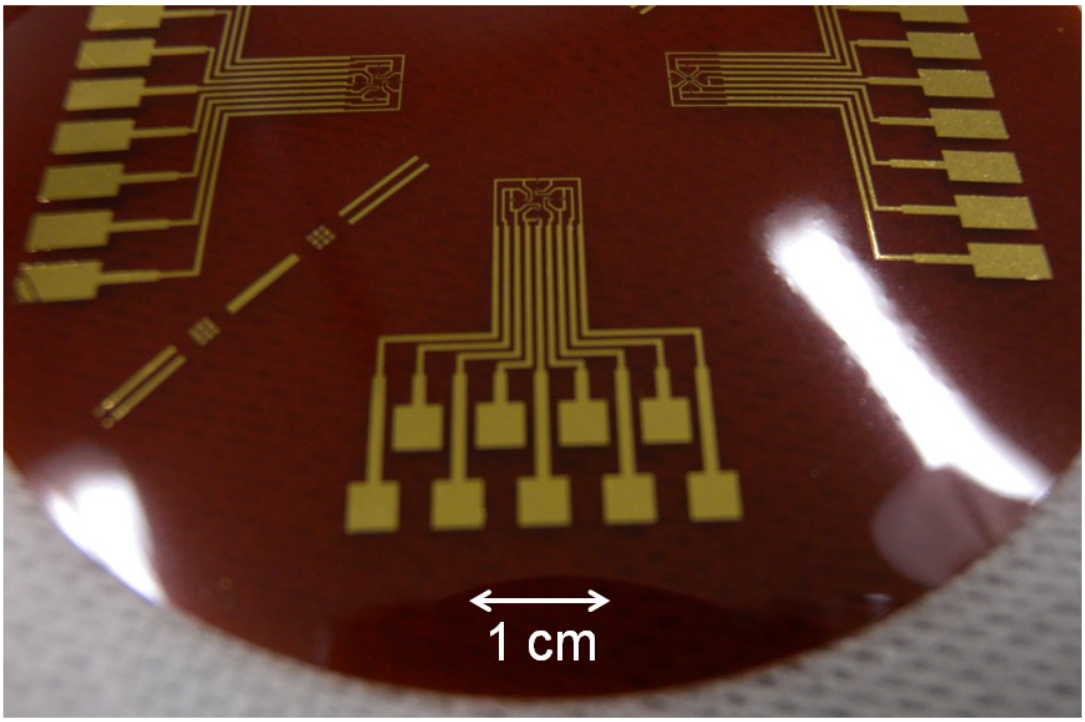

Figure 5.2.18 Optical photo of interconnects after Cr/Au deposition.

5.2.4 Formation of sacrificial layer

To make a table-shaped three-dimensional structure to use as a sensing element, a sacrificial layer was fabricated using a photodefinable lithography process with a thick photoresist material, positive-toned PMER (TOK, PMER P-HA 1300PM). Resist patterns of up to 60-μm-thick were achieved by twice coating (Fig. 5.2.19). Figure 5.2.20 shows spin coated sacrificial layer.

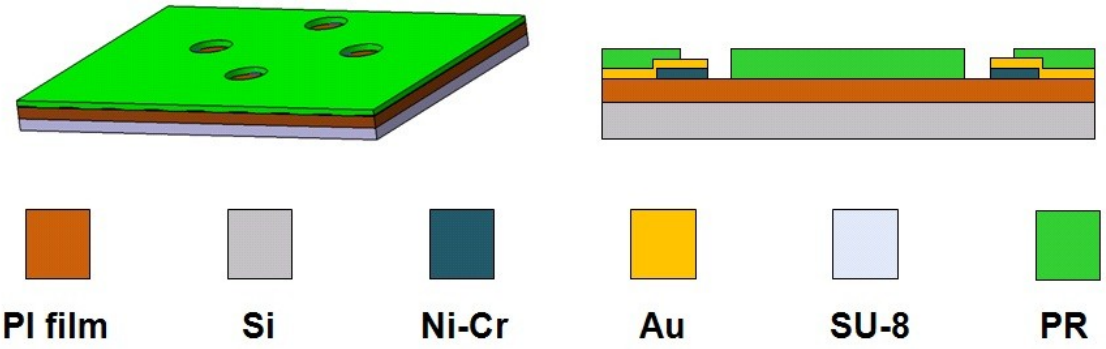

Figure 5.2.19 Sacrificial layer lithography.

- Photolithography of sacrificial layer using thick photoresist

(1) 1st spin coating : photo resist PMER P-HA 1300 PM / spin coater
- step1 : 300 rpm , 15 sec
- step2 : 800 rpm, 30 sec

(2) 1st soft bake : 110 °C, 7 min 30 sec / hot plate

(3) 1st post coating delay : 20 min / weak bake and fanning
110 °C → 30 °C; 20 °C per 5 min × 4 steps annealing

(4) 2nd spin coating : photo resist PMER P-HA 1300 PM / spin coater
- step1 : 300 rpm, 15 sec
- step2 : 800 rpm, 30 sec

(5) 2nd soft bake : 110 °C, 10 min / hot plate

(6) 2nd post coating delay : 40 min / weak bake and fanning)
110 °C → 30 °C; 20 °C per 10 min × 4 steps annealing
(7) align and exposure : i-line 3550 mJ/cm^2 / PEM-800 mask aligner
- align mask : #3 column
- print gap : 70 μm
- alignment gap : 400 μm
(8) development : PMER P-7G developer, 11 min 30 sec / 5 inch pyrex vessel
(9) D.I water rinse and dry : 1 min / 5 inch pyrex vessel

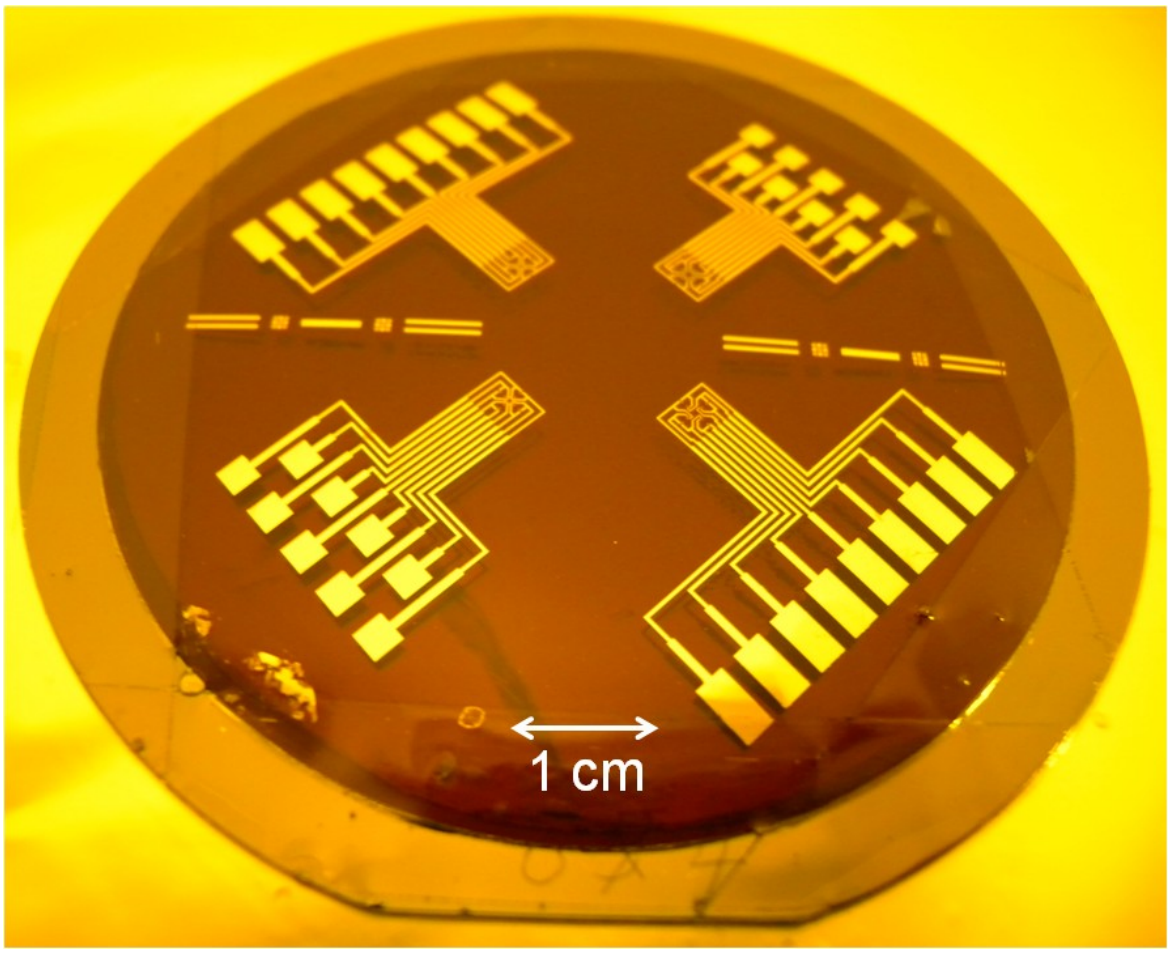

Figure 5.2.20 Spin coated thick photoresist as a sacrificial layer.

5.2.5 Patterning of table-shaped structure

As a contact plate and support column respectively, a negative-toned photo-definable epoxy (Microchem, SU-8 3050) was deposited by using a lithography process on the surface of the film and inside the sacrificial layer (Fig. 5.2.21). Figure 5.2.22 shows coating and development process.

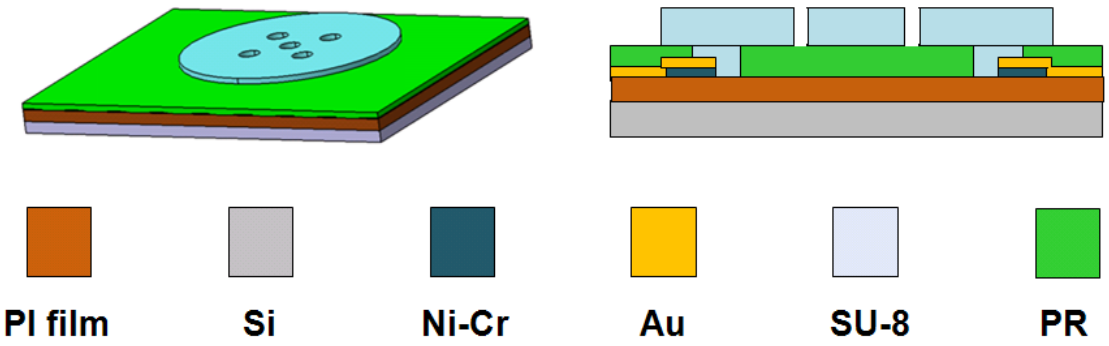

Figure 5.2.21 Pillar and sensing plate lithography.

Photolithography of table-shaped structure

(1) spin coating : photo resist SU-8 3050 / spin coater
- step1 : 500 rpm , 15 sec
- step2 : 1500 rpm, 30 sec

(2) soft bake : 95°C, 50 min / hot plate
(3) align and exposure : i-line 270 mJ/cm^2 / PEM-800 mask aligner
- align mask : #4 circular plate
- print gap : 70 μm
- alignment gap : 400 μm

(4) post exposure bake : 95°C, 5 min / hot plate (directly after expose)
(5) development : SU-8 developer, 19 min 30 sec / 5 inch pyrex vessel
(6) rinse and dry : Isopropyl Alcohol, 1 min 30 sec/ 5 inch pyrex vessel

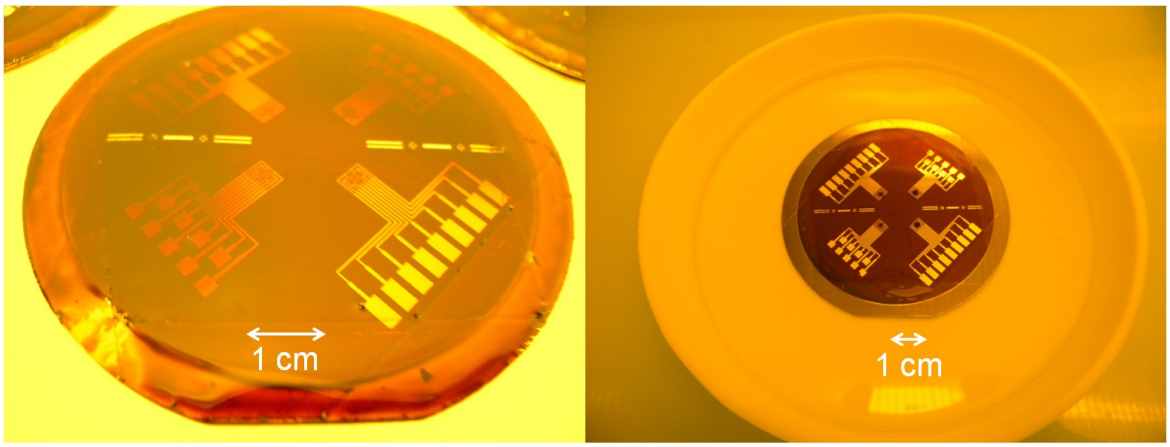

Figure 5.2.22 (A) Spin coated SU-8 epoxy and (B) development process.

5.2.6 Removal of sacrificial layer

The sacrificial layer is removed by using PMER stripper (Fig. 5.2.23). To enhance the dissolution of the sacrificial layer under the contact plate, the contact plate has five holes with 110-μm-radii which are configured symmetrically. Figures 5.2.24 and 5.2.25 show removal process and sensor-body after all micromachining process, respectively.

(1) strip and agitating : 7 min, PMER Stripper 104 / Teflon vessel
(2) heating : 70 °C, 3 min / hot plate
(3) D.I water rinse and dry : 1 min / 5 inch pyrex vessel

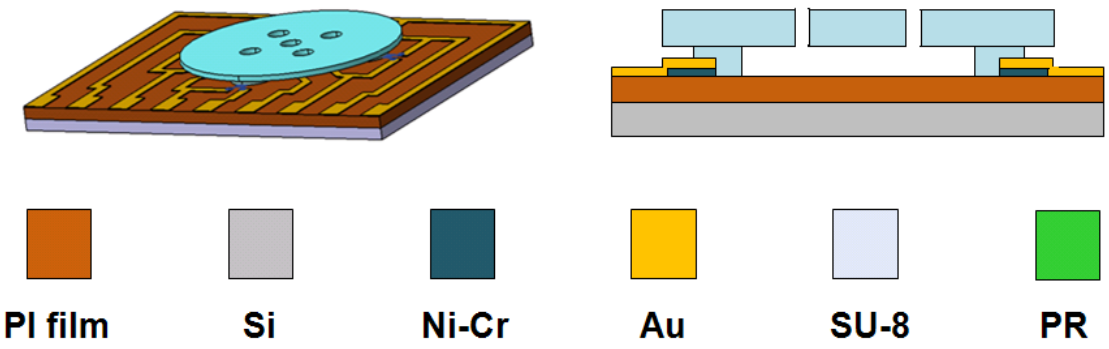

Figure 5.2.23 Removal of sacrificial layer.

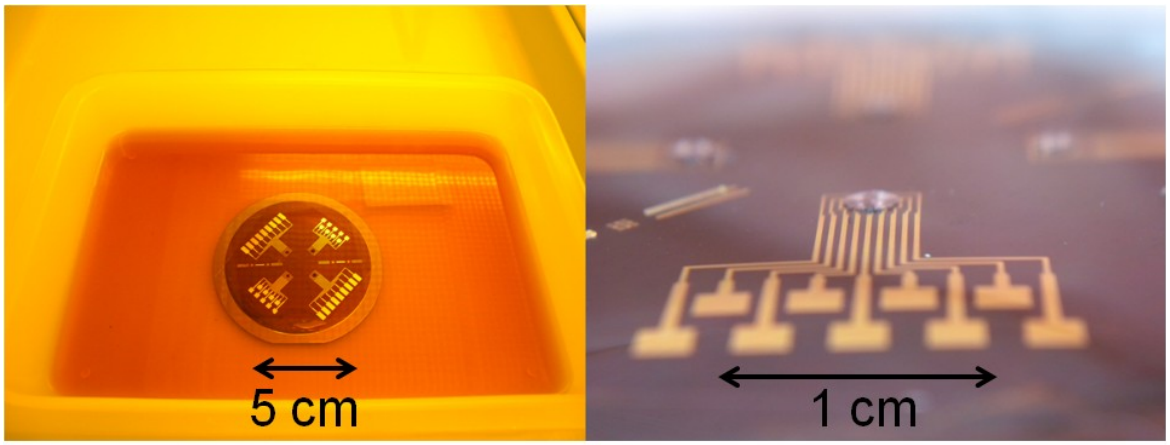

Figure 5.2.24 Removal process of thick PR and table-shaped structure.

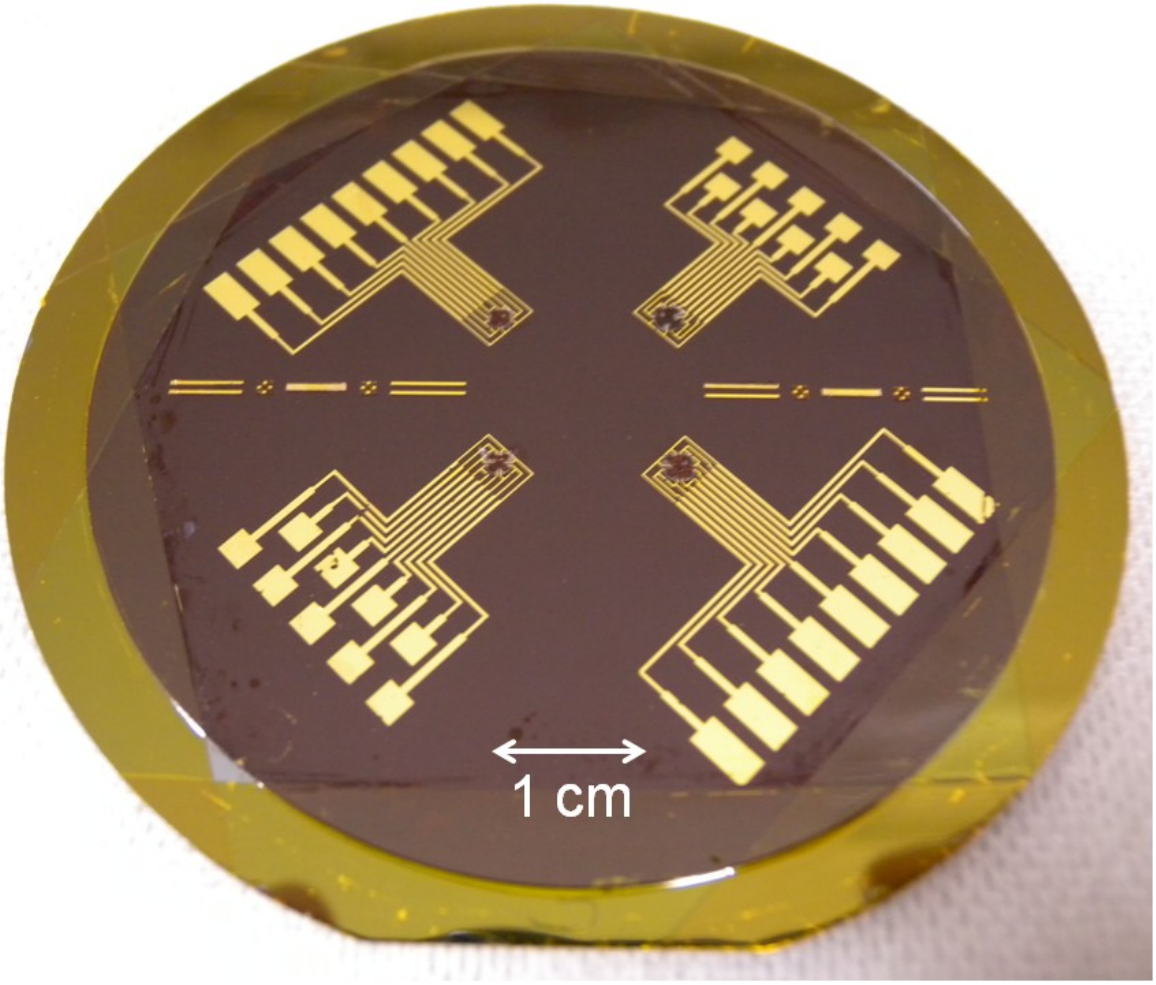

Figure 5.2.25 Sensor body after completing micromachining processes.

5.2.7 Passivation layer coating

To protect the sensor body and to form insulation layer on the circuit, the entire sensor body except the electric pads is coated in 5-μm-thick Parylene C by using parylene coating system (SCS, PDS2010). Therefore, the sensor is 250-μm-thick after the process is completed.

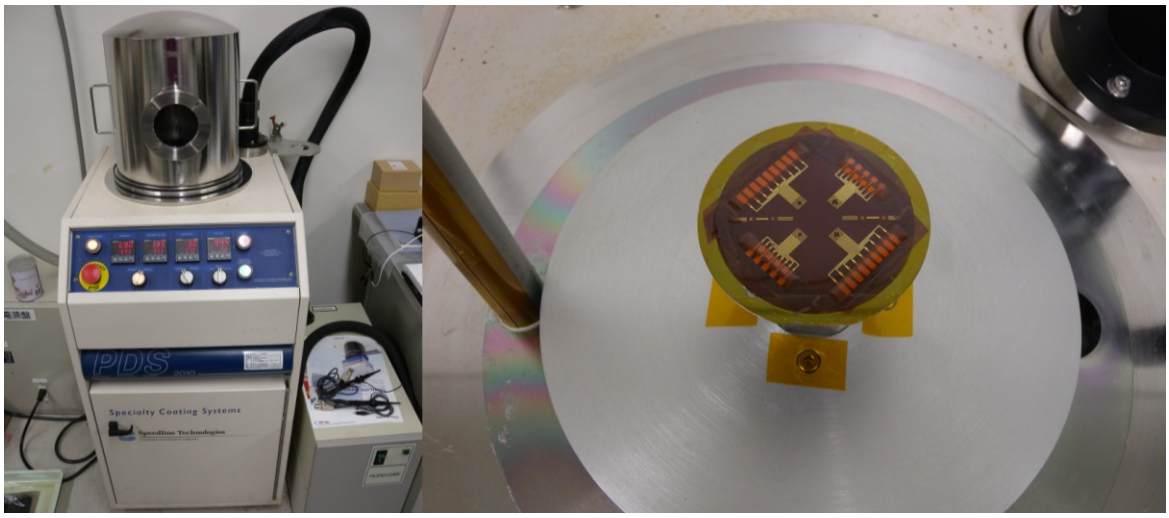

Figure 5.2.26 Parylene coating system and mounted wafer.

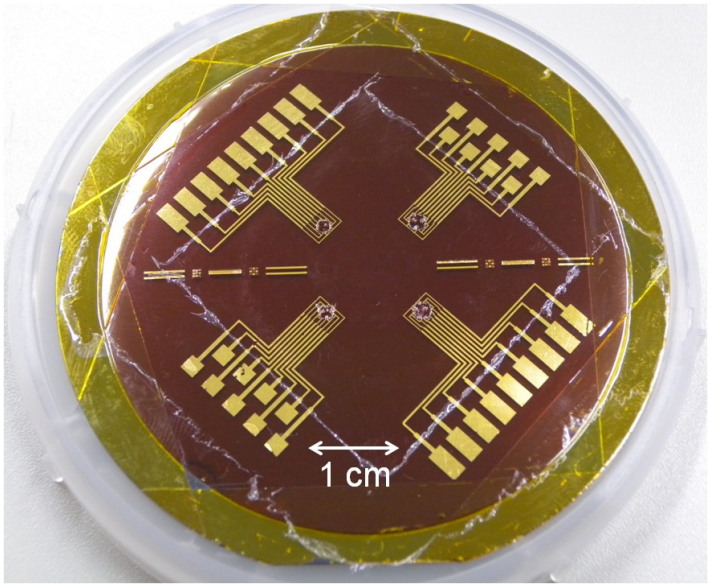

Figure 5.2.27 Sensor body after Parylene C coating.

5.2.8 Post-treatment

Release substrate from carrier wafer

The sensing device is released from the carrier wafer after the micromachining process was completed (Fig. 5.2.28). The fabricated tactile sensor (with a total thickness of 250-μm) is able to be fit on the curvature of less than 8 mm. This curvature achieves the expected flexibility of this study. Figure 5.2.29 shows the fabricated sensor body and table-shaped pad.

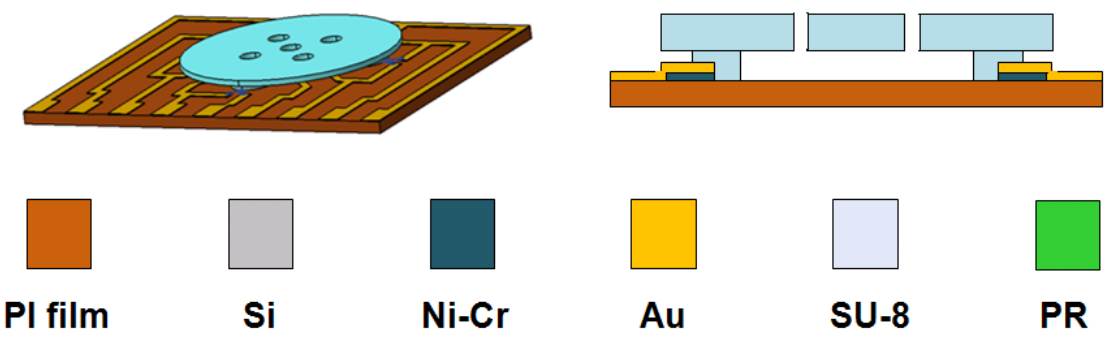

Figure 5.2.28 Release of substrate from carrier wafer.

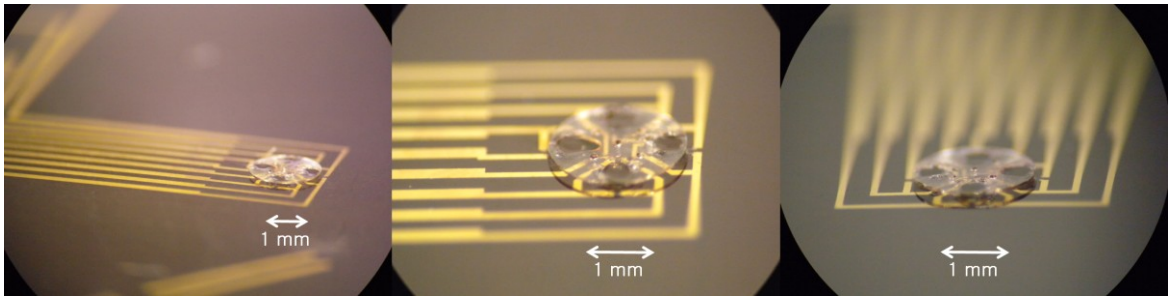

Figure 5.2.29 Released tactile sensor body and table-shaped structure.

Inspection and Wiring

Exterior examination and electric connection of the sensor is performed through microscopic inspection and checking by digital multi-meter. Finally, the electric pads are connected to a thin cord under lead soldering with Ohmic contact. Figure 5.2.30 shows inspection feature and electrically packaged sensor.

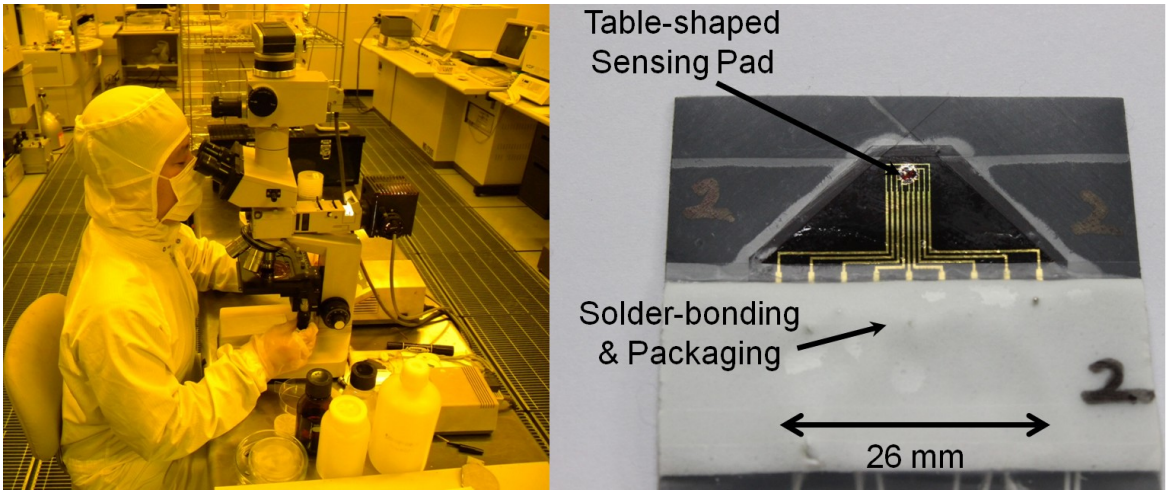

Figure 5.2.30 Microscopic inspection and packaged tactile sensor after solder-bonding.

Chapter 6

Measurement

6.1 Experimental setup

6.1.1 Data acquisition system

For the usability of the fabricated tactile sensor, a PCI-type 12-bit/16-channel data-acquisition board (Interface. Co., PCI-3174) and I/O interface (Interface. Co., TRM-7101) were connected to the sensor with a power supply (ISO-tech. Co. IPS-3610D) through a BNC cable (Interface. Co., CAB-7301), and a constant force was applied to the sensor. The voltage change of each strain gauge was converted to a resistance through the data-acquisition board, and the load was calculated from that resistance. Finally, the GPIB board sends the data to a computer via data display program (Interface. Co., GPC-3300).

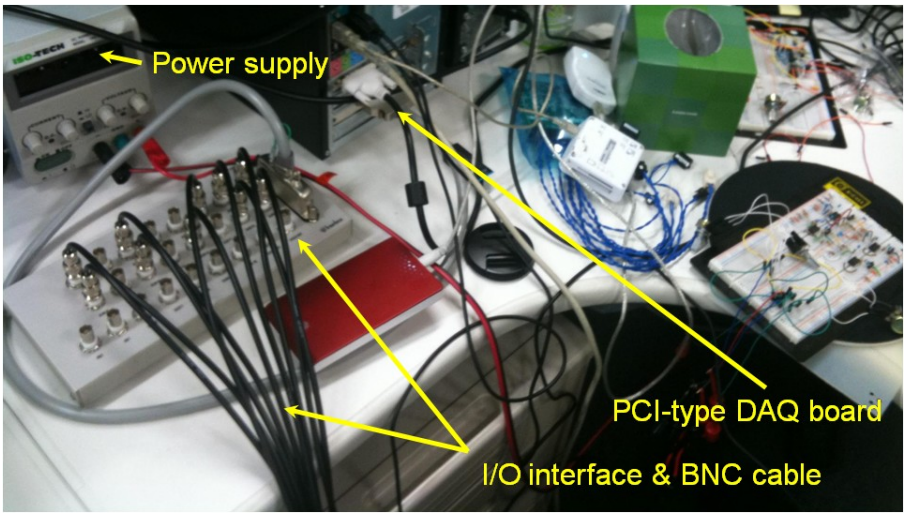

Figure 6.1.1 Data acquisition and signal processing system.

6.1.2 Force evaluation system

The fabricated tactile sensor was calibrated using an evaluation system with a three-component load cell with a probe tip. Figure 6.1.2 shows the evaluation system. The evaluation system equipped a universal stage, which has three component loadings, F_x, F_y, and F_z. These loadings are applied to the tactile sensor by rotation of the three axes of the stage. The evaluation system has the measurable force range of 10 N for the three-component force. The three-component load cell was connected to a signal conditioning amplifier (DMC 9012A, HBM Co.). Additionally, to align the sensor to the probe tip, the evaluation system has a vision system. The tactile sensor was set in the testing bed of force evaluation machine using adhesive film (3M. Co.).

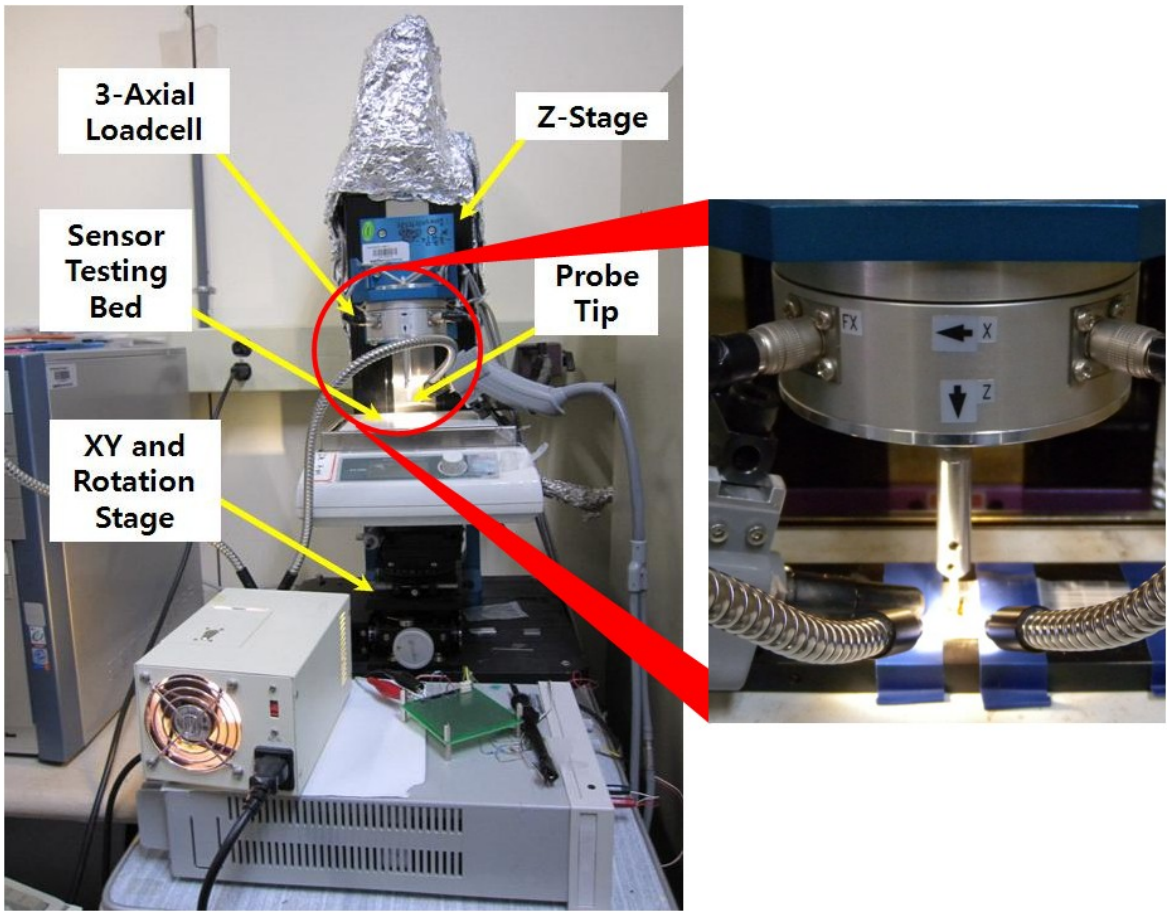

Figure 6.1.2 An evaluation system and measurement setups for tactile sensor to calibrate the resistance change at different loadings.

6.2 Force detection

While force was applied to the sensor along the *z*- and *x*-axes, the change in force on the four strain gauges, R_1, R_3, R_5 and R_7, was measured. The measured increases and decreases in resistances were found to be equal to the theoretically expected values listed in Table 3.1.1.

Normal loading F_z

The sensor was evaluated by applying normal and tangential forces between zero and 1.0 N with 0.1 N steps, respectively. The probe tip contacts the face of the contact plate of the tactile sensor as shown in Figure 6.2.1.

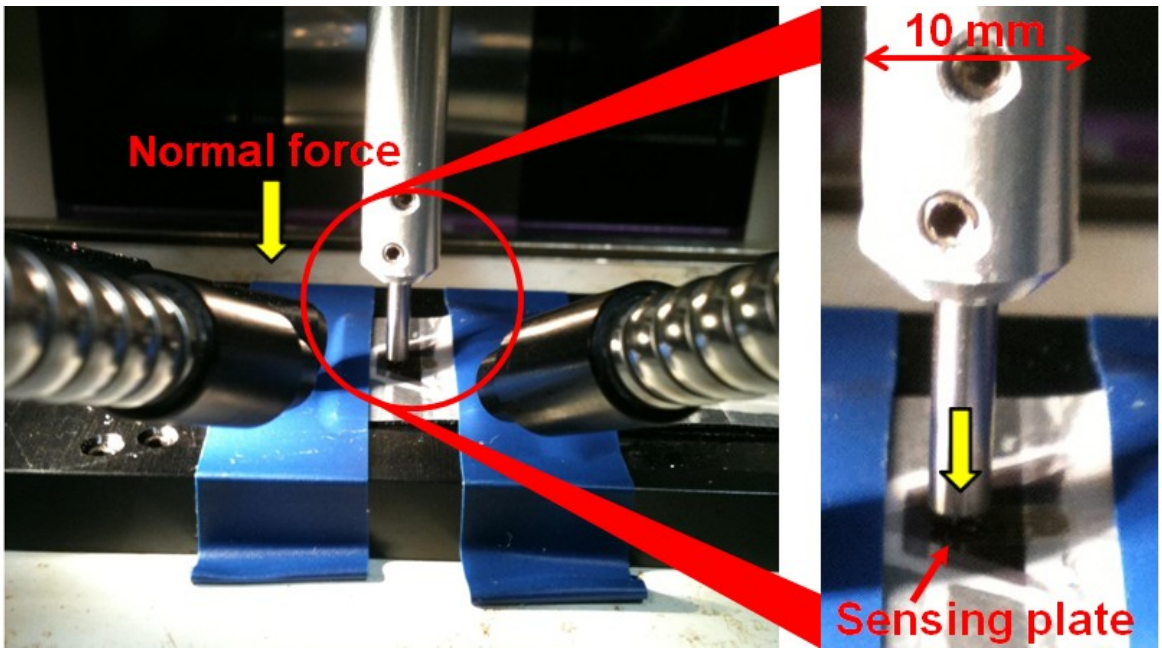

Figure 6.2.1 Applying normal force on sensing pad by probe tip.

When F_z loading (increasing from 0 to 1 N along the *z*-direction) was applied to the sensor, the output signal due to the resistance change with respect to the F_z loading and unloading (which is normalized by resistors R_1, R_3, R_5, and R_7) is shown in Figure 6.2.2. The resolution of resistance with respect to force is measured at 77,465 ppm/N in terms of $\Delta R/R$.

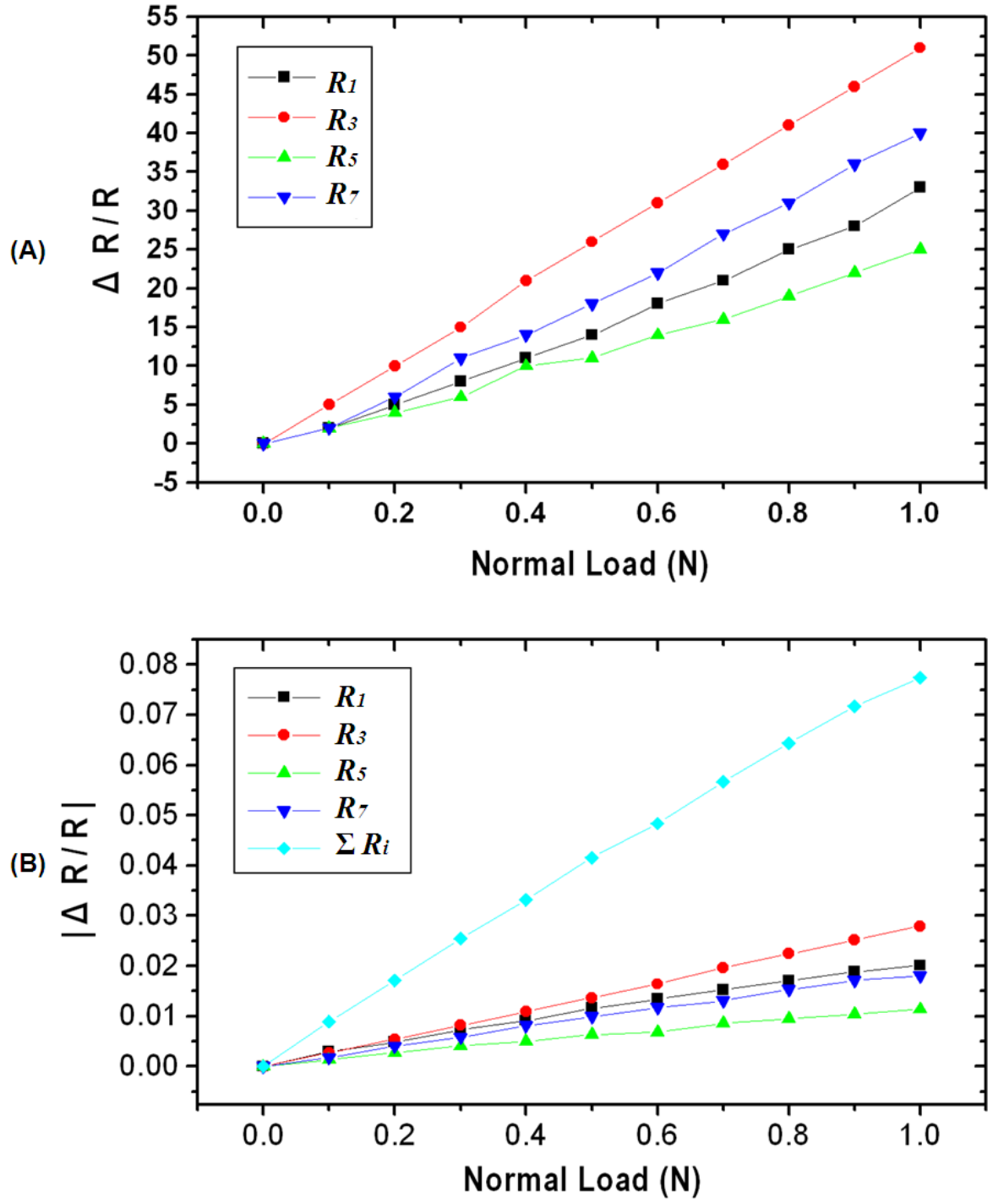

Figure 6.2.2 (A) Normalized output resistance change of the each strain gauge under normal loading F_z. (B) Calculated applied force F_z from absolute value of the normalized output resistance.

Tangential loading F_x

Originally, proposed senor is designed for surface contact force detection at upper plate. However, it is difficult to generate tangential surface contact force in the current evaluation system. Therefore, tangential load, F_x is applied to the semi-cylindrical side surface of the contact plate, alternatively as shown in Figure 6.2.3.

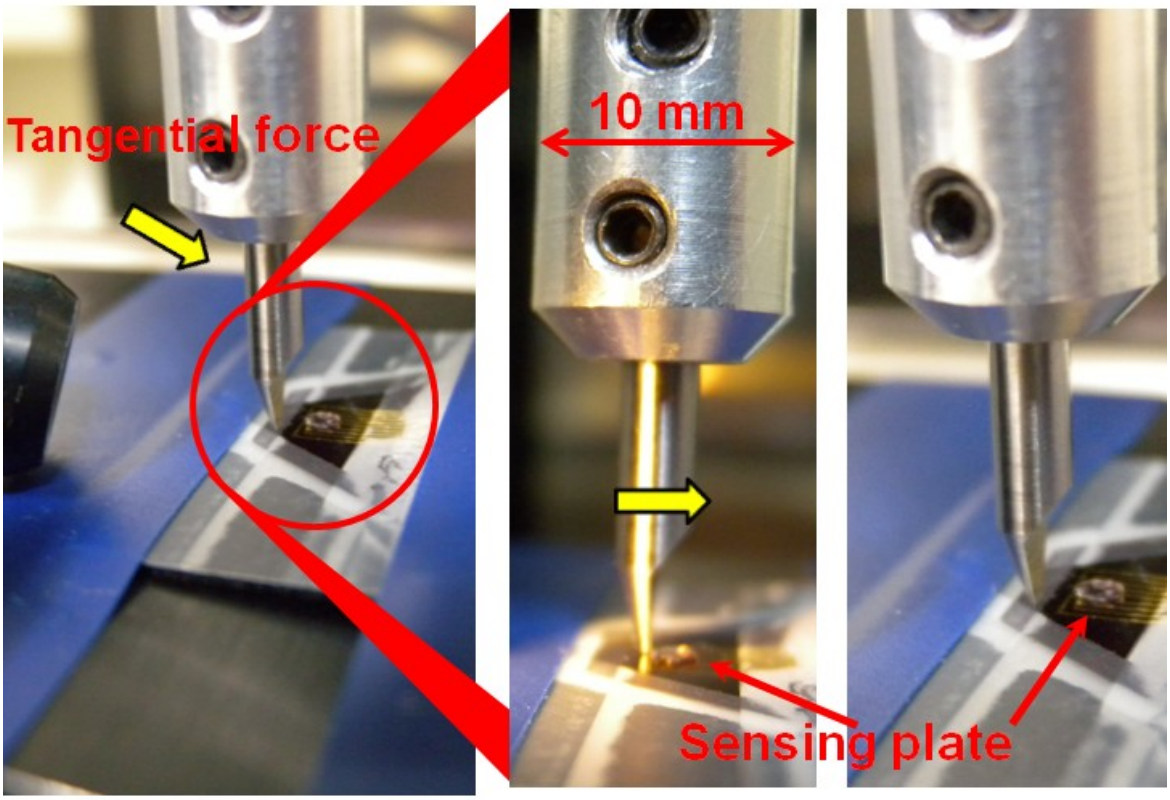

Figure 6.2.3 Applying tangential force by knife-edged probe tip.

In the case of applied F_x loading and unloading (which is normalized by resistors R_1 and R_5), the resolution of resistance with respect to force is measured at 21,693 ppm/N, as shown in Figure 6.2.4.

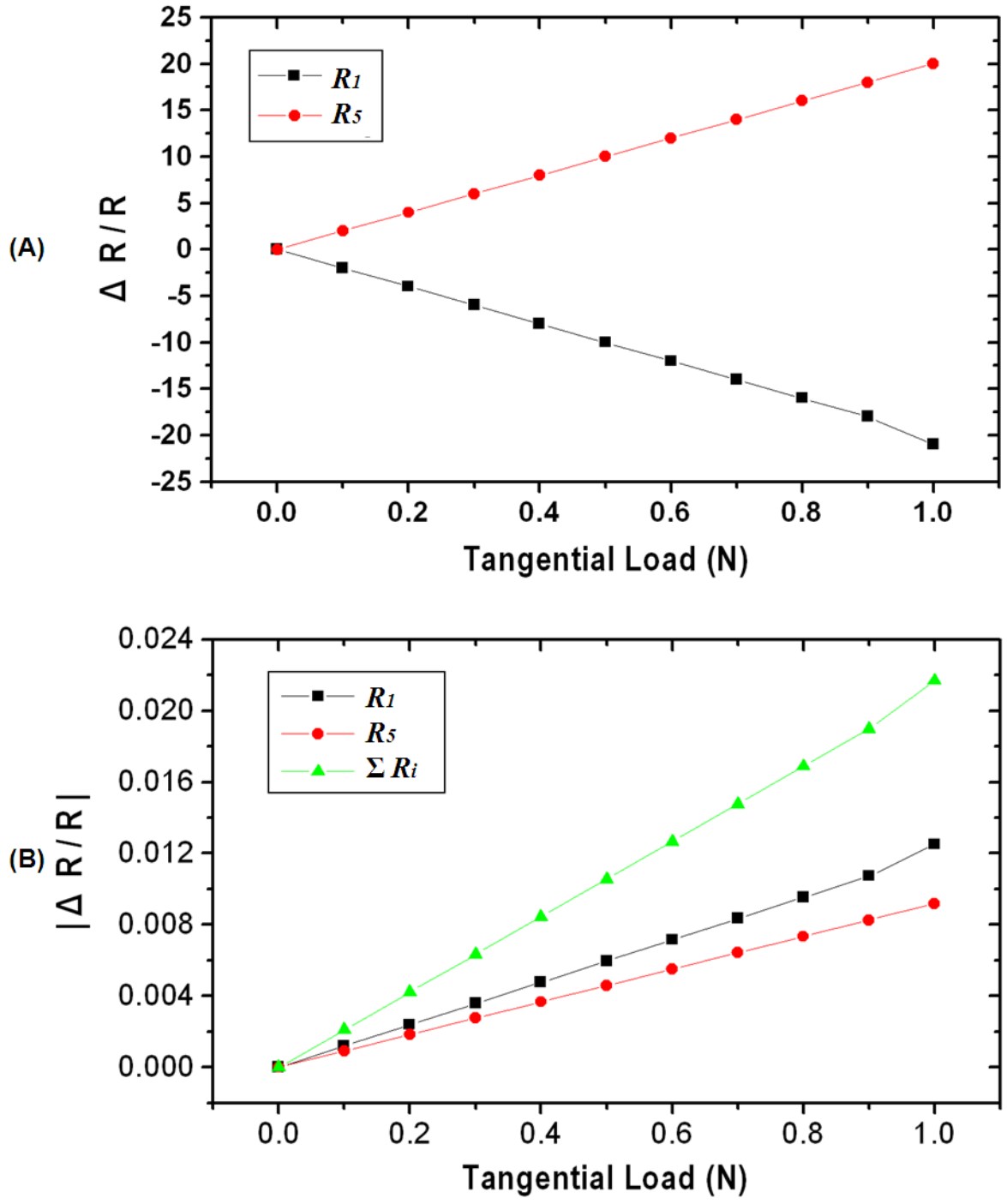

Figure 6.2.4 (A) Normalized output resistance change of the each strain gauge under normal loading F_x. (B) Calculated applied force F_x from absolute value of the normalized output resistance.

Discussion

In regard to the sensor performance, two viewpoints are considered. One is the resolution of the sensor. Fabricated sensor has the resolution of resistance change with respect to applying force measured at 7.75 %/N for the normal load and 2.17 %/N for the tangential load in terms of $\Delta R/R_0$ (see Figure 6.2.2 and 6.2.4). It shows improved resolution compared with the results of previous studies such as Kim et al. (2.1 %/N for the normal load and 0.5 %/N for the tangential load, see Table 1.2.1) [47]. The other is a sensitivity of the sensor. The sensitivity of the resistance-type sensor is expressed quantitatively as the signal amplification rate. Signal amplification rate (S) is defined as the ratio of fractional change in output resistance to the fractional change in strain as follows:

$$S = \frac{\Delta R/R_0}{\varepsilon} \tag{6.2.1}$$

Where, S: sensitivity of the sensor, R_0: offset resistance of the strain gauge, ΔR: resistance change of the strain gauge against applying external force, ε: strain of the substrate against applying external force.

In this study, the strains are changed 6.0×10^{-4}~6.1×10^{-4} by applying external normal force between zero and 1.0 N. Fractional changes in resistance ($\Delta R/R_0$) of the strain gauges are changed 0.011~0.028 by applying external normal force between zero and 1.0 N. Therefore, the sensitivities of the sensor of the fabricated sensor are determined 18.0~46.5. It means that designed table-shaped structure satisfy desired magnification of the signal amplification, in this study.

Meanwhile, the regression equation for linear fitting of F_z is expressed as below;

$$y_N = 0.07797x + 0.00147 \tag{6.2.2}$$

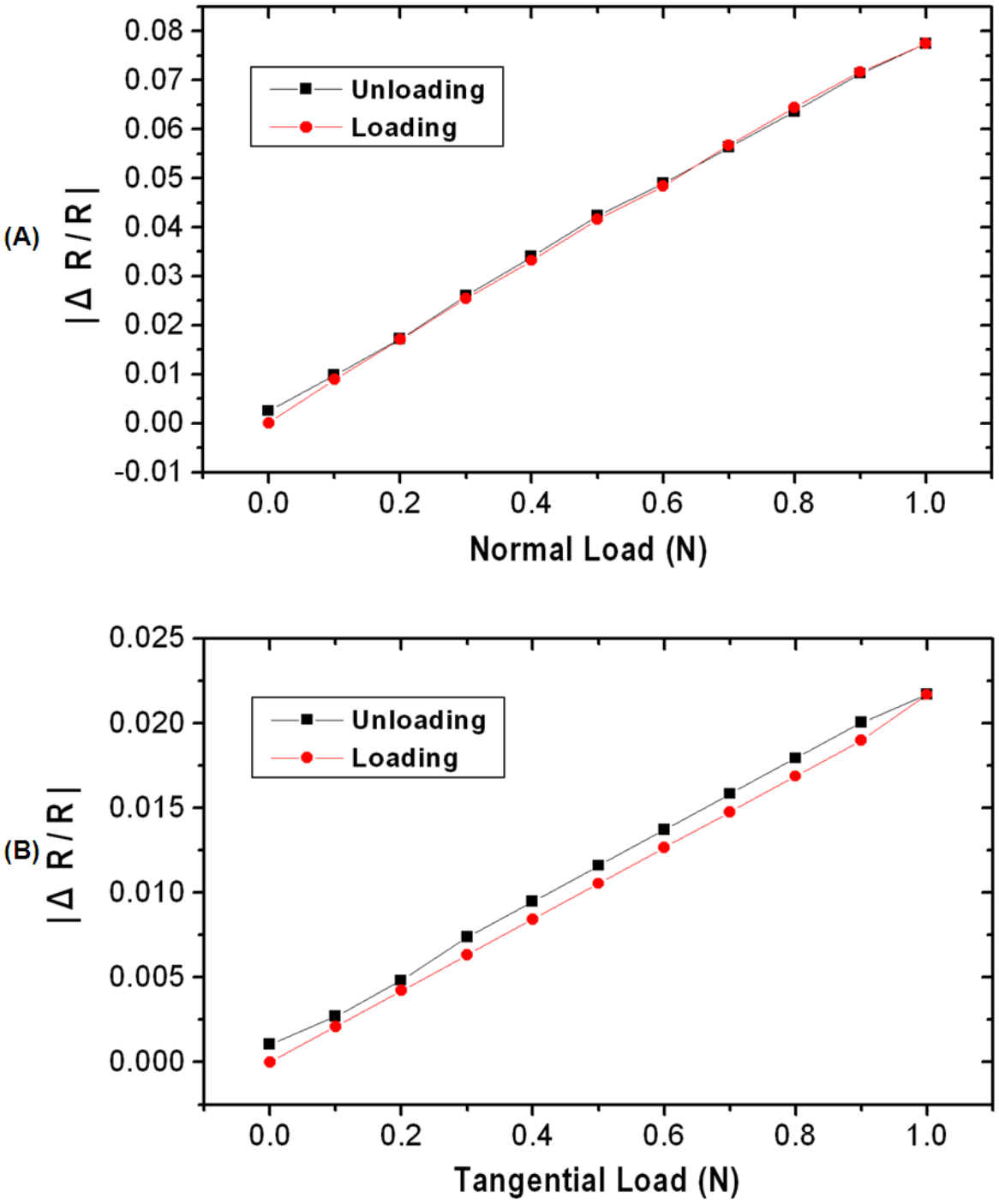

Figure 6.2.5 (A) Hysteresis change under normal loading F_z. (B) Hysteresis change under tangential loading F_x.

The regression equation for linear fitting of F_x is expressed as below;

$$y_T = 0.02137x - 0.0000813 \qquad (6.2.3)$$

From the figure 6.2.5 and equation (6.2.2) and (6.2.3), the force components F_z and F_x showed good linearity (within 0.99 % deviation) and low hysteresis (within 4.84 % deviation) under an applied loading.

Ideally, strain gauges made by the same process will have equal resistances. Although the experimental setup is perfect, fabrication errors due to the uncontrollable factors are inevitable. For example, all eight strain gauges have different initial resistances in the same fabrication process, because of their different intrinsic residual strain due to the way to deposit ionized particle. If the fabrication process is improved in the future, we believe that it will be possible to provide a simpler algorithm.

Chapter 7

Concluding remarks

7.1 Summary

In this thesis, we proposed a new type of polymer-based flexible table-shaped tactile sensor for detecting normal and tangential forces. A new fabrication approach for a three-dimensional structure was also proposed. Developed tactile senor can detect three-dimensional forces and has suitable flexibility and good sensitivity applicable for an intelligent robot's fingertips. The obtained results of this thesis are summarized as follows:

(1) To amplify the contact signal, a three-dimensionally designed table-shaped sensing element was attempted. A table-shaped epoxy sensing plate with four legs was built on top of a flexible and thin polymer substrate. This structure could effectively convert an external acting force into the concentrated internal stress with the signal amplification rate of 18.0~46.5. The normal and tangential forces could be detected by combining responses from metal strain gauges on the polymer substrate.

(2) The locations and shape/size of the strain gauges were determined by using the strain distribution obtained from FEA simulation to maximize the sensitivity of the sensor. The designed tactile sensor consists of a 60-μm-thick, 1870-μm-diameter upper plate as a sensing element and four 60-μm-high, 440-μm-diameter force-transfer columns on a 125-μm-thick, 4.18×2.91-mm rectangular membrane. The membrane material is polyimide film (with a Young's modulus of 2.5 GPa and a Poisson's ratio of 0.34). For the column and upper-plate materials, SU-8, which has a Young's modulus of 4.4 GPa and a Poisson's ratio of 0.22, is used.

(3) Triaxial force detection was calculated by combining two-dimensional mapping data on the basis of strain distribution calculated by FEA. The external loads applied to the sensor could be detected as a function of the strain-gauge responses.

(4) The fabrication process was developed based on polymer-micromachining technology. Significantly, new fabrication approaches of the sensor are proposed, such as thermo-compatible layer-by-layer process and thick sacrificial layer without wet or dry etching process for a three-dimensional structure fabrication. All processes were designed considering process-compatibility and a low process temperature of below 110°C. This technique can overcome the restrictions of the etching technique such as physical damage of the polymer material. Moreover, three-dimensional structure patterning of up to 60-μm thickness was achieved by using a photo-definable lithography process with a photoresist material, positive PMER as a thick sacrificial layer.

(5) The fabricated flexible tactile sensor was calibrated under normal and tangential forces between 0 and 1 N by using the evaluation apparatus. The sensor showed the sensitivity, 77,465 ppm/N for normal loading and 21,693 ppm/N for tangential loading in terms of $\Delta R/R$. Furthermore, normal and tangential force components showed good linearity (within 0.99 % deviation) and low hysteresis (within 4.84 % deviation) under an applied loading.

Although proposed tactile sensor remains to be conducted additional experimental study such as simultaneous loading and dynamic response for the better sensor, proposed new approaches in this study are expected to contribute in polymer-micromachining technology including three-dimensional structure fabrication using thick sacrificial layer and thermo-compatible layer-by-layer fabrication process.

7.2 Future work and Expectation

We are currently upgrading the performance of the sensor, including improvement of the signal to noise ratio and reduction of the fabrication errors in terms of the sensor sensitivity. To control the grasping force of the tactile sensor equipped robot hand is other future work. Tactile sensors in the robot manipulator field need to be tested under harsh conditions, such as impact, wear, and repeated loading, because the control for grasping in the dexterous robotic manipulation requires a robust tactile sensor.

Meanwhile, although it is no problem in a static operation, polymer materials have drawback in a dynamic situation because of its mechanical properties. For instant, since polymer materials have low elastic modulus compared to the silicon, dynamic response of the senor which is made by polymer material is later than silicon based senor. Although polyimide film and SU-8 are regarded as an elastic isotropic material, basically, polymer materials make time delay caused by restoration time from a deformation. Therefore, it is need to check dynamic response of the senor through the change of the applied loading speed. It is one of the important missions in the future work.

To verify the proposed detection method, we plan to develop an experimental setup for applying normal and tangential loadings simultaneously. Moreover, the sensing and detection algorithm will be improved to measure not only force, but also torque, by using all eight strain gauges and to solve a moment interference problem when a sensing pad meets the inclined force. Additional experiments will be conducted to check the effects of twisting or tilting moments applied to the top surface of a sensor. It is expected that the improved sensor will find many applications in the fields of not only intelligent robotic hand manipulation but also physical human-robot interaction and human-robot collaborative tasks such as dependable force feedback control.

Next, we plan to enlarge the sensing unit to a 4×4 array. This enlargement will require not only sensor fabrication but also signal processing. By making

an arrayed sensor system, we hope to provide real-time tactile information processing for a large area of a robot body. The signal processing board must be small enough to integrate the sensor system into the robot hardware system. Our ultimate goal is to integrate a sensing element and a data processing circuit like a system-on-a-chip. In addition, we will standardize the fabrication process from the viewpoint of yield improvement and commercialisation. It is expected that this approach will make it possible for the sensing device cost to be reduced in tactile-related industries.

It is expected that the polymer-based sensor could have applications in robot industry in solution for the aging society as well as in medical applications and welfare for the disabled. The sensor could be substituted for the human senses in dangerous or sensitive circumstances. In addition, a micro tactile sensor is recognized as a next generation information input-output interface for human-computer interaction. The market growth for this field will increase in the near future because tactile sensing technology will be applied to tactile displays for virtual reality environments, such as home/internet shopping. Therefore, our design and fabrication approaches would be promising as a core technology in wide fields.

References

[1] The Organization for Economic Cooperation and Development (OECD), "OECD Factbook 2010", http://www.oecd-ilibrary.org/economics/oecd-factbook-2010_factbook-2010-en, (2010).

[2] Cabinet Office, Government of Japan, "Annual report on the Aging Society 2009", http://www8.cao.go.jp/kourei/english/annualreport/2009/2009pdf_e.html, (2009).

[3] The World Health Organization (WHO), "The world health report 2007 — A safer future: Global public health security in the 21st century", http://www.who.int/whr/2007/en/ /, (2007).

[4] Ministry of Health, Labour and Welfare, Japan, "Survey on persons with physical disability and Survey of social welfare institutions", http://www.mhlw.go.jp/, (2010).

[5] Japan Organization for Employment of the Elderly and Persons with Disabilities, "Overview of persons with disabilities and their employment", http://www.jeed.or.jp/, (2010).

[6] The International Federation of Robotics (IFR), "Executive summary of world robotics 2009 service robots", http://www.ifr.org/, (2010).

[7] Ministry of Economy, Trade and Industry, Japan, "Robot market projections", http://www.meti.go.jp/, (2010).

[8] M. H. Lee, and H. R. Nicholls, "Tactile sensing for mechatronics — A state of the art survey", Mechatronics, 9, pp. 1–31, (1999).

[9] M. H. Lee, "Tactile sensing : new directions, new challenges", The International Journal of Robotics Research, 19, 7, pp. 636-643, (2000).

[10] Intuitive Surgical, Inc. http://www.intuitivesurgical.com/, (2011).

[11] T. Field, "Touch in Development. In Touch", MIT Press, Cambridge, MA, USA, pp. 37–57, (2001).

[12] I. Eibl-Eibesfeldt, "Tactile Communication. In Human Ethology", Aldine de Gruyter, Hawthorne, NY, USA, pp. 430–437, (2001).

[13] F. Yamaoka, T. Kanda, H. Ishiguro, and N. Hagita, "How contingent should a lifelike robot be? The relationship between contingency and

complexity", Connect. Sci., 19, pp. 143–162, (2007).
[14] J. Wainer, K. Dautenhahn, B. Robins, and F. Amirabdollahian, "A pilot study with a novel setup for collaborative play of the humanoid robot KASPAR with children with autism", Int. J. Soc. Rob., doi:10.1007/s12369-013-0195-x, (2013).
[15] P.S. Lum, C.G. Burgar, P.C. Shor, M. Majmundar, and M.V. Loos, "Robot-assisted movement training compared with conventional therapy techniques for the rehabilitation of upper-limb motor function after stroke", Arch. Phys. Med. Rehabil., 83, pp. 952–959, (2002).
[16] H. Yussof, M. Ohka, H. Suzuki, N. Morisawa, and J. Takata, "Tactile sensing-based control architecture in multi-fingered arm for object manipulation", Eng. Lett., 16, 9, (2008).
[17] M. Fritzsche, N. Elkmann, and E. Schulenburg, "Tactile Sensing: A Key Technology for Safe Physical Human Robot Interaction", In Proceedings of International Conference on Human-Robot Interaction, Lausanne, Switzerland, pp. 139–140, (2011).
[18] G.D. Hager, "A modular system for robust positioning using feedback from stereo vision", Trans. Rob. Autom., 13, 14, pp. 582–595, (1997).
[19] M. Prats, P. Martinet, A.P. Pobil, and S. Lee, "Vision/Force Control in Task-Oriented Grasping and Manipulation", In Proceedings of the IEEE/RSJ International Conference on Intelligent Robots and Systems, San Diego, CA, USA, pp. 1320–1325, (2007).
[20] S. Wen, B. Jia, T. Wu, S. Liu, "Unknown objects grasp planning using force/torque measurements", Adv. Int. Soft Comput., 125, pp. 741–749, (2012).
[21] J. Butterfaß, M. Fischer, M. Grebenstein, S. Haidacher, and G. Hirzinger, "Design and experiences with DLR hand II", Proceedings of World Automation Congress, 105-110, (2004).
[22] B. J. Kane, M. R. Cutkosky and G. T. A. Kovacs, "A traction stress sensor array for use in high-resolution robotic tactile imaging", Journal of Microelectromechanical Systems, 9, 4, 425-434, (2000).
[23] T. Mei, W. J. Li, Y. Ge, Y. Chen, L. Ni, and M. H. Chan, "An integrated MEMS three-dimensional tactile sensor with large force range", Sensors and Actuators A, 80, 155–162, (2000).
[24] Y. Hasegawa, M. Shikida, T. Shimizu, T. Miyaji, H. Sasaki, K. Sato, and K. Itoigawa, "A micromachined active tactile sensor for hardness

detection", Sensors and Actuators A , 114, 141–146, (2004).
[25] L. Beccai, S. Roccella, A. Arena, F. Valvo, P. Valdastri, A. Menciassi, M. C. Carrozza, and P. Dario, "Design and fabrication of a hybrid silicon three-axial force sensor for biomechanical applications", Sensors and Actuators A, 120, 370–382, (2005).
[26] S. Spinner, J. Bartholomeyczik, B. Becker, M. Doelle, O. Paul, I. Polian, R. Roth, K. Seitz, and P. Ruther, "Electromechanical reliability testing of three-axial silicon force sensors", Proceedings of the Symposium on Design, Test, Integration & Packaging of MEMS/MOEMS, (2006).
[27] T. Nakazawa, V. T. Dau, D. V. Dao, S. Sugiyama, K. Itoigawa, and H. Ueno, "Study on integration of micro force moment sensor into joystick device", Proceedings of the 25th Sensor Symposium, 55-58, (2008).
[28] M. Shimojo, A. Namiki, M. Ishikawa, R. Makino, and K. Mabuchi, "A tactile sensor sheet using pressure conductive rubber with electrical-wires stitched method", IEEE Senors Journal, 4, 5, 589-596, (2004).
[29] Y. Suzuki, Y. Hasegawa, M. Shikida, and K. Sato, "Deformation analysis of artificial hollow fibers for fabric tactile sensor", Proceedings of the 25th Sensor Symposium, 67-71, (2008).
[30] B. Choi, H. R. Choi, and S. Kang, "Development of tactile sensor for detecting contact force and slip", IEEE/RSJ International Conference on Intelligent Robots and Systems, 2638-2643, (2005).
[31] Y. J. Yang, M. Y. Cheng, W. Y. Chang, L.C. Tsao, S. A. Yang, W. P. Shih, F. Y. Chang, S. H. Chang, and K. C. Fan, "An integrated flexible temperature and tactile sensing array using PI-copper films", Sensors and Actuators A, 143, 143–153, (2008).
[32] D. Hristuy, N. Ferrier, and R. W. Brockett, "The performance of a deformable-membrane tactile sensor-basic results on geometrically-defined tasks", IEEE International Conference on Robotics and Automation, 508–513, (2000).
[33] M. Ohka, J. Takata, H. Kobayashi, H. Suzuki, N. Morisawa, and H. B. Yussof, “Object exploration and manipulation using a robotic finger equipped with an optical three-axis tactile sensor”, Robotica, 27, 5, 763-770, (2009).
[34] J. C. Lee and D. W. Lee, "Flexible and tactile sensor based on a photosensitive polymer", Microelectronic Engineering, 87, 1400–1403, (2010).

[35] Y. Zhang and N. Miki, "Sensitivity enhancement of a micro-scale biomimetic tactile sensor with epidermal ridges", Journal of Micromechanics and Microengineering, 20, 085012, (2010).
[36] H. K. Lee, S. I. Chang, and E. Yoon, "A Flexible Polymer Tactile Sensor: Fabrication and Modular Expandability for Large Area Deployment", Journal of Microelectromechanical Systems, 15, 6, 1681-1686, (2006).
[37] H. K. Lee, J. Chung, S. I. Chang, and E. Yoon, "Normal and Shear Force Measurement Using a Flexible Polymer Tactile Sensor With Embedded Multiple Capacitors", Journal of Microelectromechanical Systems, 17, 4, 934-942, (2008).
[38] M. Y. Cheng, X. H. Huang, C. W. Ma, and Y. J. Yang, "A flexible capacitive tactile sensing array with floating electrodes", Journal of Micromechanics and Microengineering, 19, 115001, (2009).
[39] P. Peng, R. Rajamani, and A. G. Erdman, "Flexible tactile sensor for tissue elasticity measurements", Journal of Microelectromechanical Systems, 18, 6, 1226-1233, (2009).
[40] J. Engel, J. Chen, and C. Liu, "Development of polyimide flexible tactile sensor skin", Journal of Micromechnics and Microengineering, 13, 359–366, (2003).
[41] J. H. Kim, J. Il. Lee, H. J. Lee, Y. K. Park, M. S. Kim, and D. I. Kang, "Design of Flexible Tactile Sensor Based on Three-Component Force and Its Fabrication", Proceedings of the IEEE International Conference on Robotics and Automation, 2589-2592, (2005).
[42] J. I. Lee, J. H. Kim, W. C. Choi, Y. K. Park, and D. I. Kang, "Design of a flexible tactile sensor based on polymer micromachining and its fabrication", Proceedings of Asia-Pacific Symposium on Mass, Force and Torque, 269-274, (2005).
[43] H.J. Kwon and W.C. Choi, "Design and fabrication of a flexible three-axial tactile sensor array based on polyimide micromachining", Journal of Microsystem Technologies 16, 12, pp. 2029-2035, (2010).
[44] H.J. Kwon, J.H. Kim, and W.C. Choi, "Development of a flexible three-axial tactile sensor array for a robotic finger", Journal of Microsystem Technologies, 17, pp. 1721-1726, (2011).
[45] K. Kim, K. R. Lee, W. H. Kim, K. B. Park, T. H. Kim, J. S. Kim, and J. J. Pak, "Polymer-based flexible tactile sensor up to 32×32 arrays integrated with interconnection terminals", Sensors and Actuators A, 156, 284–291,

(2009).
[46] F. Jiang, G. B. Lee, Y. C. Tai, and C. M. Ho, "A flexible micromachine-based shear-stress sensor array and its application to separation-point detection", Sensors and Actuators, 79, 194–203, (2000).
[47] K. Kim, K. R. Lee, D. S. Lee, N. K. Cho, W. H. Kim, K. B. Park, H. D. Park, Y. K. Kim, Y. K. Park, and J. H. Kim, "A silicon-based flexible tactile sensor for ubiquitous robot companion applications", Journal of Physics: Conference Series, 34, 399-403, (2006).
[48] C. C. Wen and W. Fang, "Tuning the sensing range and sensitivity of three axes tactile sensors using the polymer composite membrane", Sensors and Actuators A, 145–146, 14–22, (2008).
[49] K. Noda, K. Hoshino, K. Matsumoto, and I. Shimoyama, "A shear stress sensor for tactile sensing with the piezoresistive cantilever standing in elastic material", Sensors and Actuators A, 127, 295–301, (2006).
[50] H. Onishi, H. Tachibana, Y. M. Huang, M. Sohgawa, T. Kanashima, M. Okuyama, K. Yamashita, M. Noda, and H. Noma, "Stability improvement of tactile sensor of normal and shear stresses using Ni-Cr thin film gauge", Proceedings of the 25th Sensor Symposium, 63-66, (2008).
[51] E.S. Hwang, J.H. Seo, and Y.J. Kim, "A Polymer-Based Flexible Tactile Sensor for Both Normal and Shear Load Detections and Its Application for Robotics", Journal of Microelectromechanical Systems, 16, 3, pp. 556-563, (2007).
[52] H. R. Nicholls, “Advanced tactile sensing for robotics”, World Scientific, (1992).
[53] R. D. Howe, "Tactile sensing and control of robotic manipulation", Journal of Advanced Robotics, 8, 3, 245-261, (1994).
[54] V. Maheshwari and R. Saraf, "Tactile devices to sense touch on a par with a human finger", Angewandte Chemie International Edition, 47, 41, 7808-7826, (2008).
[55] J. Engel, J. Chen, Z. Fan, and C. Liu, “Polymer micromachined multimodal tactile sensors”, Sensors and Actuators A, 117, 50–61, (2005).
[56] R. A. Russell, “Robot tactile sensing”, Prentice Hall, (1990).
[57] K. Hoffmann, “An introduction to measurements using strain gages”, Hottinger Baldwin Messtechnik, pp. 39-68, (1989).
[58] The technical staff of Measurements Group, “Strain gage based transducers - Their design and construction”, Measurements Group, pp.

37-51, (1988).
[59] J. E. Mark, “Polymer data handbook”, Oxford University Press, (1999).
[60] G. Vásárhelyi, M. Ádám, É. Vázsonyi, Z. Vízváry, A. Kis, I. Bársony, and C. Dücsõ, “Characterization of an integrable single-crystalline 3-D tactile sensor”, IEEE Sensors Journal, 6, 4, 928-934, (2006).
[61] J. W. Gardner, V. K. Varadan, and O. O. Awadelkarim, “Microsensors, MEMS and smart devices”, John Wiley & Sons, (2001).
[62] S. Maruo and K. Ikuta, “Submicron stereolithography for the production of freely movable mechanisms by using single-photon polymerization”, Sensors and Actuators A, 100, 70–76, (2002).
[63] I.G. Foulds, R.W. Johnstone, and M. Parameswaran, "Polydimethylglutarimide (PMGI) as a sacrificial material for SU-8 surface-micromachining", J. Micromech. Microeng., 18, pp. 075011-22, (2008).
[64] S. Metz, S. Jiguet, A. Bertsch, and Ph. Renaud, "Polyimide and SU-8 microfluidic devices manufactured by heat-depolymerizable sacrificial material technique", Lab Chip, 4, pp. 114–120, (2004).
[65] I.G. Foulds and M. Parameswaran, "A planar self-sacrificial multilayer SU-8-based MEMS process utilizing a UV-blocking layer for the creation of freely moving parts", J. Micromech. Microeng., 16, pp. 2109–2115, (2006).
[66] X.Q. Bao, T. Dargent, and E. Cattan, "Micromachining SU-8 pivot structures using AZ photoresist as direct sacrificial layers for a large wing displacement", J. Micromech. Microeng., 20, pp. 025005-18, (2010).
[67] I. Song and P.K. Ajmera, "Use of a photoresist sacrificial layer with SU-8 electroplating mould in MEMS fabrication", J. Micromech. Microeng., 13, pp. 816–821, (2003).
[68] A. Hartley, R. Miles, N. Dimitrakopoulos, and R.D. Pollard, "SU-8 beams and membranes", 1st EMRS DTC Tech. Conf., (2004).
[69] Y. Nakamura, Y. Suzuki, and Y. Watanabe, "Effect of oxygen plasma etching on adhesion between polyimide films and metal", Thin Solid Films, 290–291, pp. 367–9, (1996).
[70] S.H. Kim, S.W. Na, N.E. Lee, Y.W. Nam, Y.H. Kim, "Effect of surface roughness on the adhesion properties of Cu/Cr films on polyimide substrate treated by inductively coupled oxygen plasma", Surface & Coatings Technology, 200, pp. 2072–2079, (2005).